

Optimisation of the preparation process for tips used in scanning tunneling microscopy

Diplomarbeit

zur Erlangung des akademischen Grades

Diplom-Physiker

vorgelegt von

Stefan Ernst

geboren am 02. Dezember 1980 in Leipzig

Max-Planck-Institut für Chemische Physik fester Stoffe, Dresden

und

Fachrichtung Physik

Fakultät Mathematik und Naturwissenschaften

Technische Universität Dresden

2006

Eingereicht am 26. Juni 2006

1. Gutachter: Prof. Dr. Frank Steglich
2. Gutachter: Prof. Dr. Lukas Eng

Abstract

The present work deals with the preparation and characterisation of tungsten tips for the use in scanning tunnelling microscopy and spectroscopy (STM and STS, respectively). Electrochemically etched tips require additional treatment to remove the dense oxide layer which evolves during etching, and to further sharpen the tips. Facilities for *in-situ* tip conditioning were implemented to two ultrahigh vacuum STM systems. The conditioning methods, including direct resistive annealing, annealing by electron bombardment, and self-sputtering with noble gas ions, were tested. Tips were characterised by scanning electron microscopy, field emission, and STM experiments. Using the so-prepared tips, high resolution STM images and tunnelling spectra were obtained at room temperature and at low temperatures (350 mK) on graphite, gold and niobium diselenide.

Zusammenfassung

Gegenstand der vorliegenden Arbeit ist die Herstellung und Charakterisierung von Wolframspitzen, welche eine wichtige Voraussetzung für Rastertunnelmikroskopie (RTM) und -spektroskopie darstellen. Die auf üblichem Wege elektrochemisch hergestellten Spitzen bedürfen weiterer Bearbeitung, um die durch das Ätzen unvermeidlich vorhandene Oxidschicht zu entfernen und die Spitzen weiter zu schärfen. Für zwei bestehende Ultrahochvakuum-RTM wurden die für die *in situ* Spitzenbehandlung notwendigen mechanischen und elektronischen Hilfsmittel aufgebaut und getestet. Dabei wurden die Spitzen mittels Rasterelektronenmikroskopie und Feldemissionsmessungen charakterisiert. Mit den durch resistives Heizen, Elektronenstoßheizen sowie Selbst-Sputtern mit Edelgasionen bearbeiteten Spitzen konnten hochaufgelöste RTM-Daten bei Raumtemperatur und bei tiefen Temperaturen auf Graphit, Gold sowie Niobdiselenid erzielt werden.



Wie schwer sind nicht die Mittel zu erwerben,
Durch die man zu den Quellen steigt!

J. W. von Goethe, Faust I

Contents

Contents	5
List of Figures	7
List of Symbols and Abbreviations	9
1 Introduction	13
2 Basics of STM	15
2.1 Quantum mechanical tunnelling	15
2.2 The working principle of an STM	18
2.3 Instrumentation	21
2.3.1 The Variable Temperature STM (VT-STM)	21
2.3.2 The Cryogenic STM	24
3 The preparation of tunnelling tips	29
3.1 The role of the tunnelling tip	29
3.2 Electrochemical etching	32
3.3 Means of tip characterisation	35
3.4 Methods for <i>in-situ</i> tip conditioning	42
3.4.1 Tip annealing	42
3.4.2 Self sputtering	46
3.4.3 The influence of an electric field on the tip	53
3.5 Facilities for <i>in-situ</i> tip conditioning	54
3.5.1 Tip conditioning at the Cryogenic STM	54
3.5.2 Tip conditioning at the VT-STM	56
3.5.3 A power supply for field emission and self-sputtering	56

4 Selected STM Results	59
4.1 Graphite	59
4.2 Au(111) surface	65
4.3 NbSe ₂	70
5 Summary	75
Appendix: A recipe for tip preparation	79
Bibliography.....	85

List of Figures

2.1	Tunnelling current vs. distance	17
2.2	Energy scheme of tip and sample for different bias voltages	18
2.3	Working scheme of an STM	19
2.4	Lock-in amplifier	20
2.6	Slip/stick mode	22
2.5	The VT-STM	23
2.7	The Cryogenic STM	25
2.8	Sketch of the ^3He cryostat	26
2.9	Vapour pressures of liquid ^3He and ^4He	27
3.1	Pt/Ir vs. W tip	30
3.2	Electrochemical etching process	32
3.3	W tip which had not been rinsed after etching	34
3.4	H_2 bubbles during etching	34
3.5	Potential at a metal surface	36
3.6	Field emission current vs. voltage for two W tips	37
3.7	Setup for field emission	37
3.8	Fowler-Nordheim plot	38
3.9	SEM image of tip A in figures 3.6 and 3.8	39
3.10	Tip radii vs. field emission threshold voltage	40
3.11	Setup for electron heating	43
3.12	Tips annealed by electron bombardment	44
3.13	Influence of the annealing power on the tip sharpness	45
3.14	Setup for Self-sputtering	46
3.15	Voltage vs. time during self-sputtering	47
3.16	Self-sputtered tips	51
3.17	STM images before and after self-sputtering	52
3.18	Another sputter voltage curve	52
3.19	A tip which was accidentally blunted during self-sputtering	52
3.20	Stage for tip conditioning in the Cryogenic STM.	55

3.21	Stage for tip conditioning in the VT-STM.	56
3.22	Block diagram of the power supply for field emission and self-sputtering (FESS)	57
4.1	Crystal structure of graphite	59
4.2	Atomically resolved STM images of HOPG	62
4.3	MOIRÉ patterns on HOPG	63
4.4	Differential conductance of HOPG	64
4.5	STM images of the Au(111) surface	67
4.6	Model of the reconstructed Au(111) surface	68
4.7	Monoatomic step and herringbone pattern on Au(111)	68
4.8	STM images of an Au film on glass substrate	69
4.9	$8 \times 8 \text{ nm}^2$ STM image of NbSe ₂ , featuring a charge density wave	70
4.10	Temperature dependence of the critical fields for a type-II SC	71
4.11	Tunnelling spectra of NbSe ₂ at $T = 385 \text{ mK}$, $\mu_0 H = 0.6 \text{ T}$	73
4.12	STS image of the vortex lattice in NbSe ₂	74
A.1	Recipient and gas supplies of the Cryogenic STM	80
A.2	Power supply for field emission and self-sputtering	81

List of Symbols and Abbreviations

Symbols

\AA	Angstrom unit; $1\text{\AA} = 0.1\text{ nm} = 10^{-10}\text{ m}$
α	polarisability
a (a_s/a_v)	lattice parametre (of a superlattice/vortex lattice)
b, c	constants
B	magnitude of the magnetic flux density
d	distance, gap width
$\delta(x)$	DIRAC delta function
D	diffusion constant
Δ	superconducting energy gap
e	charge of an electron, $e = 1.602 \times 10^{-19}\text{ C}$
$E, \varepsilon; E_F$	energy; FERMI energy
$f(E, T)$	FERMI function at energy E and temperature T $f(E, T) = 1/[1 + \exp(\frac{E-E_F}{k_B T})]$
\mathbf{F}	electric field strength, $F = \mathbf{F} $
Φ, Φ_{eff}	work function, effective work function
φ	angle
Γ	pair breaking parametre
h, \hbar	PLANCK constant, $\hbar = h/2\pi$
H	magnitude of the magnetic field strength
I	current
I_t	tunnelling current
j	magnitude of the current density
k	wave number (chapter 2) geometrical factor (chapter 3)
k_B	BOLTZMANN constant, $k_B = 1.381 \times 10^{-23}\text{ J/K}$
\mathbf{K}	force
κ	decay length
m	mass of the electron, $m = 9.109 \times 10^{-31}\text{ kg}$

$M_{\mu\nu}$	transition matrix element
μ_0	vacuum permeability, $\mu_0 = 4\pi \times 10^{-7} \text{ N A}^{-2}$
ω	frequency
p	pressure
$\tilde{\mathbf{p}}$	dipole moment, $\tilde{p} = \tilde{\mathbf{p}} $
P	power
Ψ	wave function
r	radius of apex curvature of a tip
$\mathbf{r} = (x, y, z)$	spatial coordinates
$\rho(E)$	(local) electronic density of states at energy E
t	time
T	temperature
T_c	critical temperature of a superconductor
T_P	PEIERLS temperature of the CDW transition
\mathcal{T}	(tunnelling) transmission probability
θ	angle
U, U_0, U_{eff}	potential
V	voltage
V_{th}	field emission threshold voltage; $I_{\text{th}} = I(V_{\text{th}})$
V_{gap}	gap voltage
W	potential energy
ξ	correction factor

Abbreviations

AES	AUGER electron spectroscopy
AFM	atomic force microscopy
CITS	current imaging tunnelling spectroscopy
EDM	electrical discharge machining
HOPG	highly oriented pyrolytic graphite
HV	high voltage
LEED	low energy electron diffraction
LHe	liquid helium
LN₂	liquid nitrogen
MFM	magnetic force microscopy
OVC	outer vacuum chamber
SC	superconductor, superconducting
STM	scanning tunnelling microscope, or microscopy
STS	scanning tunnelling spectroscopy
UHV	ultrahigh vacuum
XPS	X-ray photoelectron emission spectroscopy

1 Introduction

During the past century, considerable progress has been achieved in understanding the fundamental phenomena in matter. A milestone was certainly the formulation of quantum mechanics, which has paved the way towards a description of solids on an atomic level. Advanced experimental techniques succeeded to reveal ever new information about the inner structure of matter, which in turn stimulated the evolution of technologies in an unforeseen manner. In order to push the frontiers of sciences to ever smaller scales, scientist had to cope with the requirement to carry out experiments with increasingly high resolution. A rather young but nonetheless enormously successful approach to probe local properties of surfaces with high spatial are the so-called *scanning probe methods*. A probe is proximated to a surface to be investigated such that an interaction between probe and sample can take place. Measurements of the local interaction strength at sequential locations can be assembled to form an image. This concept can be applied to various interactions, for example VAN DER WAALS interaction (*atomic force microscopy*), magnetic interaction (*magnetic force microscopy*), or interaction with light (*near-field scanning optical microscopy*). The present work deals with *scanning tunnelling microscopy*, which refers to the quantum phenomenon of tunnelling. The distance between a conductive probe tip and a sample is reduced until the electron wave functions of tip and sample surface have significant overlap, and electrons can tunnel through the vacuum barrier. As the so-detected tunnelling current is strongly distance-dependant, it can be used to map the morphology of the sample surface with a resolution which goes far beyond the actual meaning of the term "microscopy". Besides its unique spatial resolution, one strength of the STM is the possibility to perform local *electronic spectroscopy*, and thereby gain valuable information about the sample's electronic properties. Invented in the early 1980's, STM has evolved into a standard tool to investigate the properties of surfaces and interfaces, with applications in various research fields besides physics, such as material sciences, chemistry, or biology. A brief introduction to the method of STM will be given in chapter 2 of this work, including theoretical aspects as well as their technical application.

One important prerequisite for high quality STM is a good tunnelling tip. The properties of the probe are reflected in the quality of the obtained data. The reliable preparation of tunnelling tips is one of the most important, but also one of the most tricky experimental

aspects of STM. The task of this work was it to optimise the preparation process of tungsten tips for the use in ultrahigh vacuum STM. This topic is addressed in detail in chapter 3 of this thesis. The tungsten tips are produced by the commonly used electrochemical etching procedure. For the use in STM, additional *in-situ* conditioning is necessary, specifically to remove the dense oxide layer which inevitably evolves during the etching process, and which may otherwise disturb the tunnelling experiment. Tip conditioning takes the main stage within this work. Here, the following methods had been chosen: Direct resistive annealing, annealing by electron bombardment, and self-sputtering with noble gas ions. These methods seemed to be promising while being applicable in the existing STM systems with a reasonable effort. The technical requirements had to be provided or adapted, if already available. Specifically, stages for the *in-situ* conditioning were to be designed and implemented into the respective vacuum chambers. Even though the solutions presented in section 3.5 are adapted to the requirements of the STM's of our group, the principle may well be applicable to other systems, and it might even be used for other experimental techniques which demand for sharp, clean conducting tips, as in other scanning probe methods.

The respective methods of tip conditioning had to be tested and optimised. To this end, tips were characterised by means of electron microscopy and field emission experiments. Naturally, the ultimate criterion for the quality of a tunnelling tip is to perform STM experiments. Tunnelling microscopy and spectroscopy was carried out on various samples. Selected STM data is presented in chapter 4, including for instance normal imaging and superstructures on graphite, surface reconstruction on a gold single crystal surface, and tunnelling spectroscopy in the mixed state of the type-II superconductor NbSe₂.

The demand for ultrasharp and clean metal tips has been present already before the invention of STM, for instance for the use in field ion microscopy. Throughout the years, numerous methods for tip preparation and, specifically, for the conditioning of etched tungsten tips have been suggested and tried out (see chapter 3 and references therein). Also the techniques used within this work have been known for some time, so reinventing the wheel was not necessary. However, the work of other scientists can only to some extent replace the gathering of *own* experience. Since there is probably no "standard way" for straightforward tip preparation, and the methods have to be adapted to the present technical circumstances and requirements, there is no way around finding one's own way. In addition, with a method as complex as STM, it is profitable to gain as much experience as possible with the experimental setup. In case of STM, this naturally includes the handling of the tunnelling tips. In this sense, the "recipe for tip preparation" given in the Appendix of this thesis is not claimed to be the "ultimate way" to prepare tips, rather it may be seen as guideline through one possible way, including the experiences which were made during this work.

2 Basics of STM

This chapter addresses basic aspects of Scanning Tunnelling Microscopy (STM). Section 2.1 deals with quantum mechanical tunnelling in general, as far as it is necessary to understand the concepts involved in this work. A more detailed theoretical treatment can be found for instance in Ref. [1]. The working principle will be presented and discussed subsequently in section 2.2. Finally, the two STM systems available in our group are briefly described in section 2.3.

2.1 Quantum mechanical tunnelling

In quantum mechanics, a vacuum gap in between two conductive electrodes can be described by a potential barrier. Let a barrier of constant height U_0 be extended between 0 and d on the z axis and consider a particle of energy $E < U_0$ and mass m . The solutions of the one-dimensional stationary single-particle Schrödinger equation then have the form

$$\Psi(z) = \begin{cases} b_1 e^{ikz} + c_1 e^{-ikz}, & z < 0; \\ b_2 e^{\kappa z} + c_2 e^{-\kappa z}, & 0 \leq z \leq d; \\ b_3 e^{ikz} + c_3 e^{-ikz}, & z > d \end{cases}$$

where $k = \frac{2m}{\hbar^2} \sqrt{E}$ and $\kappa = \frac{2m}{\hbar^2} \sqrt{U_0 - E}$. In contrast to classical behaviour, there is a finite probability for the particle to overcome the barrier. In order to obtain the transmission probability \mathcal{T} through the potential barrier, the current density operator

$$\hat{\mathbf{j}} = \frac{i\hbar}{2m} (\Psi \nabla \Psi^* - \Psi^* \nabla \Psi)$$

has to be evaluated for the incident and the transmitted waves, j_i and j_t , respectively. This is,

$$\mathcal{T} = \frac{j_t}{j_i} = |c_3|^2 = \dots \approx \mathcal{T}_0 e^{-2\kappa d} \quad (2.1)$$

Hence, the tunnelling current through the potential barrier *decreases exponentially* with the barrier width. In a metal, an electron at FERMI energy E_F experiences a potential barrier of the height $\Phi = V_0 - E_F$. Typical values for the work functions Φ of metals are 4 – 5 eV, hence κ is in the order of 1 \AA^{-1} . That is, the tunnelling current typically decreases by

about one order of magnitude per 2 Å width of the barrier. Even though this very simple approach can certainly not explain STM in detail, it illustrates nicely its basic idea; that is, to use tunnelling current as a sensitive measure for the distance between a sharp probe and a sample in order to map the sample surface topography.

Already before the construction of the first STM in 1982[2], the phenomenon of tunnelling had been subject to both experimental and theoretical investigations. One possible approach was given by the *transfer hamiltonian theory*, as suggested by J. BARDEEN in 1961[3]. In most practical cases the tunnelling barrier is broad enough to assume weak coupling between the two electrodes. In this case, each electrode can be treated separately, with a tunnelling hamiltonian as perturbation. Then, the many-particle tunnelling current can be written to first order as

$$I = \frac{2\pi e}{\hbar} \sum_{\mu\nu} |M_{\mu\nu}|^2 [f(T, E_\mu) - f(T, E_\nu)] \delta(E_\nu + eV - E_\mu) \quad (2.2)$$

where $f(T, E)$ is the FERMI function at temperature T , and V is the voltage applied between the electrodes. The main obstacle is then to evaluate $M_{\mu\nu}$, the matrix element for the transition of an electron in the state ψ_ν in one electrode into a state ψ_μ in the other electrode. For elastic tunnelling, BARDEEN showed that

$$M_{\mu\nu} = \frac{\hbar}{2m} \int d\mathbf{S} (\psi_\mu^* \nabla \psi_\nu - \psi_\nu \nabla \psi_\mu^*). \quad (2.3)$$

The integration surface lies in between the two electrodes.

In order to further evaluate $M_{\mu\nu}$ for the case of STM, one has to take into account the particular geometry of the setup. In an ideal STM, the probing electrode would only consist of a single point. As shown by TERSOFF and HAMANN[4], equation (2.2) in this case reduces to

$$I \propto \sum_{\nu} |\psi_\nu(\mathbf{r})|^2 \delta(E_\nu - E_F) \equiv \rho_s(\mathbf{r}, E_F) \quad (2.4)$$

where $\psi_\nu(\mathbf{r})$ are wave functions in the sample electrode at the lateral position \mathbf{r} of the probe, and $\delta(x)$ is the DIRAC delta function. Thus, the ideal STM would measure a tunnelling current which is *proportional to the sample's local density of states (LDOS) at position of the tunnelling tip*. Relation (2.4) still holds for somewhat more realistic descriptions, as long as the following constraints are fulfilled:

- The tip has an uniform density of states at the FERMI energy,
- the applied bias voltage is sufficiently small ($\simeq 10mV$),
- the temperature is low, and
- the tip wave functions are asymptotically spherical (*s-wave tip*).

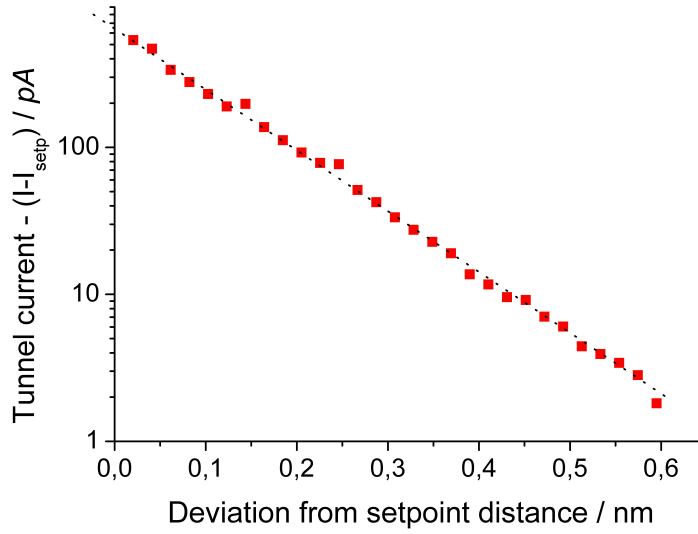


Figure 2.1: Tunnelling current vs. tip displacement (relative to the setpoint values) for a W tip on polycrystalline Au sample, semi-logarithmic plot. The dashed line is a linear fit.

The results of TERSOFF and HAMANN impart basic understanding of general features of STM data, even though the assumptions are quite severe. In practice, the low bias assumption is often violated. Also, most tunnelling tips are made from transition metals such as tungsten, where tunnelling from d -wave states cannot be neglected. One possible way out is the use of a one dimensional model for tunnelling based on the WKB approximation. This semi-classical approach to treat quantum mechanical problems is named after G. WENTZEL, H.A. KRAMERS and L. BRILLOUIN; for an introduction see for instance Ref. [5]. Assuming high momentum states and a slowly varying potential, this model predicts the tunnelling current to be[6]

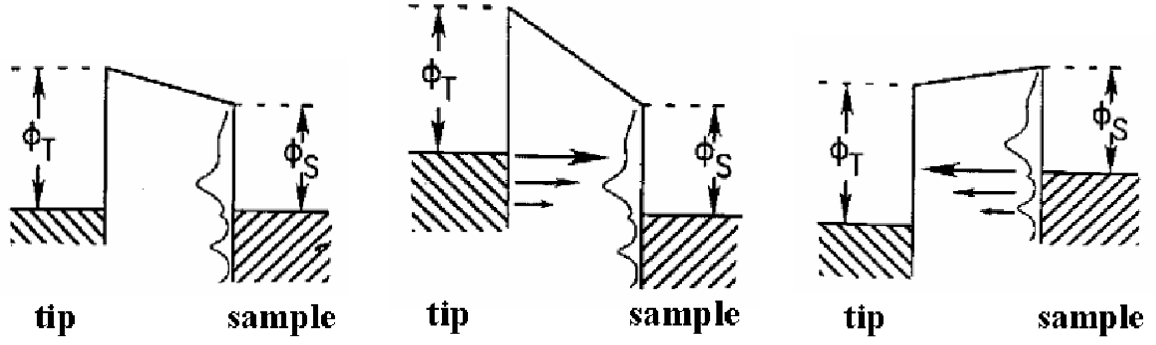
$$I(V, d, \mathbf{r}) \approx \int_{-\infty}^{\infty} d\varepsilon \rho_s(\varepsilon, \mathbf{r}) \rho_t(\varepsilon - eV, \mathbf{r}) \mathcal{T}(\varepsilon, V, d) [f(T_s, \varepsilon - eV) - f(T_t, \varepsilon)] \quad (2.5)$$

where

$$\mathcal{T}(\varepsilon, eV, d) = \exp \left\{ -2d \frac{\sqrt{2m}}{\hbar} \sqrt{\frac{\Phi_s + \Phi_t}{2} + \frac{eV}{2} - \varepsilon} \right\} \quad (2.6)$$

is the *tunnelling transmission probability* of an electron with energy ε and applied bias V . $\rho_{s/t}(\varepsilon, \mathbf{r})$ is the LDOS of sample/tip, and $T_{s/t}$ are the respective temperatures, which may differ during experiments. Note that \mathcal{T} again depends exponentially upon d , as it was also the case in equation (2.1). To illustrate this result, figure 2.1 shows the tunnelling current as a function of tip/sample distance, measured by STM. The exponential dependency of $I(d)$ is verified over almost three orders of magnitude.

According to equation (2.5), the tunnelling current is proportional to the local density of states, integrated over an energy interval. This is illustrated in figure 2.2. Without any



(a) Thermal equilibrium, zero bias (b) Positive bias, tunnelling into empty sample states (c) Negative bias, tunnelling from occupied sample states

Figure 2.2: Energy scheme of tip and sample for different bias voltages; figures from [6]

applied voltage, the FERMI levels are equal in both electrodes, and the tunnelling current is zero. If the sample is on a positive bias voltage with respect to the tip (2.2(b)), electrons can only tunnel into states *above* the FERMI energy of the sample, as (for low T) there are no empty states below E_F . The tunnelling current thus depends on the number (or density) of unoccupied states in the sample. Contrarily, the tunnelling current is sensitive to the occupied electron states at negative bias (Fig. 2.2(c)).

In the low-temperature limit (i.e. when $f(\varepsilon)$ becomes a simple step function), the ε -integration in equation (2.5) reduces to a finite interval. The *differential conductance* can then be obtained by differentiating with respect to V [6]:

$$\frac{dI}{dV}(V, d, \mathbf{r}) = \rho_s(E_F + eV, \mathbf{r})\rho_t(E_F, \mathbf{r})\mathcal{T}(eV, eV, d) + \int_{E_F}^{E_F + eV} d\varepsilon \rho_s(\varepsilon, \mathbf{r})\rho_t(\varepsilon - eV, \mathbf{r})\frac{\partial}{\partial V}\mathcal{T}(\varepsilon, eV, d) \quad (2.7)$$

For low bias voltages, the transmission probability \mathcal{T} is usually a smooth and slowly varying function, which only contributes a smooth background, and $\partial\mathcal{T}/\partial V$ can be neglected. Thus, equation (2.7) simplifies further to[1]

$$\frac{dI}{dV} \propto \rho_s(E_F + eV, \mathbf{r}) \quad (2.8)$$

Accordingly, one can assign features in dI/dV directly to the density of states as a function of energy at the lateral sample position \mathbf{r} .

2.2 The working principle of an STM

Scanning Tunnelling Microscopy belongs to the class of local probe methods. As described in the previous section, an atomically sharp conducting tip is brought into close proximity

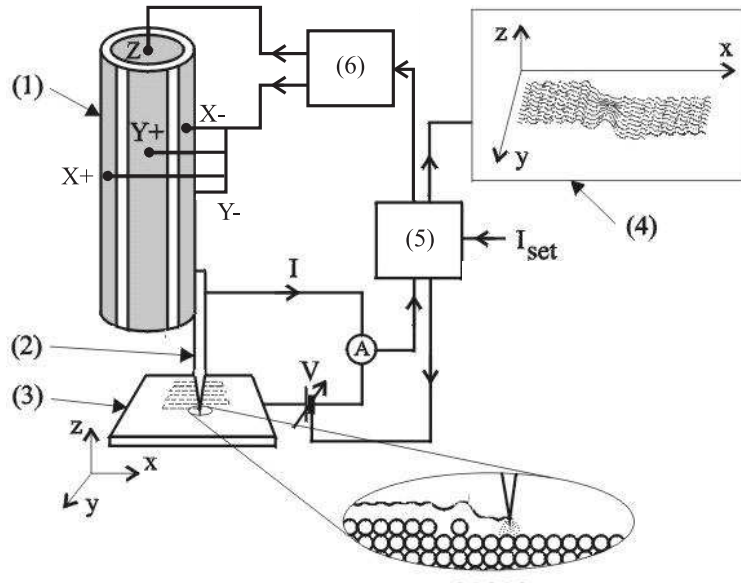


Figure 2.3: Working scheme of an STM. (1)-piezo scanner tube, (2)-tunnelling tip, (3)-sample, (4)-image: planes of constant sample DOS, (5)-control unit, (6)-piezo power supply

to the sample surface. If a voltage V is applied, a tunnelling current $I(d, V)$ according to equation 2.5 can be detected. Scanning the tip with piezo actuators across the sample surface, the exponential dependency of I upon d can be used to map the sample's surface topology. There are two principle operation modes: constant height mode, and constant current mode. In the latter case, a feedback loop regulates the z coordinate of the tip such that the measured tunnelling current maintains a pre-set value I_{set} during scanning. Surface height inhomogeneities Δz can so be detected by monitoring the extension of the piezo in z direction (or, more precisely, the voltage applied to the piezo) at each point on a (x, y) grid. According to equation 2.5, such constant current topographs can be interpreted as *planes of constant electronic density of states* above the sample. One can relate such image to the "real" surface topography insofar as the spatial distribution of the electron concentration is related to the crystal structure of the surface atoms, i.e. as the electrons "follow" the topography. Atomically resolved STM images hence do not "show" atoms but enhanced electron concentration in the vicinity of atomic sites. Spatial inhomogeneities in the tunnelling probability can also be caused by a number of other effects, though. Such can be for instance electronic excitations in the solid or changes in the work function caused by the chemical composition. Hence, the interpretation of STM topographs may be rather involved, depending on the sample.

An important feature of STM is the possibility to perform local tunnelling spectroscopy. To this end, the tunnelling current is measured as a function of gap voltage at a fixed tip position \mathbf{r} . The feedback loop is opened to keep the tip at a constant distance, and

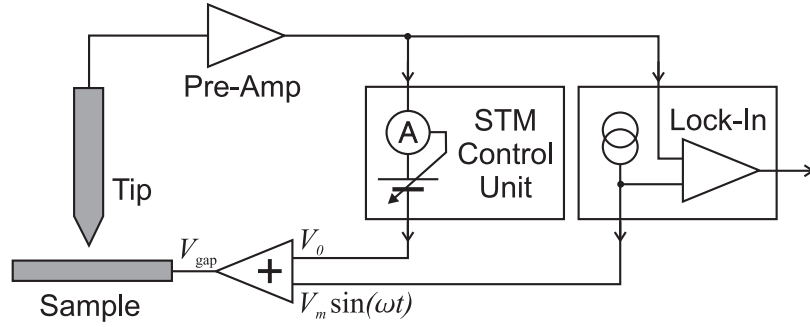


Figure 2.4: Principle for STM measurements with an lock-in amplifier

the bias is ramped stepwise in the range of interest. The averaging time within one step influences the energy resolution of the spectrum. As described above, such a spectral curve $I(V)$ contains information about the local electronic structure of the sample. According to equation (2.7), the differential conductance at bias V can be directly related to the LDOS at energy eV away from the FERMI level. In order to measure dI/dV directly, one can make use of the lock-in technique. Here, the bias voltage V_0 is modulated with a small AC voltage $V_m \sin(\omega t)$. For $V_m \ll V_0$, the tunnelling current can be expanded into a power series:

$$I(V_0 + V_m \sin \omega t) = I(V_0) + \left. \frac{dI}{dV} \right|_{V_0} \cdot V_m \sin(\omega t) + \frac{1}{4} \left. \frac{d^2 I}{dV^2} \right|_{V_0} V_m^2 (1 - \cos 2\omega t) + \dots \quad (2.9)$$

The lock-in amplifier creates a DC output signal which is proportional to dI/dV .

Compared with other experimental techniques which are sensitive to the electronic structure, such as photoemission spectroscopy, the dimensions of the STM probe are extremely small. That is, the electronic DOS is measured *locally* within a certain spatial resolution instead of integrated over a rather large sample area. A disadvantage of local probing is that one has to measure a large number of spectra to be sure that the data is representative for the whole surface. On the other hand, it provides the unique possibility of resolving spatial inhomogeneities in the electronic structure. This can be achieved by *scanning tunnelling spectroscopy (STS)*. Here, local $I - V$ curves are measured on a grid of (x, y) -points. Comparing these spectra, one can map regions of different electronic properties, e.g. due to chemical or physical phase separations. Moreover, one can study influence of external parameters such as temperature or the applied magnetic field on such phenomena, cf. section 4.3 of this work.

Temperature plays yet another important role in STM. Thermal fluctuations reduce the resolution of both topography and spectroscopy. Equation (2.5) contains the temperature dependant FERMI functions of tip and sample. Elevated temperatures lead to thermal broadening, and features in $I(V)$ are smeared out. It is therefore profitable to carry out

STM experiments at low temperatures.

Another feature of STM is its extreme surface sensitivity. Experiments are susceptible to the properties of the foremost atomic layer. This makes it an ideal tool to study surfaces. A disadvantage is that the properties of the surface are not necessarily equal to those of the bulk material. Atoms located near a surface experience an asymmetric binding environment[7]. Thus, the structure of a surface can differ substantially from the bulk (e.g. reconstructions, cf. section 4.2), and also the electronic properties may be different (e.g., bounded surface states of semiconductors situated within the gap). A further matter of concern is the chemical identity of the surface to be studied. According to kinetic gas theory, the adsorption rate of a surface is inversely proportional to the gas pressure. If kept under ambient conditions, a clean surface would be entirely covered by adsorbates within parts of a second. Moreover, chemical reactions of the sample with the surrounding gas phase, especially with oxygen, might change the surface properties drastically. In order to appropriately suppress chemical reactions and to lower the adsorption rate, it is profitable to carry out the STM experiments under vacuum conditions.

2.3 Instrumentation

2.3.1 The Variable Temperature STM (VT-STM)

The microscope described in this section is the less complex one of the two systems available in our group. It was manufactured by OMICRON NANOTECHNOLOGY GMBH[8]. The microscope is situated inside an ultra high vacuum (UHV) chamber (figure 2.5(a)) with typical pressures in the 10^{-10} mbar range. The system is equipped with one turbo molecular drag pump (Pfeiffer TMU261), two ion getter pumps (IGP) and two titanium sublimation pumps (TSP). Pressure measurement is carried out with Bayard-Alpert ionisation gauges. After having exposed the UHV system to ambient conditions, it is necessary to desorb adsorbates which have gathered at walls of the recipient. To this end, the entire system can be baked for several hours at about 150 °C.

A gate valve divides the recipient into two parts, one of which contains the STM itself. At the other chamber, a thin film preparation will be set up in future. This will allow the *in situ* preparation and investigation of materials without braking the vacuum. The transfer of samples and tunnelling tips is realised by a precision manipulator which also contains facilities for resistive sample heating up to 1170 K. This provides a possibility to prepare the sample surface for STM experiments.

The VT-STM is designed to perform measurements in a temperature range between 25 K and 1000 K. Sample cooling is realised via a liquid helium (LHe) continuous flow cryostat, which is thermally coupled to the sample by a braid and a clamping block, cf. figure 2.5(b). Specially designed sample holders shield the sample against radiation from the

environment. Elevated sample temperatures are reached by radiative heating with a PBN (pyrolytic boron nitride) heating element. Note that only the sample itself is thermalised, while the surrounding STM components remain at room temperature. This allows for a fast thermalisation and a high flexibility of conditions. However, the high temperature at the tip lowers the resolution (the Fermi function at the tip becomes very broad, cf. equation 2.5), and the large temperature gradient between tip and sample might cause undesired effects due to thermal drift.

A crucial prerequisite for achieving high resolution and low-noise STM data is isolation against external vibrations. The latter can easily interfere with data features such as atomic corrugations. For this purpose, the VT-STM is mounted on a platform which is spring-suspended inside the UHV chamber (eigenfrequency ≈ 2 Hz). Permanent magnets and copper plates are mounted to render a nearly non-periodic eddy current damping.

As mentioned in the previous section, the relative movements of tip and sample are carried out by piezo ceramics. The VT-STM uses a tube scanner, which is visible in figure 2.5(b) (cf. also the illustration in figure 2.3). The tube consists of multiple electrodes to facilitate lateral as well as longitudinal contraction. The maximum travel is limited to $12 \times 12 \mu\text{m}^2$ laterally and $1.5 \mu\text{m}$ in z direction. Additional piezo motors are implemented for coarse positioning in x and y direction and movement in z direction. These coarse piezos are operated in so-called slip/stick mode. Sliders are magnetically coupled to shear piezos. If a sawtooth voltage as in figure 2.6 is applied, the sliders are transported by the piezos during the slow piezo movement ("stick"), and slip during the fast movement due to their inert mass. The result is a relative movement of slider and piezo. In this way, relatively large translations can be carried out. Approaching tip and sample to tunnelling distance is done automatically as follows. The scanner is extracted in z direction until a tunnelling current is flowing. If at maximum extraction no current is yet detected, the scanner is retracted, and the coarse piezo steps forwards by less than the maximum extraction of the scanner. This cycle is repeated until the tip is within tunnelling distance to the sample. The tip is mounted upwards in a tip holder which itself is held magnetically on the scanner. The gap voltage is supplied to the tip whereas the sample holder is connected to ground. The measured output signals are passed through a preamplifier (OMICRON SPM Pre 4) outside the STM into the control unit (OMICRON Matrix SPM-CU).

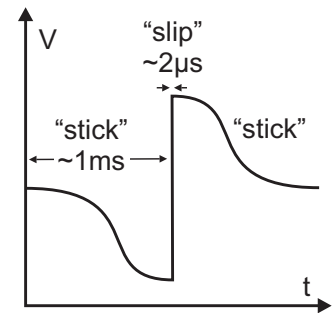
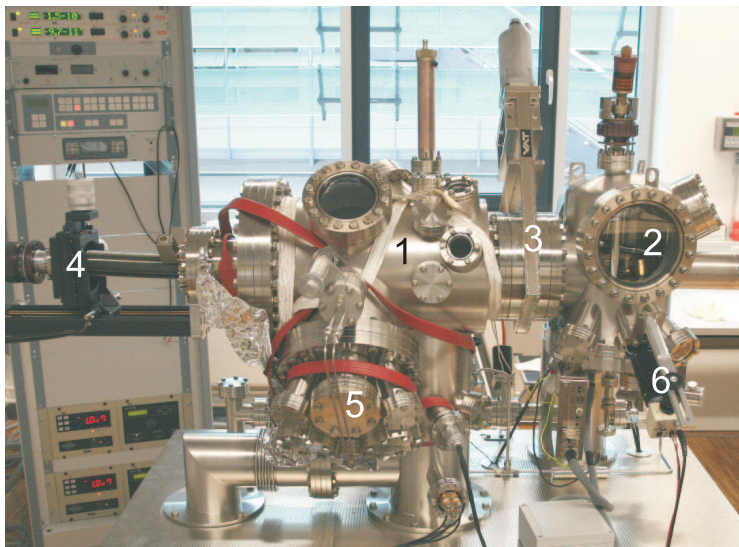
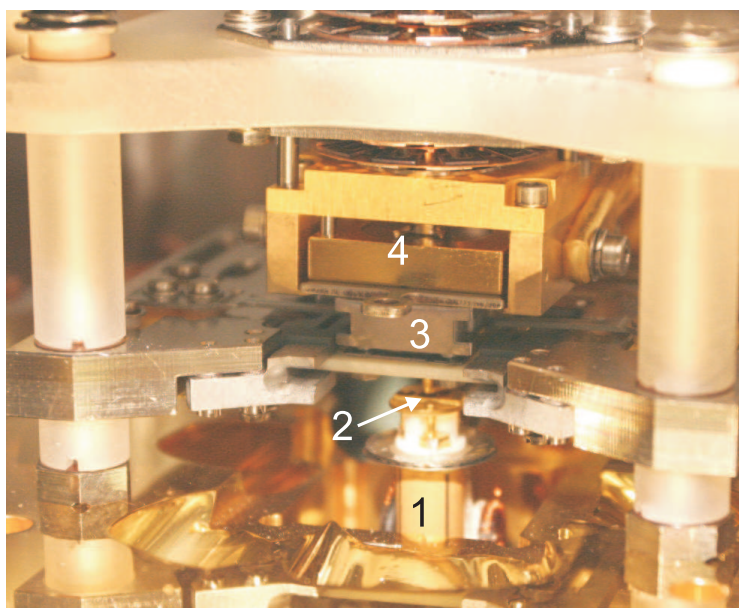


Figure 2.6: Schematic of the voltage supplied to the coarse piezo during one step



(a) The UHV recipient with MBE chamber (1) and STM chamber (2), separated by a gate valve (3); transfer manipulator (4), cluster flange (5), and CCD camera for tip positioning (6).



(b) The STM: scanner tube (1), tip holder (2) with a tip pointing upwards, sample plate (3) (cooling version), and clamping block for thermal coupling to the cryostat (4)

Figure 2.5: The VT-STM

2.3.2 The Cryogenic STM

Compared to the former, the system described in this section is technically far more complex because it combines the following requirements:

- UHV conditions
- a temperature range down to 350 mK
- a magnetic field of $\mu_0 H = 12$ T in z direction
- high stability due to sophisticated vibration isolation
- facilities for sample preparation and analysis

The system was manufactured by OMICRON NANOTECHNOLOGY GMBH as a prototype.

UHV system

The apparatus has been designed as a two chamber UHV system (figure 2.7). The preparation chamber includes facilities for the *in situ* preparation and characterisation of sample surfaces: As in the VT-STM, samples can be heated on the transfer manipulator. An argon sputter gun and a cleaving tool provide additional possibilities to prepare clean and smooth surfaces. An electron source or a X-ray source can be used in combination with an energy analyser to characterise samples by X-ray photoemission electron spectroscopy (XPS) or Auger electron spectroscopy (AES), respectively. Low energy electron diffraction (LEED) can reveal information about the atomic structure and symmetry of surfaces. The STM chamber is separated by a gate valve and extends to the innermost part of the cryostat.

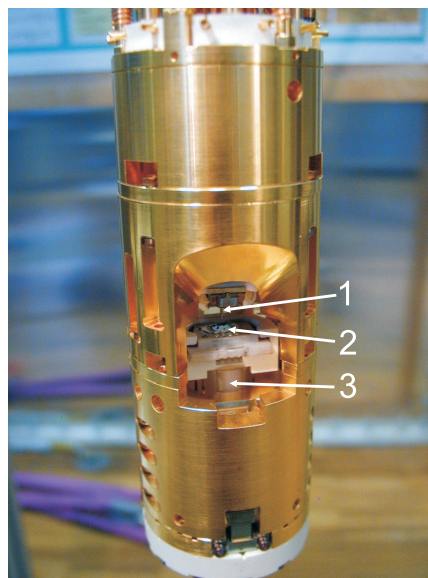
The ^3He cryostat

The system is equipped with a single shot ^3He cryostat manufactured by OXFORD LTD.[9] Figure 2.8 sketches the cryostat setup. For thermal shielding against the environment, reservoirs for liquid nitrogen (LN_2) and LHe are arranged concentrically around the cold inner part. The outer vacuum chamber (OVC) thermally decouples the respective containers. The so-called UHV sock separates the OVC from the inner UHV chamber which contains the STM. The main function of this additional double-walled vacuum specimen is it to facilitate the baking of the cryostat while the STM chamber remains evacuated. To this end, hot dry air is drawn through the UHV sock such that the inner part of the cryostat is radiatively heated. During normal operation, a flow of ^4He gas cools the innermost wall of the UHV sock.

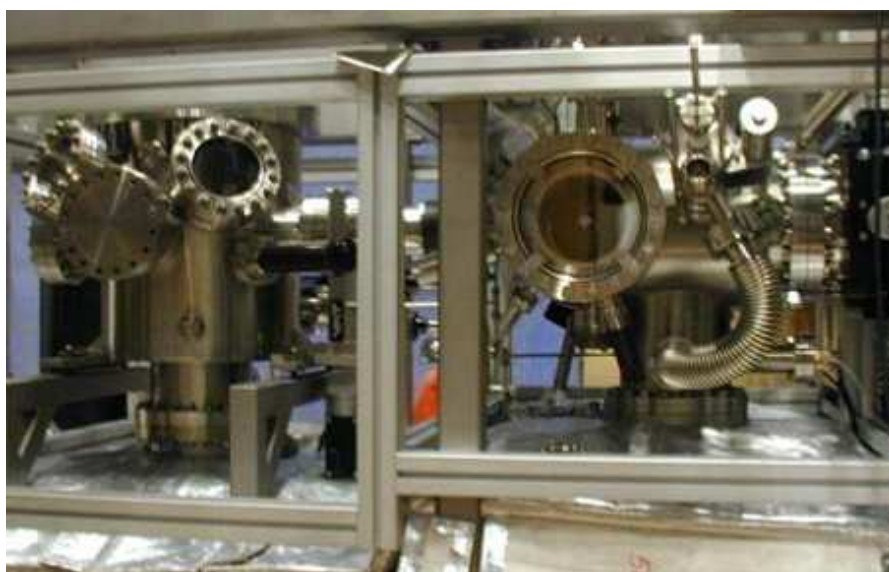
The heart of the cryostat is the UHV compatible Heliox insert. The setup is sketched in figure 2.8b). For cooling, the 1K pot is partially filled with LHe through a capillary from



(a) Overall view: the cryostat and the air legs are visible



(b) The STM head: (1)-tip, pointing downwards, (2)-sample plate, (3)-scanner tube



(c) The UHV recipient with STM chamber (left) and preparation chamber (right)

Figure 2.7: The Cryogenic STM

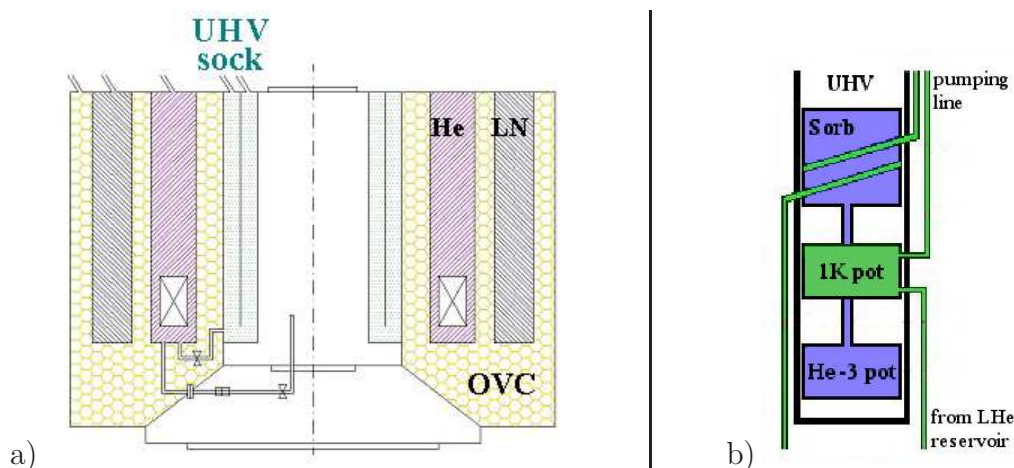


Figure 2.8: Setup sketch of the cryostat (a) with the individual specimens and cryoliquid reservoirs, and the ^3He insert (b) with the circuits for ^3He (blue) and ^4He (green)

the reservoir. By pumping the 1K pot, the He gas pressure above the liquid is reduced. The latent evaporation heat of atoms replenishing the vapour is withdrawn from the liquid's mean energy, i.e. the temperature in the LHe decreases. In this way, the pot is cooled to below 2 K. Further cooling involves a separate closed ^3He circuit. The ^3He pot is partially filled with liquid ^3He . If the pot is pumped, the vapour pressure above the liquid is reduced, and the pot is cooled down to 0.3 K. This is considerably lower than one could reach by evaporation of ^4He . The reason is that at the same temperature, ^3He has a much higher vapour pressure than ^4He due to its larger zero-point energy, cf. figure 2.9. A sorption pump (sorb) is used for pumping the ^3He pot. It contains a large charcoal surface which is kept at low temperature. ^3He atoms from the gas phase adsorb at the cold surface, and the vapour pressure drops. One cooling cycle lasts for up to 30 hours. Once all liquid in the ^3He pot has been evaporated, the ^3He has to be recondensed. To this end, the sorb is heated to about 40K such that it releases all ^3He . The gas is now free to condense in the ^3He pot which is in thermal contact with the 1K pot. According to the vapour pressure curve in figure 2.9, the condensation starts below $\sim 3.3\text{K}$. As soon as enough ^3He has condensed, the sorb heater is switched off. The sorb is now cooled and starts again to pump the ^3He pot.

The STM

The STM head is suspended with soft springs at the ^3He pot. A braid establishes a good thermal contact while minimising the mechanical coupling. It is so possible to keep the STM head with tip and sample at a temperature of about 340mK . The part of the UHV chamber which is inside the cryostat is separated from the rest of the chamber by "radiation doors". For mounting tip and sample without breaking the UHV, the entire Heliox insert

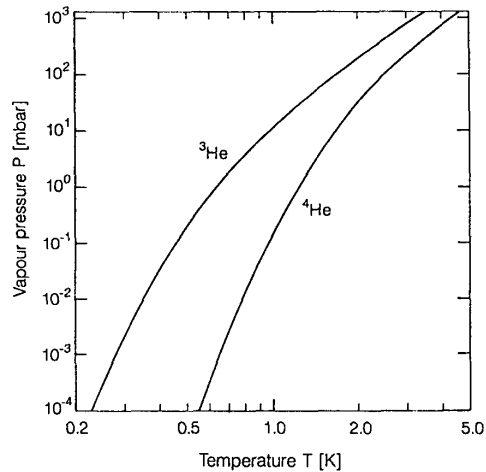


Figure 2.9: Vapour pressures of liquid ^3He and ^4He . Figure taken from [10]

can be lowered out of the cryostat into a part of the chamber where the head is accessible with a wobble stick. The STM head is surrounded by a radiation shield, consisting of two tubes. The inner tube can be rotated against the outer one to access the head through openings.

To prevent mechanical instability, the design of the STM head itself is made very compact and rigid. Therefore, no AFM/MFM option was included. Moreover, there is only one lateral degree of freedom in sample course movement. Tip positioning has to be carried out when the insert is lowered out of the cryostat. When inside the cryostat, the STM is not visible from outside, and one has to work "blindly". In contrast to the VT-STM, the gap voltage is here applied to the sample, whereas the tip is connected to ground.

A superconducting magnet is situated in the LHe reservoir of the cryostat. In its operating position, the STM head is positioned in the centre of the magnetic field. The maximum field at the sample position is $\mu_0 H = 12$ T perpendicular to the sample surface. In this way, field induced variations of the sample's electronic structure can be studied. Electronic phase separations can be directly observed by STS, e.g. vortex lattices in type-II superconductors[11].

Vibration isolation

One reason for the considerable effort in cryotechnique is that various phenomena only occur at low temperatures, such as superconductivity. Another, equally important fact is that the resolution of STM decreases at higher temperatures. This is particularly destructive for the energy resolution of STS: The broadening of the Fermi distribution smears out the spectroscopic features, cf. equation (2.5). The requirement of high resolution demands for an involved isolation against external vibrations, too. Because of the strong magnet, an eddy current damping as in the VT-STM, cf. the section 2.3.1 is not practicable here. The

vibration isolation of this STM system consists of various features:

- The basement underneath the system is decoupled from the surrounding floor of the building.
- The apparatus rests on four pneumatic legs with an active vibration damping.
- All pumping lines pass a massive concrete pit.
- The STM head is suspended on springs inside the chamber. Together with the high mass of the head, the springs have a low eigenfrequency. Thermal contact is realised with a braid instead of a solid connection.

The spring suspension of the STM head is a very effective decoupling. However, it may also become a source of trouble in connection with the limited space available inside the cryostat. The diameter of the STM head is 46 mm, whereas the bore of the inner radiation shield is two inches wide. That is, there is a spacing of only 2 mm between the head and the shielding. Because of the length of the suspension springs, even tiny lateral forces exerted on the head may be enough to make the head touching the radiation shield. This mechanical and thermal coupling may then in turn distort the measurements and the thermalisation at lowest temperatures. Such tiny forces might for instance originate in small magnetic moments. As calculations show, already tiny magnetic inhomogeneities may be sufficient in connection with a radially inhomogeneous magnetic field, such as the field induced by the magnet in our STM. As a consequence, one has to be extremely careful with the choice of materials used for the construction. As an example, contacts and screws for the use in UHV are often gold coated to prevent oxidation. The deposition of gold onto a metal surface requires an underlayer because gold would not easily stick to the surface. One suitable and frequently used material for this purpose is nickel. In our case the use of nickel would lead into trouble, since nickel is ferromagnetic. It would be preferable to choose chromium instead. A further issue of concern is the material of the head itself. Originally, the head was intended to be made from titanium. But because of the magnetic moment of titanium, the latter had to be replaced by a bronze with a very low magnetic susceptibility.

3 The preparation of tunnelling tips

One important prerequisite for obtaining high quality STM and, specifically, spectroscopic data is a good tunnelling tip. As for any technique, one cannot expect the results to be better than the probe allows. The reproducible preparation of tunnelling tips is therefore one of the experimental key aspects of STM. In order to define the requirements to such preparation process, section 3.1 focuses on the role of the tip in STM. The influence of the tip material, of contaminants at the tip surface, and of the tip shape on STM experiments will be discussed in this section. Therein, it will also be explained why we are mainly interested in the use of tungsten (W) tips. A standard procedure to prepare such tips is electrochemical etching. The method will be described in section 3.2, along with some remarks on how the process can be optimised to improve the success rate of as-etched tips in STM. Equally important is additional treatment of the tips after etching. A number of conditioning methods have been studied in this work. In order to judge the efficiency of such methods and to optimise them, means of tip characterisation were necessary, which will be discussed in section 3.3. The conditioning methods will be presented and compared in section 3.4. Finally, section 3.5 deals with the technical realisation of *in-situ* tip conditioning in our STM systems.

3.1 The role of the tunnelling tip

It is intuitively clear for any measurement technique that the properties of the probe may have major impact on the quality of the obtained data. It shall be discussed which role the tunnelling tip plays in scanning tunnelling microscopy and spectroscopy, and what are thus the requirements to any tip preparation in order to get optimum results.

The two attributes relevant for the performance of a tunnelling tip are its shape and its chemical composition[12]. The latter involves two issues: the material which the tip is made of, and contaminations present on the tip surface. Contaminants can lead to severe distortion of the STM experiment. Insulating layers covering the tip apex such as metal oxides (e.g. oxides of the tip material itself) act as additional tunnelling barriers which the electrons have to overcome. The resolution would be reduced because it would be more difficult to stabilise the tunnelling current, and for small gap voltages the tip could even crash and cause damage to sample and tip[13]. Even more disturbing are such contamination layers

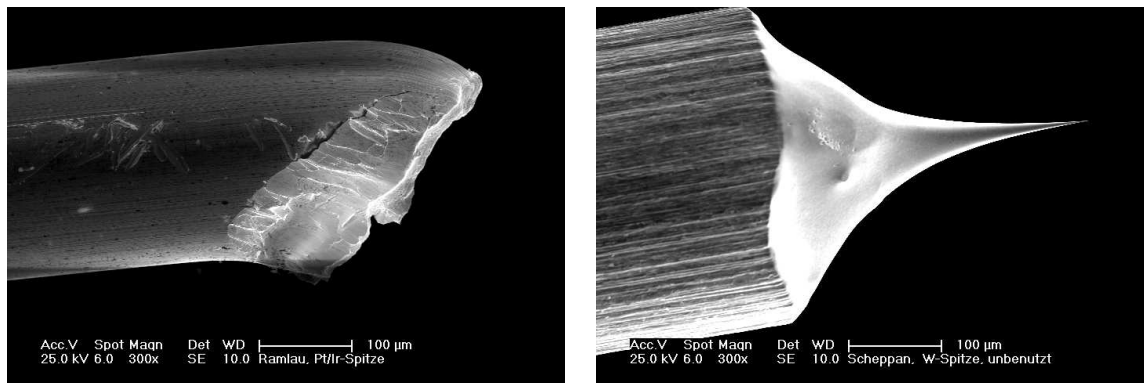


Figure 3.1: Left: Pt80/Ir20 tip cut from 0.25mm wire with some pincers; right: W tip, etched from 0.375mm polycrystalline wire

for spectroscopic experiments, as they might lead to additional spectral features superposed to the measurement data. Small features in the sample's electronic structure close to the FERMI level may not even be resolvable any more. In the presence of the electric field between tip and sample, adsorbates on the tip surface may migrate towards the tip apex ([14], cf. section 3.4.3 of this work). This might completely change the properties of the tip and render the data useless.

The tip material itself also influences the properties of the obtained STM data[12]. According to equation (2.5), the tunnelling current depends not only on the electronic DOS of the sample, but also on that of the tip. A variety of materials has been used for the manufacture of tunnelling tips throughout the history of STM[12]. For most applications, "normal" metallic tips are best suitable. However, some experimental tasks call for more "exotic" materials. For example, superconducting tips have been fabricated from lead, aluminium[15] or niobium[16]. Spin polarised STM can be performed with ferromagnetic or antiferromagnetic probes, as for example with tips made from Ni[17], CrO₂[18] or with tungsten tips covered by a thin layer of iron or chromium[19].

One commonly used tip material is platinum iridium (Pt-Ir). This alloy is particularly suitable for the use under ambient conditions because Pt is relatively inert to oxidation. A fraction of Ir is convenient to make the tip harder. Another advantage is the uncomplicated preparation. With some experience, cutting a piece of Pt-Ir wire with a punch or a pair of scissors (see figure 3.1) gives sufficiently sharp tips to achieve atomic resolution. The success rate is rather low, though. Additionally, Pt-Ir tips are mechanically unstable and therefore only of limited use for spectroscopic measurements. Tungsten is a widely used element for STM tips, and it also fits best to our experimental purposes: Since we intend to work exclusively under UHV conditions, there is no risk of oxidation of clean tips once they are inside the vacuum chamber. Tungsten is suitable for use at low temperatures, since it becomes superconducting only below 10 mK. Above this temperature, the transition metal

has a high and comparatively smooth DOS at the FERMI energy[20], so that tungsten is feasible for spectroscopic measurements. Last not least, tungsten is a very hard and mechanically stable material. For those reasons, the preparation of tungsten STM tips is in the main focus of this work.

The preparation of tips from W single crystals has been reported (see for instance Refs. [21], [22]). Within this work, tips were made from polycrystalline W wire. Such wire is easier to obtain (and therefore much cheaper) and easier to handle than pieces of single crystals. A carefully prepared polycrystalline W tips can end with small single-crystalline grains which are few nanometres in size[23]. High resolution STM data can be achieved even though the crystallographic orientation of those small grains is at angles with the tip axis. We used 99.95% pure polycrystalline tungsten wire with a diameter of 0.375 mm.[24]

On a macroscopic scale, a tunnelling tip has to be stable against mechanical vibrations, as the latter might disturb data acquisition. Long and thin tips are generally less favourable than ones which have a rather short and thick shank and taper rapidly towards the apex. Such tips have higher eigenfrequencies and are generally more stable [12]. Far more important than the macroscopic shape of a tunnelling tip, though, is its structure on an atomic scale. One of the outstanding features of scanning tunnelling microscopy is its unique spatial resolution. If carried out under adequate conditions, one can resolve features which are on the length scale of interatomic distances in solids. One limiting factor for the spatial resolution is the dimension of the probe. Due to the exponential dependency of the tunnelling current upon the distance (cf. figure 2.1), essentially only electrons at the few foremost atoms of the tip contribute to tunnelling. As an ideal tip, one could think of a tip terminating in *one single atom*. The controlled building of such a tip is possible, but it is rather involved[21, 25]. However, it is possible to achieve atomic resolution with tips which *microscopically* have finite radii of apex curvature of about 10 to 20 nm[23, 13]. Tunnelling then occurs at those few atoms which happen to "stick out farthest" from the apex[12]. That is, the sharpest tips do not necessarily yield the highest resolution. But the sharper the tip is on a microscopic scale, the higher is the possibility that the tunnelling current flows only through one of such "minitips" consisting of just few atoms. If tunnelling occurred at two or more spots at the tip apex, the resolution would be reduced, and multiple images of sample features might be superposed in the resulting one[12].

Even if tunnelling took place only at one spot of the tip apex, the atomic arrangement could easily change during scanning which might then cause discontinuities in the data. This is particularly severe for spectroscopic measurements. High energy resolution can only be achieved with appropriately long averaging times. Consequently, STS measurements can easily take several hours. The atomic configuration of the tip should thus be stable throughout such time intervals.

In conclusion, the aim of any tip preparation or conditioning is it to *routinely* obtain tips which are

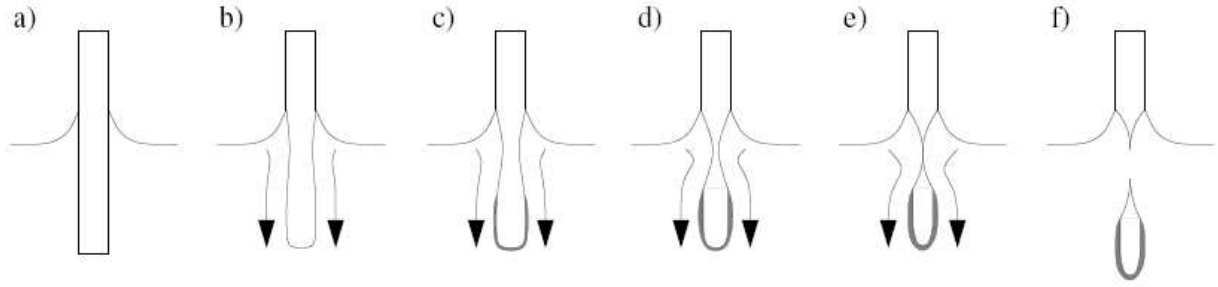


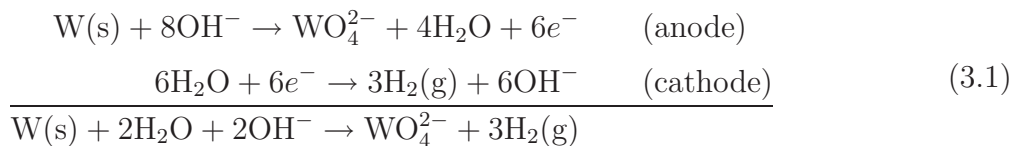
Figure 3.2: Illustration of the electrochemical etching process. b) to e) show the necking close to the meniscus, the flow of WO_4^{2-} ions (arrows) and the formation of a dense WO_3 layer around the wire. In f), the lower part eventually drops off. Figure taken from [29]

- sharp enough to achieve the spatial resolution required
- mechanically stable, and
- free of any disturbing contamination.

In the following section, some aspects of the manufacture of tungsten tips will be outlined. It shall be noted that this is not to be a complete presentation of all possible or conceivable ways to produce high quality tips. It shall rather show the procedures as they were investigated within the scope of this work.

3.2 Electrochemical etching

A generally applied method to produce sharp tungsten tips is electrochemical etching ([26], [27], [28]). A piece of polycrystalline tungsten wire is mounted to a holder and immersed into caustic soda solution (NaOH). The immersion depth can be varied. A ring-shaped stainless steel wire is situated concentrically around the W anode and serves as counter electrode. If a voltage is applied between the two electrodes, the following reaction takes place:



At the interface of electrolyte and air, solid tungsten is oxidised to tungstate anions (WO_4^{2-}) which are soluble in water. At the cathode, water molecules are reduced to hydroxide ions (OH^-) and hydrogen gas. The latter is visible as gas bubbles in the etchant. Figure 3.2 illustrates the evolution of the etching process. The dissolution of tungsten causes the formation of a neck on the wire. The inhomogeneous etching rate leading to the neck has two reasons[27]: Firstly, the surface tension of the etching liquid causes the formation of a meniscus around the W electrode. The etching rate at the top of the meniscus is lower than

further down due to a concentration gradient caused by diffusion of OH^- towards the anode. Secondly, the WO_4^{2-} ions evolving during etching flow towards the lower end of the anode wire and generate a dense viscous layer which prevents the lower part from being etched. As a result of both effects, the etching rate is largest somewhat below the surface of the etchant. As the reaction (3.1) proceeds, the neck becomes thinner and thinner until it finally breaks, and the lower part drops off. The resulting tip has a radius of apex curvature in the order of about 20 to 50nm. To our experience, a too quick etching frequently causes irregularly shaped tips, whereas a too long duration of the process results in rather long and thin tips. Sharp and regularly shaped tips can be obtained with applied voltages of 8-9 V for 3 M NaOH solution. For higher (lower) molarities, the voltage has to be decreased (increased) anti-proportionally. For the wire in use, initial immersion depths of 1.5 to 2.0 mm gave good results. If the wire were dipped too deeply into the etchant, the neck would break too early due to the higher mass of the part below the neck, resulting in less sharp tips. For too small immersion depths, we frequently observed irregularly long and thin tips which were often bended. An explanation could be that the head-and-neck shape is degenerated, and no drop-off can occur.

The etching process has to be terminated immediately after the drop-off in order to prevent the tip from being blunted by further etching. To this end, we monitored the current flowing between the electrodes at a fixed etching voltage. During etching, the area of the W surface which is immersed into the electrolyte is reduced, thus the current decreases nearly linearly with time[26]. The breaking of the neck can be detected as a sudden decrease of the current. In our case, the etching power supply (OMICRON NANOTECHNOLOGY GMBH[8]) automatically terminates the etching process as soon as the current drops below a pre-set threshold value. Alternatively, the jump can be detected by monitoring changes in the differential current. After drop-off, the tip is taken out of the solution and carefully rinsed in de-ionised water, in order to remove remainders of the etchant. Figure 3.3 shows a tip which had not been cleaned after etching. The tip is almost completely covered by sodium hydroxide crystals which may severely disturb STM experiments. After being dried with clean nitrogenic gas, tips are ready to be loaded into the UHV system.

The as-etched tips are rather fragile and have to be handled carefully. During our experiments, a number of procedures turned out to be useful to optimise the tip quality, or to increase their success rate. As a result of its production process, the surface of the polycrystalline tungsten wire contains residual carbon and has an irregular and grooved shaped. At the beginning of the etching, we could observe fibres coming off the wire. Those fibres remained on the surface of the etchant and frequently stuck to the readily etched tip when it was pulled out of the solution. The tips were then often visibly bent and could not be used further. A simple solution to this problem is to shortly pre-etch a larger part of the wire than required for the actual etching step in a separate NaOH solution (a more detailed description is given in the Appendix).

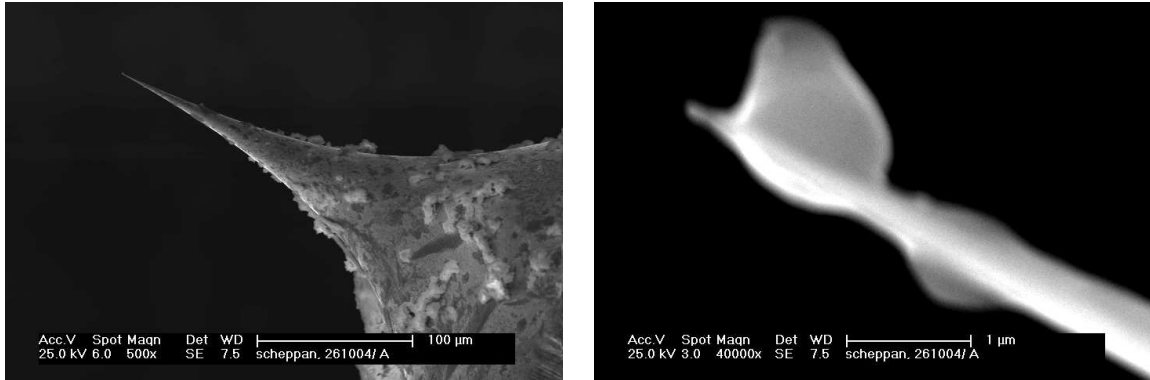


Figure 3.3: A tungsten tip which had not been rinsed after etching

As described, the NaOH surface forms a meniscus around the tungsten wire during etching. As the neck in the wire deepens, the meniscus can drop to a lower position, often leading to the formation of a second neck below the first one. This may result in oddly shaped, mechanically unstable tips. It is therefore profitable to observe the etching process through an optical microscope and to lower the tip by about 0.1 mm after a few minutes in order to reduce the surface tension. The reduced height of the meniscus is also profitable for the tip shape, since the aspect ratio of the etched tip is mainly determined by the shape of the meniscus, and a lower meniscus results in shorter tips[27]. The observation of the process may cause additional vibrations which might disturb the etching, especially in an advanced state when the neck is already thin. For this reason we situated our etching tool on top of a heavy stone block based on rubber feet. Moreover, we put a plexiglass shield to protect the NaOH surface from air flow. In this way, the vibrations of the lower part of the etched wire could be reduced visibly. Another undesired effect results from the H_2 gas evolving at the cathode according to the reaction (3.1). Due to the inhomogeneous electric field between the concentric electrodes, the gas bubbles migrate from the cathode towards the tungsten anode where they frequently disturb the etching process. We found that the amount of gas bubbles which actually reach the anode depends on the immersion depth of

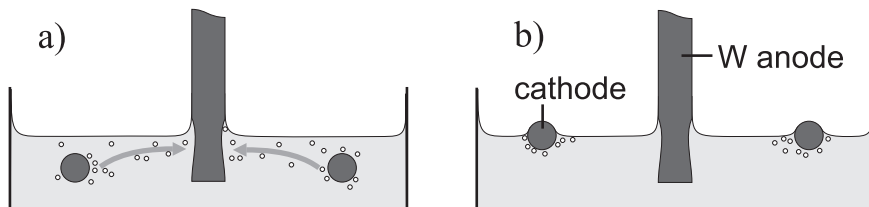


Figure 3.4: Bubbles of H_2 gas evolving at the cathode can migrate towards the W anode and disturb the etching (a). If the cathode is only touching the surface of the etchant, almost no gas bubbles can reach the anode (b)

the counter electrode into the NaOH solution. This is illustrated in figure 3.4 If the cathode is mounted in such a way that it is just touching the surface of the etchant, almost no gas bubbles are visible at the anode.

A major disadvantage of electrochemical etching is that tips prepared in this way are covered by a dense oxide layer. Hence, additional treatment is necessary after etching. This topic will be addressed in detail in section 3.4. The rate of tips which, after etching, could be used for any further treatment was about 50%. If the tips had been stored for one day or longer in air, the rate would have been worse, probably due to proceeding oxidation. Storing the tips in ethanol seemed profitable, though. Firstly, the tips did not oxidise any further, and the fraction of useable tips was increased. And secondly, any organic contaminants were removed from the tip at the same time.

3.3 Means of tip characterisation

In order to study the efficiency of tip preparation methods, it is necessary to characterise tips in a reproducible manner. The ultimate way to test the quality of a STM tip would be to perform tunnelling experiments with well-known reference samples. With a blunt or strongly contaminated tip, it would not be possible to achieve stable atomic resolution. Multiple tips cause anisotropic or multiple imaging of sample features. Spectroscopic measurements can provide information on the presence of additional non-metallic layers on the tip surface. However, STM measurements are generally quite time consuming, and a *differentiated* characterisation of the tip by STM is not easily possible because of the variety of parameters which influence the STM data.

A more direct way to determine the tip morphology is to visualise them. With an optical microscope one can see whether a tip is bent or irregularly shaped only on a macroscopic scale, which anyway is often useful. By means of *scanning electron microscopy (SEM)*, the shape can be probed in the sub-micrometre range. The actual atomic arrangement is not accessible, though. SEM experiments are time consuming as well, and they have to be carried out *ex situ*. Therefore, it is convenient to have a means to check quickly on tip sharpness and cleanliness already *before and during the conditioning process*. In this way, one can quantify the impact a certain treatment method has on a tip. One way to achieve this is to perform *field emission experiments* which will be described in the following.

In a metal, electrons reside inside a potential well, which is mainly due to their interaction with the positively charged metal ions. The potential can classically be described as

$$U(x) = \Phi - \frac{e^2}{4x}, \quad x > 0,$$

if the metal fills the half-space $x \leq 0$. Φ denotes the work function of the metal surface. The $1/x$ term describes the interaction of an electron outside the metal with its mirror charge. If now an electric field $\mathbf{F} = F\mathbf{e}_x$ is applied, the potential will be influenced as follows:

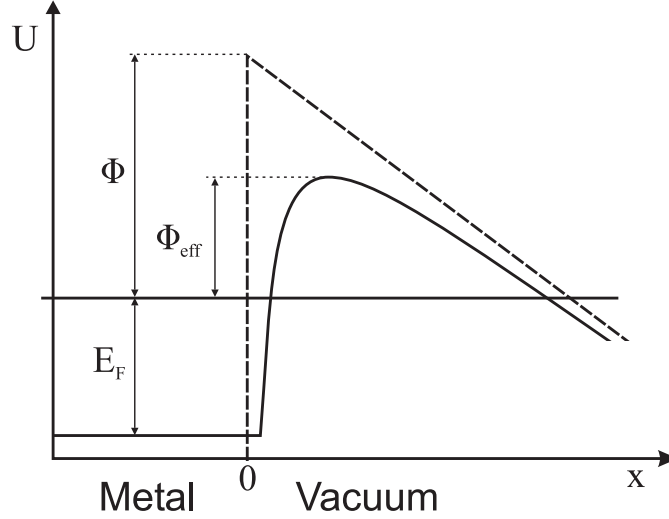


Figure 3.5: The potential experienced by an electron at a metal surface in the presence of an electric field (solid line). The dashed line is the potential *without* the effect of the mirror charge.

$$U(x) = \Phi - \frac{e^2}{4x} - Fex, \quad x > 0. \quad (3.2)$$

The resulting effective potential is sketched in figure 3.5 (the solid line for $x > 0$). An electron close to the Fermi level experiences a more or less triangular-shaped potential barrier which it can overcome by tunnelling. The higher the magnitude of the field, the narrower is the barrier, resulting in a higher transmission probability \mathcal{T} . In 1928, FOWLER and NORDHEIM published an expression for the field emission current density j as a function of F and Φ [29, 30, 31, 32]:

$$j = \frac{e^3}{2\pi h} \frac{(E_F/\Phi)^{\frac{1}{2}}}{\xi^2(E_F + \Phi)} F^2 \exp \left\{ -\frac{8\pi\sqrt{2m}}{3eh} \xi \frac{\Phi^{\frac{3}{2}}}{F} \right\} \quad (3.3)$$

The parametre $\xi \leq 1$ is a correction which accounts for the interaction of an electron outside the metal with its mirror charge, i.e. the deviation from the simple triangular potential well (dashed line in figure 3.5. Note that ξ depends only on the lowering of the potential barrier $\Phi_{\text{eff}} = \Phi - \sqrt{eF}$ due to the applied field[31]. The FOWLER-NORDHEIM equation (3.3) describes field emission from a infinite plane emitter under high electric fields in the low temperature limit, but it can also be used to approximate the emission from a tip-shaped metal at higher temperatures. The idea is now to relate the emission current to the geometry of the emitter. Approximating the tip geometry by a sphere of radius r at the end of a cone-shaped shank, the electric field at the tip surface can be written as[33]

$$F = \frac{V}{kr}, \quad (3.4)$$

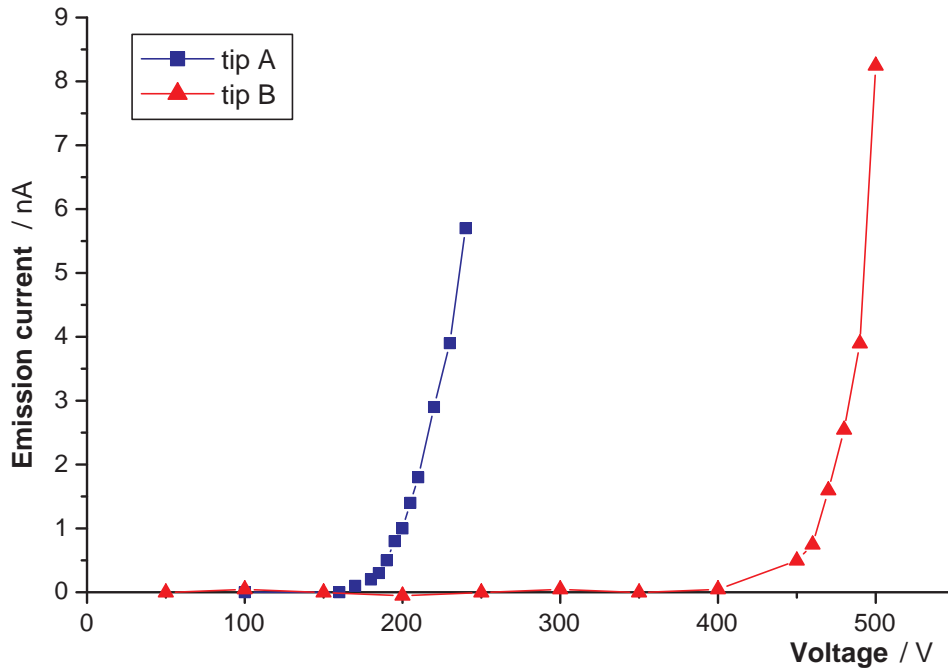


Figure 3.6: Field emission current vs. voltage for two W tips

where V is the applied voltage, and k is a geometrical factor which takes the shank into consideration. An appropriate value is $k \approx 5$ [33, 29]. Inserting numerical values for the constants in equation 3.3 yields for the total emission current

$$I \propto \left(\frac{V}{r}\right)^2 \exp\left\{-6.8 \cdot 10^9 \Phi^{3/2} \frac{\xi k r}{V}\right\} \quad (3.5)$$

for Φ in eV , V in volts, and the tip radius r in metres.

Now figure 3.6 shows the *measured* field emission current vs. voltage of two tungsten tips. The measurement setup is illustrated in 3.7: We placed the tip a few millimetres away from a counter electrode, applied a positive high voltage to the tip, and measured the emission current between tip and electrode. A detailed description of the technical realisation will be

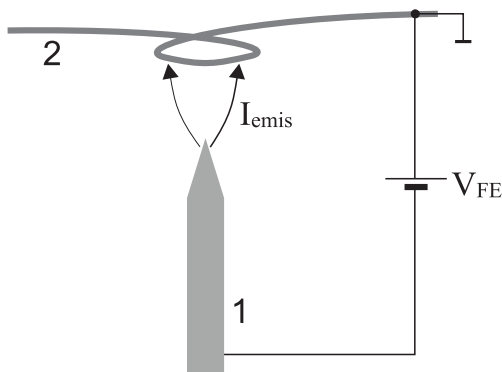


Figure 3.7: Schematic of the setup configuration for measuring the field emission from a tip; 1-tip, 2-counter electrode.

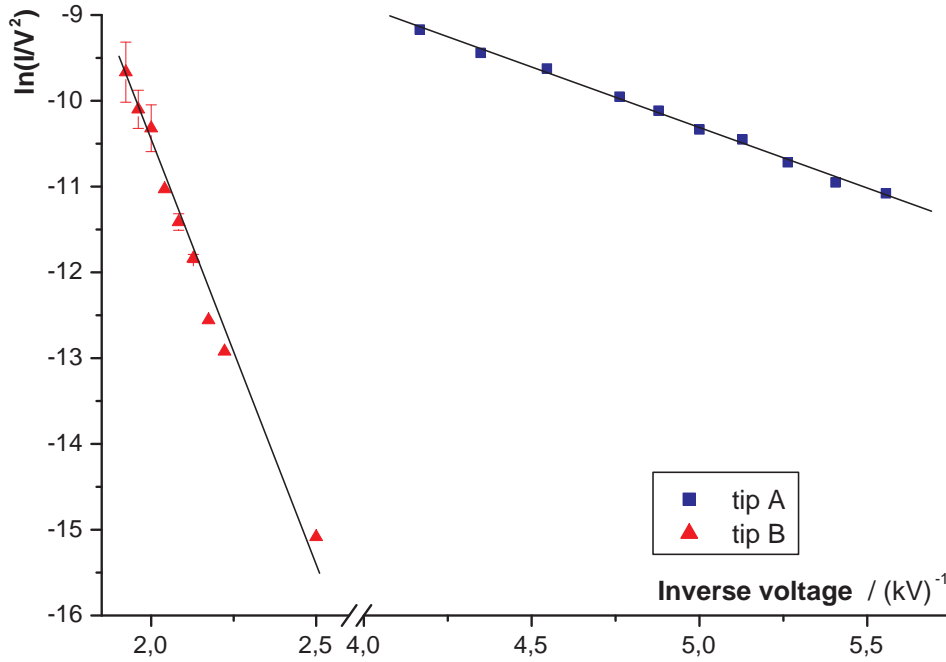


Figure 3.8: Fowler-Nordheim plots for the same tips as in figure 3.6; the sharper tip A has a smaller (negative) slope than a less sharp one B

given in section 3.5. In agreement with equation (3.5), the current is negligibly small below a certain threshold voltage, whereas it increases quickly above. However, this threshold is different for both curves. Since a smaller apex radius results in a higher electric field, cf. equation (3.4), the voltage required to draw a certain current is lower for a sharp tip than for a blunt one. This suggests that tip A in figure 3.6 is sharper than tip B. Moreover, the radii of the tips can be extracted from the $I - V$ characteristics as follows: Equation (3.5) can be transformed into

$$\ln\left(\frac{I}{V^2}\right) = -6.8 \cdot 10^9 \xi k r \Phi^{3/2} \cdot \frac{1}{V} + \text{const.} \quad (3.6)$$

That is, the left hand side is a *linear* function of $1/V$. In figure 3.8, $\ln(I/V^2)$ is plotted vs. $1/V$ for both tips (so-called FOWLER-NORDHEIM plots). The linear behaviour, supported by the linear fits (black lines), confirms the validity of equation (3.5). The tip radii can be estimated from the slopes of the graphs. Using an average work function $\Phi = 4.5$ eV for tungsten, $k = 5$ and $\xi = 1$, one gets $r = (4.3 \pm 0.1)$ nm for tip A, and $r = (29.6 \pm 1.4)$ nm for tip B. Figure 3.9 is an SEM image of tip A, from which we graphically found a radius of (14 ± 6) nm. The considerable difference of the two results can have a number of reasons. On the one hand, it is very difficult to determine the tip radius from an SEM micrograph because of the limited resolution. Very small features such as clusters of few atoms cannot

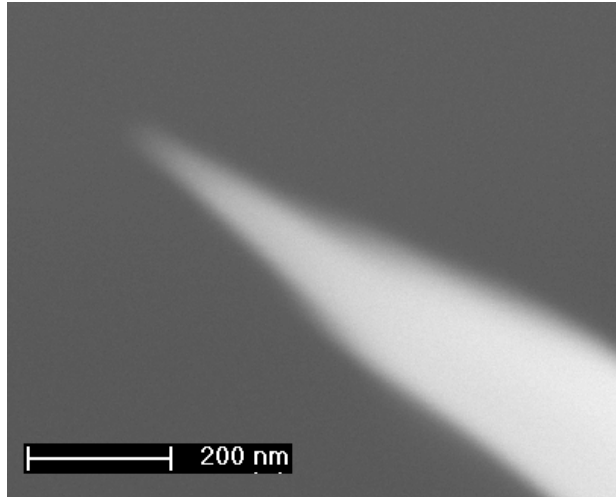


Figure 3.9: SEM image of tip A in figures 3.6 and 3.8. The apex radius is ($r = 14 \pm 6$) nm

be resolved. On the other hand, the values for the constants in equation (3.6) were chosen rather arbitrarily. In particular, the correction ξ has not yet been considered at all. With typical voltages of $V = 200$ V and $r = 4$ nm for tip A, the field at the tip apex is about 10^8 V/cm, which, according to NORDHEIM[31], leads to a correction factor of $\xi \approx 0.4$. Including this into the calculation, the radius extracted from figure 3.8 for tip A becomes $r = (10.9 \pm 0.3)$ nm, i.e. 78% of the value obtained from SEM, which is in reasonable agreement. It shall be noted that it was possible to get atomic resolution images in STM with this very same tip. Unfortunately, there is no SEM data available for tip B. However, estimating ξ in this case would lead to a corrected radius of (37.5 ± 1.8) nm.

Besides extracting the tip radius from a FOWLER-NORDHEIM plot, there is an even easier way to obtain a crude estimate of the tip sharpness by field emission. For this quick test it is sufficient to measure just *one point* at the $I-V$ curve. For a fixed emission current, equation (3.5) induces a *linear dependency* of the voltage upon the radius. This can be seen as follows: Let the function f be defined such that $I(V, r) \equiv f(V/r)$. The inverse function of f is

$$\begin{aligned} f^{-1} : \quad y &\mapsto f^{-1}(y) = x, & \text{such that } f(x) &= y \\ &\Rightarrow f^{-1}(I(V, r)) &= \frac{V}{r} \end{aligned}$$

That is, for a fixed value I_{th} of the current, the threshold voltage is proportional to r :

$$V_{\text{th}} \equiv V(I_{\text{th}}) = f^{-1}(I_{\text{th}}) \cdot r \quad (3.7)$$

So, in order to estimate the tip sharpness, we placed the tip in the setup described above and measured the voltage V_{th} required to draw 1 nA from the tip. The value 1 nA was chosen such that it lay above the sensitivity limit of our measurement, but still was sufficiently low

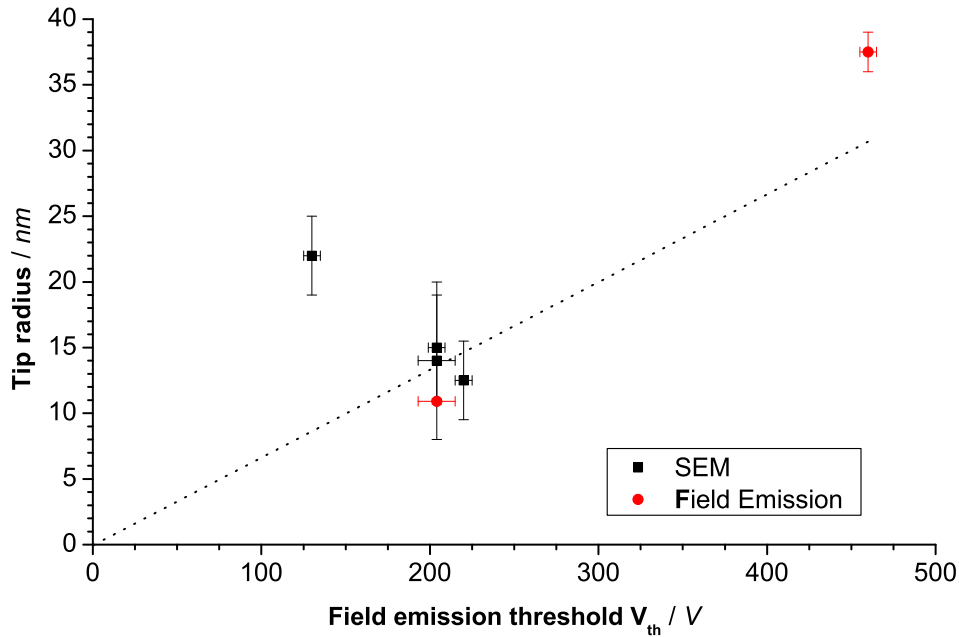


Figure 3.10: Tip radii vs. field emission threshold voltage; the radii were determined from SEM images or Fowler-Nordheim plots. The dashed line is the graph $r[\text{\AA}] = \frac{2}{3}V_{th}[\text{V}]$.

that the tip was not endangered to be harmed. For a number of tips we both measured field emission and determined the apex radii from SEM images, in order to find the constant of proportionality in equation (3.7). The results can be seen in figure 3.10, The figure also includes the radii extracted from FOWLER-NORDHEIM plots for the two tips A and B mentioned above. With the few data points available it would be highly speculative to establish any relation between tip radius and threshold. The expected linear dependency may as well be conceivable as a linear one, as it has been revealed by DE RAAD et al.[34]. Assuming nonetheless a linear behaviour, one can graphically estimate an upper and a lower limit of the slope of the graph. Taking the mean value of these two slopes, it is possible to conclude a *rule of thumb*:

The tip radius in \AA is roughly $\frac{2}{3}(\pm \frac{1}{6})$ of the measured threshold in volts.

This relation is depicted as a dashed line in figure 3.10. More measurements are necessary to confine this statement.

For testing purposes, a tip which had shown a threshold voltage of about 500 V was purposely blunted by crashing it against the counter electrode. Afterwards, no more field emission could be detected up to 1kV. This proves that electrons are indeed emitted from the tip apex instead of some other sharp edges at the tip or the tip holder. In order to check on the influence of the stage geometry on the field emission data, one and the same tip was

placed in different positions with respect to the looped counter electrode. Increasing the relative distance of tip apex and counter electrode by 1 mm caused a change in threshold voltage from 230 V up to 290 V. Moving the tip parallel to the loop plane by withdrawing it from the stage for up to 1 mm changed the threshold by as little as 5 V. That is, there is some influence of the geometry of the experimental setup on the field emission, but it is not crucial for our purpose: estimating the tip sharpness.

The results presented in this work are based on experiments with more than 70 tungsten tips. This only includes "successful" experiments, i.e. only tips which, after etching, were transferred into the UHV chamber, exposed to some conditioning and characterised using one or more of the methods mentioned above. Not included are the countless tips which were lost at some point of the experiment before getting any reliable result. About 50 tips were tested in STM itself. Mostly we used graphite as a standard sample, but also other samples were tested, such as Au(111) single crystal, NbSe₂ and manganite samples. Selected results are presented in chapter 4. In addition to the STM work, more than 25 tips were examined by means of SEM. The measurements were carried out *ex situ* in an XL30 microscope, manufactured by Philips Electron Optics, with a LaB₆ cathode. Field emission tests were only available after the completion of the corresponding facilities described in section 3.5. Field emission data is available for about 40 tips.

An exact quantisation of the tip shape is not easily possible with the methods in use. Further information might be gained from transmission electron microscopy (TEM) measurements. However, it is doubtful whether this would be useful because a sharp tip is not a *guarantee* for high resolution STM. Nevertheless, field emission is a simple and quick tool to check whether a tip may *at all* be suitable for STM, and one can observe *changes* in the tip sharpness due to some treatment procedures. Atomically resolved STM images could be achieved with tips from a wide range of field emission voltages V_{th} from 130 to 430 V. Best results were obtained between 150 and 300 V. Following the rule stated above, these tips had apex radii between 7.5 and 15 nm (or even up to 22.5 nm, assuming the upper bound). Interestingly, a number of tips which had a very low $V_{\text{th}} \lesssim 150$ V did not show any decent tunnelling at all. One reason for this might be that very sharp tips are mechanically unstable. It might also be that the tip had multiple sharp tips or sharp edges at the apex, which led to a high field emission, but were unfavourable for STM (cf. section 3.1). Above 400 V, we hardly obtained good STM results.

3.4 Methods for *in-situ* tip conditioning

Electrochemical etching yields tips which are microscopically sharp. As mentioned in the previous section, it is possible to achieve atomic resolution with tips which have apex radii in the order of 10 nm. It is the aim of tip conditioning to create tips which are as sharp as that, but equally important is it to get rid of any contaminants which may disturb tunnelling. During etching and storing the tips under ambient conditions, many kinds of contaminations can gather at the tungsten surface. In particular, a dense insulating layer is evolving during the etching procedure[13, 27, 29]. This layer mainly consists of tungsten trioxide WO_3 , but also carbon, NaOH conglomerates and $\text{WO}_3\text{-Na}$ microcrystals have been found[35]. The thickness of these layers can be up to 20nm at the apex[13, 34]. Various techniques have been suggested to remove these additional tunnelling barriers and to sharpen tips. The methods include direct and indirect annealing, chemical treatment, sputtering, ultrasonic cleaning and the application of high electric fields. Not all of the methods seemed to be promising or applicable to our experimental setups. Therefore, the subsequent presentation solely includes the methods we investigated at our instruments.

3.4.1 Tip annealing

One widely used way to treat as-etched tips is to anneal them *in situ*. Water and other solvents are removed at relatively low temperatures already. Above 750 to 800 °C, a reduction of the tungsten trioxide takes place:



The tungsten dioxide is volatile. As the WO_3 layer is removed from the tip, a pure tungsten surface is generated. This reaction takes place far below the melting temperature of tungsten (3410 °C). However, elevated temperatures also enhance the diffusion of surface atoms. This can lead to blunting of the tip below the melting point[22]. Hence, it is necessary to protect the tips from being overheated.

We performed tip annealing in two different ways: Direct resistive annealing and heating by electron bombardment. For direct heating, the tip shank is brought into mechanical contact with a tungsten filament. The latter is resistively heated, glowing bright orange. We were not able to observe whether or not the tip itself was glowing, since the filament was shining far too brightly. However, comparing the brightness of the filament with and without the tip touching, it could easily be seen that some heat was flowing into the tip in the former case. The direct annealing method is relatively easy to perform. A piece of 0.2 mm tungsten wire used as a filament inside the vacuum chamber is heated by means of a standard dc power supply. A disadvantage, however, is that the process is difficult to control. The whole tip shank is being heated up, and the exact heat flowing to the apex cannot be predicted. Tips may accidentally be molten if heated too strongly. When bringing

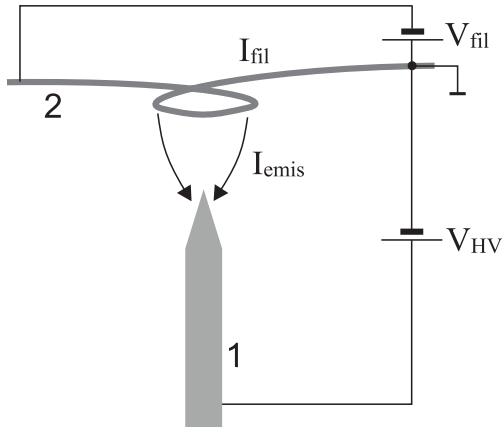


Figure 3.11: Schematic of the setup configuration for tip annealing by electron bombardment; 1-tip, 2-filament. Note the reversed polarity of the voltage as compared with the setup for field emission (Fig. 3.7)

the tip into contact with the filament, one can easily bend or crash the tip. By applying too much force, one might even break the filament since tungsten becomes brittle once it has been annealed. Tips which had only been treated with this method did in general not show good STM results. Probably, most of them were either molten (as it was observed by SEM) or not affected at all. Nonetheless, if carried out carefully, this direct heating procedure is useful as a first gentle treatment step or in connection with other methods (see below). Field emission measurements often become more stable after heating the tip *gently* for few minutes, probably due to the removal of water from its surface.

A more subtle heating method uses electron bombardment[13]. To this end, the tip is placed in front of a looped filament wire as illustrated in figure 3.11, such that the distance is a few millimetres. A detailed description can be found in chapter 3.5. Note that the setup is similar to the one used for field emission experiments, cf. figure 3.7. In contrast to the latter, the filament is here resistively heated such that electrons are thermally emitted. In addition, a positive high voltage V_{HV} with respect to the filament is applied to the tip, i.e. the polarity is reversed as compared to field emission. Under the influence of the electric field, the electrons are accelerated towards the tip. The density of impinging electrons is highest at the very tip where the field gradient is largest. Entering the metal, the electrons are decelerated down to the metal's FERMI velocity. The difference in energy is transferred into heat and causes the tip to be heated up locally. Note that the high voltage should be applied to the tip, leaving the filament on virtual ground. If otherwise a negative HV were applied to the filament, electrons would be accelerated not only towards the tip, but also towards the surrounding chamber. Hence the number of electrons available for heating would be drastically reduced. Moreover, it would be impossible to measure the electron current which actually flows to the tip.

The annealing process is determined by the heating power $P = V_{HV} \cdot I_{emis}$. We exposed W tips to powers between $10 \mu\text{W}$ and 10mW , V_{HV} ranging from 0.2 to 2.0kV . The tips were usually treated for 30 to 60 seconds. Within this range, the annealing time did not seem to have any influence: A tip that had been annealed for 30s already was not affected

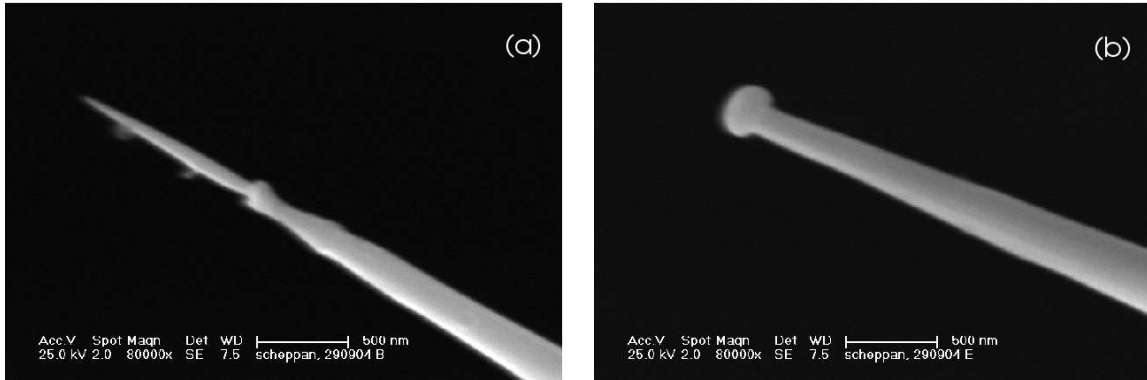


Figure 3.12: Tips annealed by electron bombardment. (a) $V_{\text{HV}} = 250 \text{ V}$, $I_{\text{emis}} = 0.1 \mu\text{A}$, $t = 30 \text{ s}$; a neck has formed during annealing due to the removal of W_2O_7 and W . (b) the tip was molten. (b) $V_{\text{HV}} = 1.6 \text{ kV}$, $I_{\text{emis}} = 2.0 \mu\text{A}$, $t = 50 \text{ s}$; the tip was probably molten at the apex

by further annealing for 60s, according to field emission test.

Among the tips exposed to this annealing procedure, a number of 15 was eventually tested in STM (not including those tips which were later found to be molten during annealing). Five of those tips gave atomic resolution. The annealing parameters of these good tips were spread over a rather large range, between $16 \mu\text{W}$ and $500 \mu\text{W}$ at voltages from 200 to 350 V. Figure 3.12(a) shows an SEM image of a tip which has been heated for 30s at $25 \mu\text{W}$, 250 V. The formation of the neck was probably caused by the removal of elementary tungsten during heating, as it was already reported in literature[13]. We could not correlate the occurrence of this effect to the preparation conditions, though. However, we concluded from this image that tips are indeed already affected by annealing with very low powers. SEM images have also revealed that treatment with too high a power leads to blunting of the tip. An example can be seen in figure 3.12(b): The tip was heated up to 3 mW and seems to be molten at the apex. In order to further understand this blunting, a number of tips was annealed repeatedly with gradually increased power, after each step checking on the tip sharpness by field emission. A representative curve can be seen in figure 3.13. The tip radius reduces linearly with power up to some minimum, above which the tip is blunted. Note that the tip is not molten at once, but it is blunted *gradually*. An explanation could be that heating enhances the diffusion of surface atoms away from the apex towards reach an energetically favourable state[22]. In this case one would expect an exponential increase of the tip radius, as diffusion constants D generally take the form[36]

$$D = D_0 \exp[-E/k_{\text{B}}T]. \quad (3.9)$$

More data is needed to support this supposition. Note that the power value at which this blunting started was not the same for different tips investigated. It seems that sharp tips

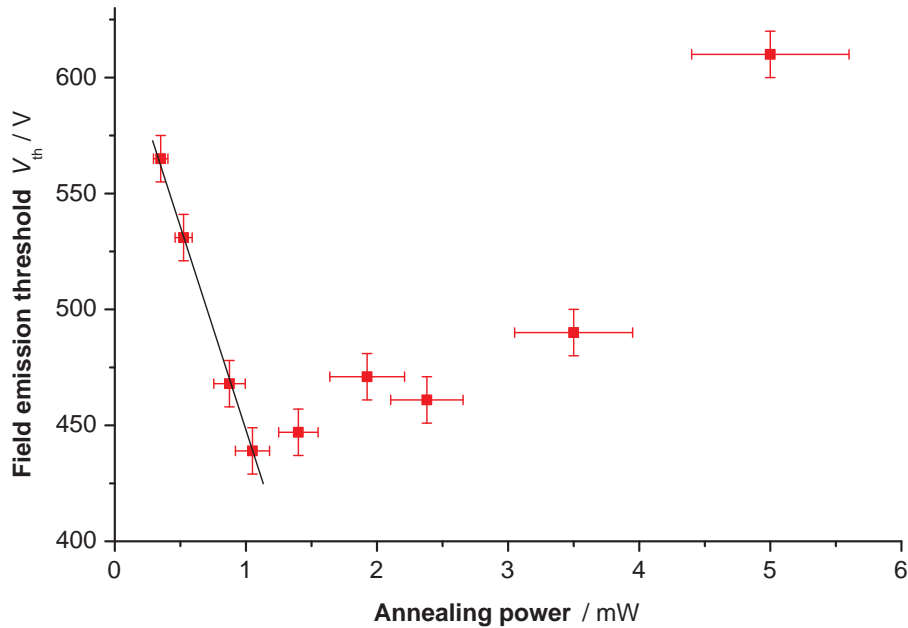


Figure 3.13: Influence of the annealing power on the tip sharpness: The tip was annealed with gradually increasing power. After each heating cycle, field emission was measured.

start blunting at lower powers than less sharp ones, but so far, we could not correlate the situation of the minimum to properties of the tip. Typically, blunting starts between 0.5 and 1.5 mW , in some cases even at lower power. More measurements are necessary to confine this upper limit. In order to anneal the tips effectively without risking to blunt them, powers between 20 μW and 100 μW ($I_{emis} = 0.1$ to $0.5 \mu A$ at 200 V) seem to be most promising. Within this work, only a few experiments were carried out at very high voltages (>1 kV). The effect of high electric fields on the annealing process may be worth studying in more detail (compare also section 3.4.3).

In conclusion, heating by electron bombardment seems to be more suitable for the fragile STM tips. The annealing conditions are well-controllable, and only the very tip is affected by this method. According to the reaction (3.8), tungsten oxide as well as elementary tungsten are removed, leading to a cleaning and sharpening of the tips. However, the sharpening effect is limited to the removal of a rather thin layer, and an initial sharpness of the tips is therefore required to achieve good results in STM. The overall rate of tips which gave good results in STM was rather low. The reason might be that tips annealed within a too wide range of heating parameters are included. Not all tips could be imaged in SEM after the STM experiments to reveal whether they were blunt. Restricting the procedure to the parameter range in which good results were obtained is likely to improve the success rate.

3.4.2 Self sputtering

Another means to clean and sharpen tungsten STM tips is ion sputtering[23, 13]. If a target surface is bombarded by energetic ions (typicall 30-50 eV), atoms, secondary ions or clusters of atoms can be ejected from the surface. This sputter process is well-established for removing of materials, e.g. for cleaning or depth-profiling of surfaces. Mostly, noble gases are used to avoid any chemical reaction with the surface to be treated. The use of a typical ion gun would cause quite some technical effort. For tip-shaped targets, a method easier to realise is *self sputtering*, as it was initially applied for field-ion microscopy (FIM) tips[33]. For this sputtering procedure, the tip is situated in a setup similar to the one used for field emission, cf. section 3.3. Subsequently, clean noble gas is introduced into the vacuum chamber, and a high voltage V_s is applied between tip and counter electrode such that electrons are field-emitted from the tip. Those electrons, in turn, can ionise noble gas atoms. Under the influence of the high electric field, the positively charged ions are accelerated towards the tip and sputter its surface (figure 3.14).

In our experiments, we used argon and neon as sputter gases. Comparing the results, it seemed that sputtering with Ar gas produced less reliable tips, probably due to the high atomic mass of Ar. This corresponds to results found in literature[37]. The mass of helium ions, however, is too low to achieve appreciable sputter rates[33]. Therefore, we chose to only work with Ne as sputter gas in later experiments.

During sputtering, we monitored the sputter voltage V_s as well as the current flow between tip and counter electrode. Note that the Ne^+ ion current is about three orders of magnitude smaller than the electron emission current I_{emis} and can therefore be neglected[37]. In order to keep a constant sputter rate and to avoid damages to the tip caused by too high currents, V_s was controlled such that the current remained nearly constant throughout the sputtering process. A typical $V_s(t)$ curve is shown in figure 3.15. As described in section 3.3, the voltage which is required to draw a certain emission current from the tip depends on the tip apex radius r . Hence, the drop of V_s over time indicates that the tip was sharpened.

Figure 3.16 presents SEM images of tips for which sputtering had been terminated at different states of the process. The first tip (a) shows a neck which was formed during sputtering at a distance of a few hundred nanometres away from the apex. The formation of a neck occurs due to a larger sputtering rate at the shank as compared to the apex. According to SCHILLER et al.[37], this may have several reasons: Firstly, the density of

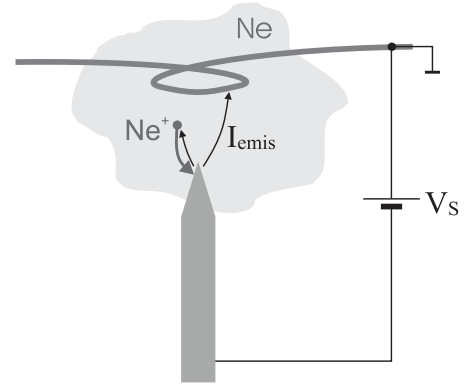


Figure 3.14: Setup for Self-sputtering

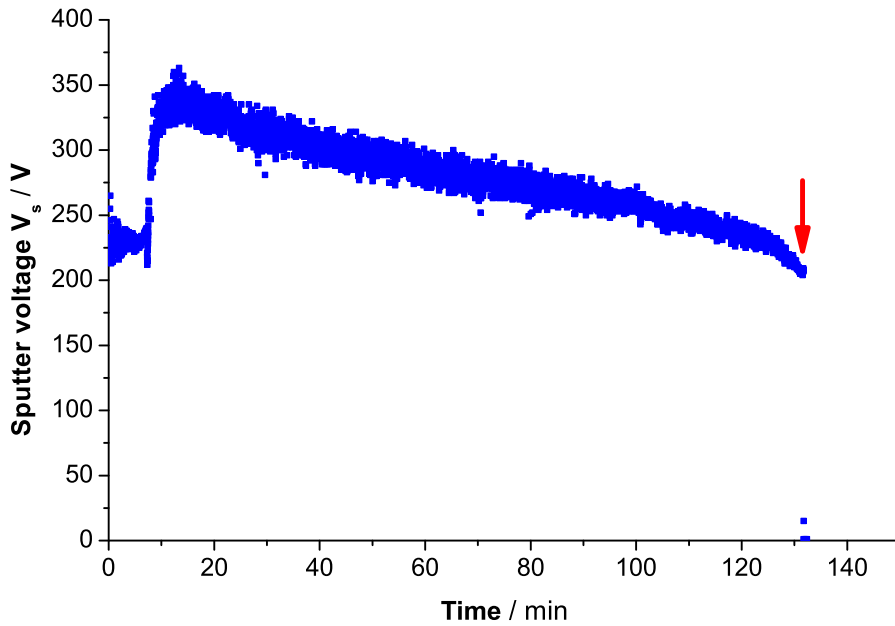


Figure 3.15: Sputter voltage V_s vs. time. The decrease of V_s indicates that the tip was sharpened. The process was automatically terminated immediately after a sudden drop in V_s due to a decapitation of the tip (see below), which is marked by the arrow. Note the down-turn and the reduced noise level of the curve just before this switch-off.

impinging ions is largest somewhat below the apex. This is because the emitted electrons have a distribution of velocity components tangential to the electric field[38]. Electrons emitted from one point of the tip surface result in an angular distribution of impinging Ne^+ at the tip surface. Due to the different masses, the Ne^+ ions and the electrons creating them do in general *not* follow the same trajectories. This is why the maximum value of the ion distribution is further away from the apex than the electron emission point. - Secondly, the ions strike the tip surface at the shank at some angle instead perpendicularly. This enhances the sputter rate, as sputtering is most effective at about 60° . SCHILLER et al. found that neck-formation only occurs for electron emission currents $< 20 \mu\text{A}$. For higher currents, the distribution of impinging ions at the shank would be smeared out because the density of ions would be higher as well, leading to an enhanced Coulomb interaction among the ions.

Such neck-and-head shape would of course be unfavourable for a STM tip. It causes mechanical instabilities which show up as low-frequency noise in STM data. As sputtering proceeds, though, the neck deepens (figure 3.16(b)) until the part above the neck is eventually torn off ("decapitation"). This happens when the material's flow stress at the neck is overcome by the force acting on the head in the electrostatic field. The remaining part of the tip would have a much sharper apex than before. For this reason, these decapitation processes are connected with sudden drops of the sputter voltage in the order of 50 V[34].

Detecting these voltage jumps, it is possible to automatically terminate the sputter process immediately after a decapitation, resulting in very sharp and clean tips with apex radii of few nanometres[37], cf figure 3.16(c). Notably, such decapitation of the tip is usually connected with a typical shape of the V_s vs. time curve. Just before the decapitation, one can often observe an enhanced sharpening rate (indicated by a down-turn of the curve), along with a reduction of the noise, see figure 3.15. In few cases, the curve also turned up instead of down shortly before a sudden voltage drop.

Among the tips treated by self-sputtering, a number of 31 were eventually tested in STM. For ten of them, argon was used as sputter gas, while all the others were sputtered with neon. Six of the ten tips treated with argon gave atomic resolution on graphite. However, only for one of them the quality was really satisfactory, that is low noise, sharp features and no double imaging. From the 21 tips treated with neon gas, twelve showed atomically resolved images on graphite or gold, six of them in really high quality. Best results were obtained with tips that showed a field emission threshold V_{th} between 180 and 250 V, indicating apex radii of about 10 to 15 nm (cf. figure 3.10 in section 3.3), but occasionally atomic resolution was obtained up to $V_{th} = 400$ V. On the other hand, we noted that tips which appeared very sharp ($V_{th} \lesssim 150$ V) frequently did not yield any reasonable resolution at all, as it was mentioned in section 3.3 already. Furthermore, good results with sputtered tips were almost exclusively achieved after the occurrence of a tip decapitation described above. Figure 3.17 shows two STM topography images of HOPG. The images were recorded with one and the same W tip *before* and *after* a sputter treatment which ended with a decapitation, evidencing a distinct improvement in resolution. Contrariwise, tips that had been sputtered for a longer time without such decapitation did in general not show reasonable imaging. We frequently noticed considerable oscillations in the order of 25 Hz which were superposed to the tunnelling signal. Those disturbances were evidently caused by the tip. Probably, a pronounced neck caused by sputtering as in figure 3.16(b) rendered the tip mechanically unstable. Similar observations can be found in literature[13]. Attempts to sputter tips just for few seconds in order to remove contaminants without the formation of any neck did not succeed either.

Clearly, a higher electron emission from the tip leads to a larger sputter rate. In order to achieve appreciable sputter rates and at the same time ensure that the formation of a neck is possible, we chose emission currents between 5 to 20 μ A. The power supply in use (cf. section 3.5.3) is limited to one kilovolt. As a rule of thumb, the voltage required for a field emission of 10 μ A is about 1.5 to 2 times higher than for 1 nA. Hence, only tips with an initial field emission threshold $V_{th} \lesssim 600$ V were eligible for sputter treatment *in our setup*.

During sputtering, the penetrating ions cause damages at the tip surface, frequently resulting in the formation of multiple tips[13]. Subsequent annealing can cure such damages and bring the tip into a more stable state[23]. We found that for tips which had been annealed after self-sputtering, the tunnelling current was generally less noisy, the resolution

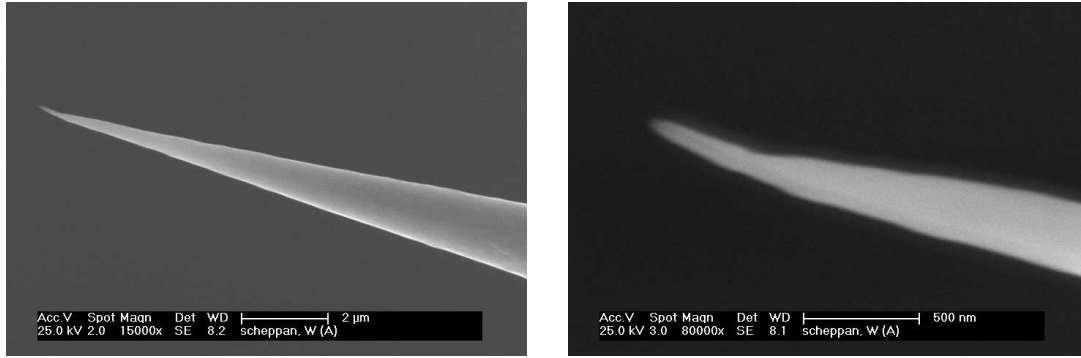
was better and the tips were more stable during tunnelling. We used gentle direct resistive annealing for few minutes, the filament only glowing red to dark orange. Due to technical difficulties, we were so far not able to combine self-sputtering with electron beam heating. However, this combination seems to be quite promising since electron annealing offers a number of advantages over direct annealing, as it was outlined above. The self-sputtering process itself can be repeated for one and the same tip. Thus it is possible to recover tips which have been crashed during scanning. The only condition is that the tip is still sharp enough to draw an emission current which is sufficiently high to reach appreciable sputter rates.

The pressure of the sputter gas itself was not found to be not crucial for self sputtering. Indeed, it only influences the speed of the process, as the sputter rate is proportional to the gas pressures[33]. The energy of the impinging ions, though, is nearly independent of pressure. This is because most of the ionisations occur within a distance less than ten apex radii (i.e. few hundred nm) from the tip, whereas for a typical pressure of 10^{-3} mbar, the distance of two gas molecules is few micrometres[38, 33, 37]. In our experiments, we used Ne gas pressures between $2 \cdot 10^{-5}$ and $5 \cdot 10^{-5}$ mbar. We could not observe any influence of the Ne gas pressure on the tip performance. Apart from its pressure dependence, the duration of sputtering process varies strongly for different tips. A decapitation of the tip can occur after few minutes, occasionally it can take up to two hours, though (cf. figure 3.15). This may have a number of reasons. Simple geometric consideration reveals that the tip's cone angle strongly influences the amount of material that has to be removed for a decapitation. However, the duration of the sputter process could so far not be evidently correlated to any tip properties or working conditions. Note also that the sharpening of the tip does not necessarily happen monotonously. We frequently observed increases of the sputter voltage during sputtering, as it is visible in figure 3.18. Usually, the voltage increased by less than 100 V, and in most cases it started again to drop soon after.

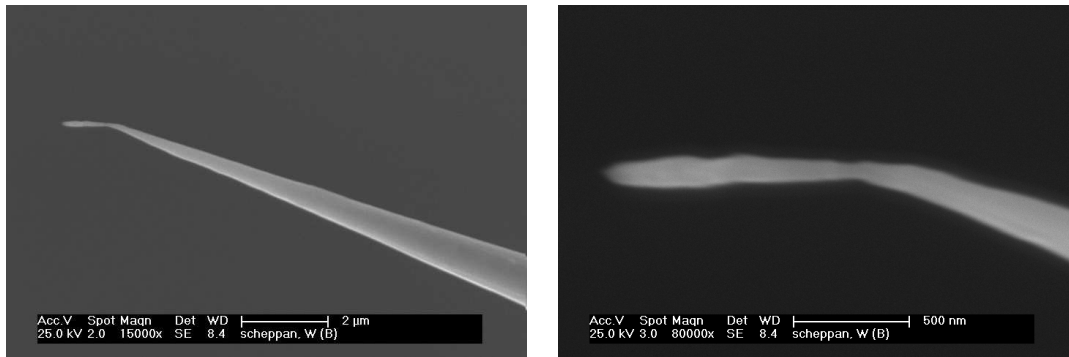
The *cleanliness* of the sputter gas turned out to be more important than the gas pressure. This includes the quality of the supplied gas as well as the amount of residual gas in the recipient before introducing the sputter gas. During sputtering, we occasionally observed sudden breakdowns of the emission current. After such incidents, no more field emission could be measured up to 1 kV, indicating that the tips were blunt. A SEM image of such a tip can be seen in figure 3.19. This blunting could be explained by the occurrence of a discharge between tip and counter electrode due a high concentration of water vapour[34]. The resulting high currents might lead to a melting of the tip. This would be in agreement with our observation that a higher residual gas pressure in the chamber leads to a considerably increased probability of such discharges. In order to reasonably reduce the loss rate, we found that the base pressure in the chamber should be at least three orders of magnitude smaller than the neon pressure. This is a severe problem if the part of the chamber in which sputtering takes place is often exposed to ambient conditions. Furthermore, the lines of the

gas supply ought to be flushed before use.

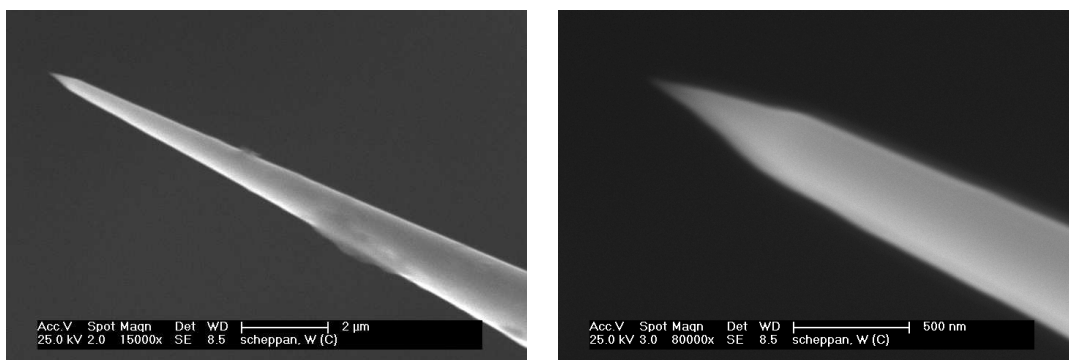
In summary, the method of self sputtering offers an effective means for tip conditioning. An increasing neck-formation close to the apex leads to a decapitation of the tip. If the process is determined immediately after such incident, the remaining tips are sharp and free of contaminants. However, it is profitable to subsequently anneal the tips in order to achieve high quality STM data with a reasonable success rate.



(a) The tip was sputtered for about 30 minutes with $p_{\text{Ne}} = 3 \cdot 10^{-5}$ mbar, $I_{\text{emis}} = 15..18 \mu\text{A}$. The sputter voltage dropped from initially 320 V to < 200 V. The process was terminated manually, no sudden jumps in voltage were observed. A slight neck has evolved about 500 nm away from the apex. The apex radius is (22 ± 3) nm.



(b) Sputtered at $p_{\text{Ne}} = 3 \cdot 10^{-5}$ mbar, $I_{\text{emis}} = 16..18 \mu\text{A}$. The voltage dropped rapidly in the first minutes of the process from < 500 V to 330 V; then it decreased only very slowly without any sudden drops, until the process was stopped manually after 60 minutes. The neck is more pronounced and further away from the tip apex than at 3.16(a); a second slight necking can be seen closer to the apex. The bending of the tip might have happened during sputtering as the tip was horizontally, or *ex situ*.



(c) This tip was sputtered for only less than 8 minutes before the process was terminated automatically by the power supply. Starting at very low currents (the voltage limit of our power supply, 1 kV, was not sufficient to draw more than $2 \mu\text{A}$ from the tip), current later increased to $> 15 \mu\text{A}$. The field emission threshold reduced from 340 V before sputtering to 220 V afterwards, indicating that the tip was sharpened. The tip apex radius determined from the SEM image is (12 ± 3) nm. The change of the cone angle indicates that the tip was decapitated during sputtering, resulting in a mechanically very stable geometry.

Figure 3.16: SEM images of W tips which had been exposed to self sputter treatment with neon ions. The images within one line always show the same tip at different magnifications.

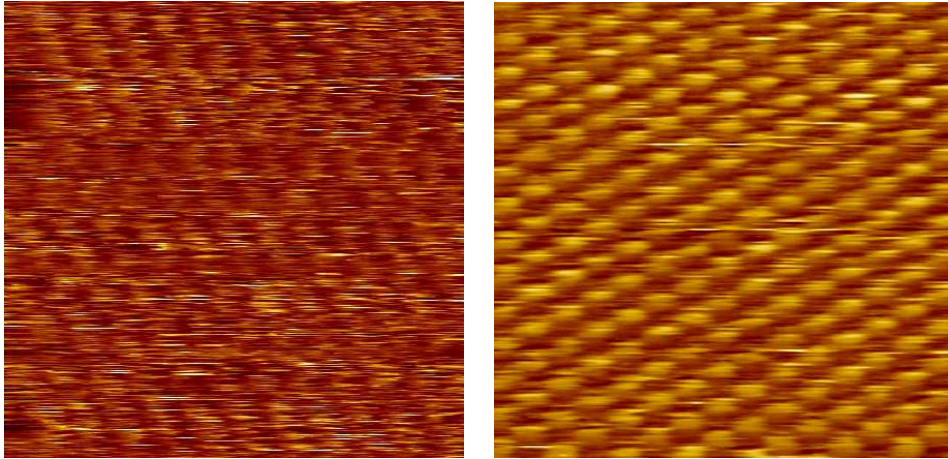


Figure 3.17: Comparison of two $3 \times 3 \text{ nm}^2$ STM topographs obtained with the same W tip on HOPG at room temperature. The left image was recorded with the untreated tip, the right one after self-sputtering at a neon pressure of $2.5 \cdot 10^{-5}$ mbar. The sputter process was stopped automatically after five minutes.

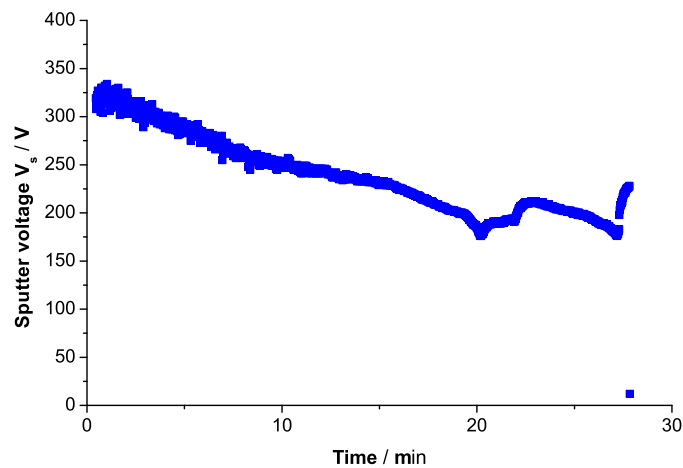


Figure 3.18: A sputter voltage vs. time curve, showing repeatedly an increase in voltage. The process was terminated manually.

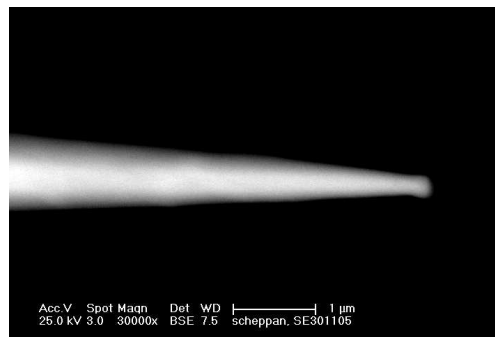


Figure 3.19: This tip was accidentally blunted on a large scale during self-sputtering at too high base pressure in the chamber

3.4.3 The influence of an electric field on the tip

Even though the overall shape of an etched tungsten tip is quite stable, it is subject to permanent changes on an atomic scale. Atoms can diffuse along the surface, be evaporated from the surface, or atoms from the gas phase can be adsorbed on the tip surface. On the one hand, this may lead to undesirable effects during experiments. Changes in the atomic configuration or contaminations migrating towards the very tip apex may disturb data acquisition. Working at low temperatures may reduce such effects since the diffusion depends exponentially upon activation energy (cf. equation (3.9) in section 3.4.1).

On the other hand, the latter effects can be beneficial for tip preparation if applied in a controlled manner. As shown by FINK, it is possible to create mono-atomic tungsten tips using field evaporation[21]. Carefully adjusting the tip potential, one atomic layer after the other could be removed from the surface of a single-crystalline tungsten tip. The process was carried out and monitored in a FIM setup with electric fields in the order of 4 V/Å. This procedure is technically very demanding, though.

At a sharp tip, thermal diffusion creates a flux of atoms which is directed away from the apex. With a strong electric field, the direction can be reversed, though[14]. Under the influence of an external field \mathbf{F} , atoms at the metal surface are polarised[39, 40]. The resulting dipole moment $\tilde{\mathbf{p}}$ is proportional to the field, $\tilde{\mathbf{p}} = \alpha\mathbf{F}$, the constant α being the polarisability. The potential energy of such a polarisation is

$$W = \frac{1}{2}\tilde{\mathbf{p}} \cdot \mathbf{F} = \frac{1}{2}\alpha F^2 \quad (F = |\mathbf{F}|) \quad (3.10)$$

In an inhomogeneous field, as it is present at the apex of a sharp tip, such dipoles experience a force

$$\mathbf{K} = -\nabla W = \alpha F(\nabla F) \quad (3.11)$$

Note that field enters equation (3.11) quadratically. This force is always directed *towards* the highest field. Accordingly, the field induces a diffusion flux towards the tip apex, independently of the polarity. This diffusion can be used to alter the atomic configuration: During tunnelling in an STM, the field strength between tip and sample is large also for moderate gap voltages due to the small tunnelling gap of less than 1 nm. A widely used way of tip treatment *inside the STM* is to strongly increase the voltage for a short time while the tip remains in proximity to the sample. To our experience, this procedure is helpful for tips which are sharp but do not show satisfactory resolution. Applying 5 to 10 V for few seconds was sometimes sufficient to change a tip in a profitable way. It seems to be promising to apply this procedure in connection with other methods, as to "put the finishing touch", or to recover tips which have changed during scanning. A higher voltage in the order of 50 to 80 V may be more effective to improve our tips[41]. However, the pre-amplifiers in use at our STM's are limited to $V_{\text{gap}} = \pm 10$ V. We are, therefore, planning on altering our electronic setup, in order to be able to apply higher voltages.

3.5 Facilities for *in-situ* tip conditioning

Part of the experimental task of this work was the design and construction of facilities for *in-situ* tip conditioning for both our STM systems. The aim was the reliable fabrication of tips yielding high resolution and low noise STM data by choosing one, or a combination of methods described in the previous sections. The entirely different designs of the two STM and, specifically, of the respective tip holders demanded for different solutions for the tip conditioning stages as well. Either design will be described in this section.

In both systems, the stages for tip treatment were mounted in the load lock chambers. The advantage is that one can carry out tip conditioning without opening the main UHV chamber. The loadlock can be evacuated separately with turbo pumps. Within a few minutes, the pressure normally reaches the 10^{-6} mbar range, which is sufficiently low for a first careful field emission test. If the tip is found to be sharp enough, the loadlock can be pumped further until the working pressure for tip conditioning (10^{-8} mbar range) is reached. Otherwise the tip can be replaced by a new one without losing overly much time. The load lock chamber of the VT-STM can be seen in figure 3.21. The design of the chambers is similar for both STM's. In either case, the tip conditioning stage was mounted on a stainless steel angle which was attached to a CF40 port, cf. figure 3.20. The stage can be retracted by a linear drive such that tips or samples can be transferred into the main chamber using a manipulator.

On top of the construction of the stages for tip conditioning, some additional technical requirements were to be provided. A power supply was designed for field emission experiments and self-sputtering of tips. The power supply will be described in section 3.5.3. The gas supplies of the UHV recipients had to be added or adapted, cf. figure A.1 on 80, and modifications had to be made to the loadlock vacuum chambers.

3.5.1 Tip conditioning at the Cryogenic STM

As shown in figure 3.20, there are two places to put tip holders. The dovetail openings were made by electrical discharge machining (EDM) from a piece of stainless steel. At the left place, the tip is situated beneath a looped 0.2 mm diameter tungsten wire. This loop serves as counter electrode for self sputtering and field emission tests, and as both filament and counter electrode for tip annealing by electron bombardment. The loop has a diameter of 2-3 mm, and it is a few millimetres away from the tip end, depending on the tip length. One end of the looped wire is connected to a current feedthrough whereas the other end is at ground. The high voltage is in any case supplied to the *tip*, leaving the counter electrode at ground potential. Otherwise, there might be an undesired flow of electrons between counter electrode and the surrounding UHV chamber or other metal parts in the environment. The second position for tip holders is designed for direct annealing of the tip. A piece of tungsten wire is positioned in such a way that it touches the tip shank 1-2 mm below the tip's apex.

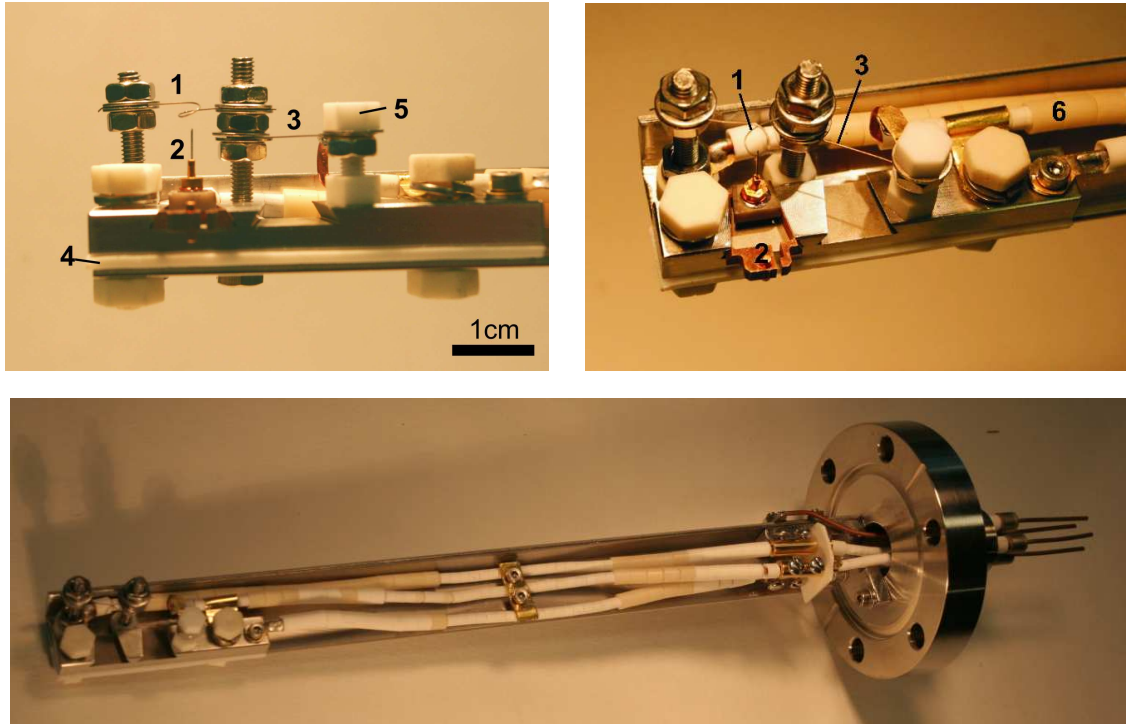


Figure 3.20: Stage for tip conditioning in the Cryogenic STM. (1)-looped W wire as counter electrode/filament, (2)-tip holder with tip pointing upwards, (3)-W filament wire for direct annealing; insulation by Teflon (4), ceramic screws (5) and ceramic beads around electrical connections (6)

When a current of few amperes is passed through the wire, it starts to glow, and heat can flow into the tip. During glowing, tungsten becomes very brittle. In order to not break the filament wire, the tip only touches the filament when the tip holder is fully inserted into the stage.

The high voltages involved demand for a good electrical isolation. At the same time, the materials have to be suitable for application in vacuum. The stainless steel part which contains the tip holders is isolated from ground by a 1 mm teflon layer. Electrically isolated parts were connected using Al_2O_3 screws, nuts and washers[42]. Some of these ceramic parts had to be replaced after some time of operation because they were not insulating any more. Presumably, a thin conducting layer had been deposited from the W filaments onto the ceramic surfaces. The resulting leak currents rendered low-current measurements impossible. The electrical wiring was made from 1 mm copper wire, surrounded by ceramic beads. 1 mm wire was used to account for the high currents flowing, and to avoid wires being bent and causing a short circuit. For connection to external power supplies, a four-way vacuum feedthrough was used (connecting both the filaments, the tip HV and ground).

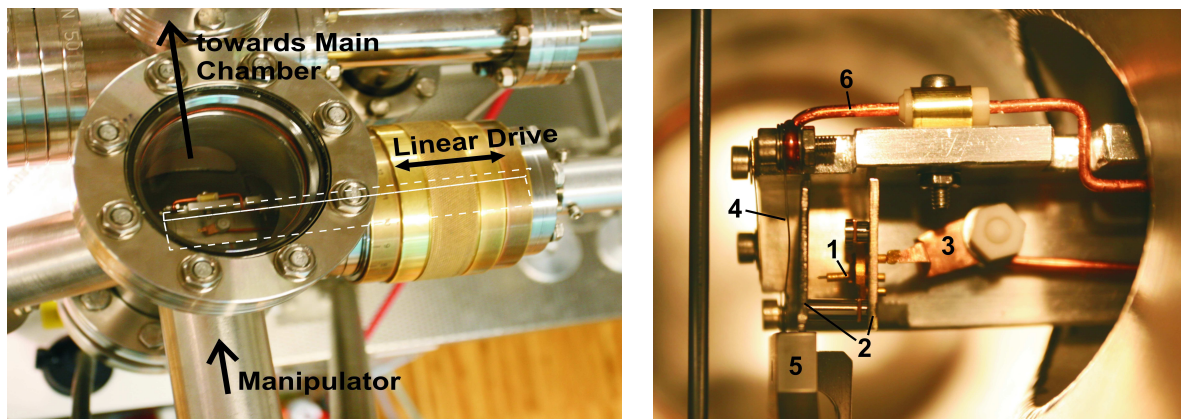


Figure 3.21: Stage for tip conditioning in the VT-STM. (1)-tip holder with the three legs and a tip (pointing left), (2)-two parallel plates of the tip carrier, (3)-contact spring to supply HV to the tip, (4)-W filament wire for direct annealing, (5)-transfer manipulator, (6)-1mm copper wire

3.5.2 Tip conditioning at the VT-STM

For the transfer within the VT-STM, the tip holder is here put into a special carrier, as it can be seen in figure 3.21. It consists of two parallel stainless steel plates which are connected by screws and which have the same dimensions as the sample plates. Tips and samples can so be handled in the same way inside the recipient. The tip itself is electrically isolated from the body of this tip holder. Electrical contact to the tip is established through one of three small legs at the backside of the tip holder. The high voltage necessary for tip conditioning is applied by touching this leg with a contact spring. For this end, the tip carrier is put sideways onto the steel angle which the conditioning stage is mounted on. One of the plates of the carrier (the one on the left in figure 3.21) serves as a counter electrode for field emission and self-sputtering. This is possible because the carrier itself is at ground potential via the steel angle. To facilitate the tip conditioning, the original carrier plates had to be modified. Tip annealing can be performed by touching the tip shank with a glowing W filament wire which is brought between the two plates of the carrier. Annealing by electron bombardment is not possible in this setup. An additional degree of freedom would be necessary to bring a filament close to the tip and at the same time apply high voltage to the tip.

3.5.3 A power supply for field emission and self-sputtering

A new power supply was designed in order to perform field emission tests and self-sputter treatment of tungsten tips. A number of demands had to be taken into consideration. The most important features of the power supply are described in the following. A schematic

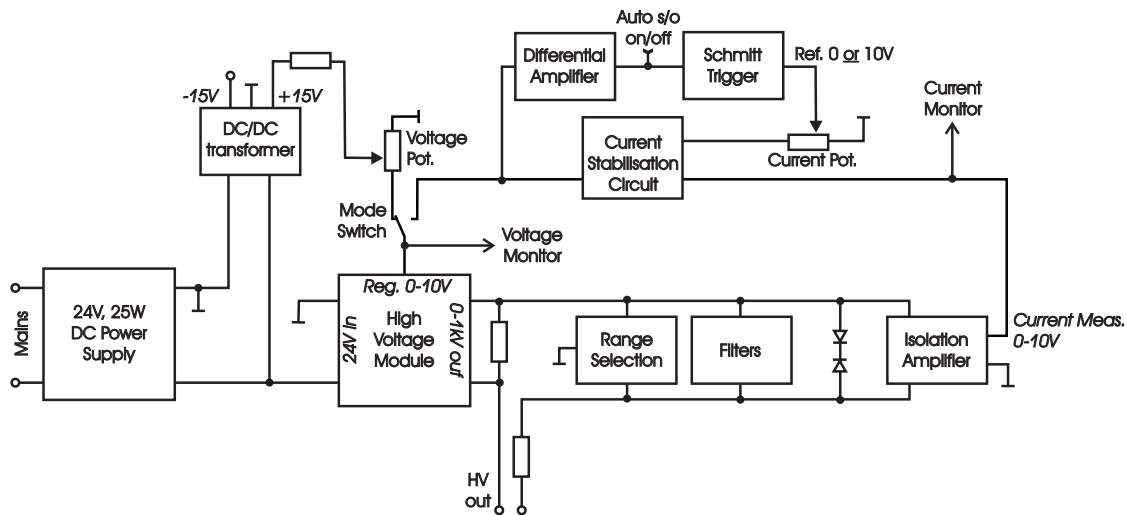


Figure 3.22: Block diagram of the power supply designed for field emission and self-sputtering (FESS). The electronic design is penned by M. RAMS

circuitry is sketched in figure 3.22

The power supply provides negative high voltages up to 1 kV. Four ranges for current measurement are available, the lowest up to 100 nA and the highest up to 100 μ A. Each range covers 3,5 digits, hence the lowest detectable current is 0.1 nA. Current measurement is performed as voltage measurement across resistors in series with the output. The vacuum gap between tip and counter electrode has a resistivity in the G Ω range, and the resistors thus experience only a comparably low voltage drop. However, the resistors have to be well-separated from ground potential. An isolation amplifier (ANALOG DEVICES AD210*¹) enhances the signal and minimises noise. Along with the high voltage, the current measurement signal is displayed on an LCD and can be transmitted to a computer via an USB interface module (MEASUREMENT COMPUTING PMD-1208LS). In this way, both values may be monitored over time either directly or within a home-written computer program.

The mains voltage is transformed into 24 V DC. This voltage is used for regulation purposes, but is also transformed into the required high voltage by a miniature HV module (APPLIED KILOVOLTS MHP1N). The output of the HV module with a maximum voltage of 1 kV is proportional to a regulation voltage (0-10 V). Two different ways can be chosen to set the regulation voltage (and, hence, to control the high voltage): The first one is used for field emission experiments. The regulation voltage is directly tuned with a potentiometer ("voltage pot" in figure 3.22). In this way, one can gradually increase the voltage applied to the tip and read the electron emission current.- The second mode is adapted to self-sputtering. The regulation is facilitated by a feedback loop. The input signal is the measured emission current (more precisely, a voltage proportional to the latter). The current

¹All electronic devices available at CONRAD ELECTRONICS GMBH[43]

stabilisation circuit, containing a differential amplifier, regulates the voltage in such a way that the emission current drawn from the tip during sputtering remains (nearly) constant. A second control loop is responsible for the automatic switch-off of the sputter process in case of a tip decapitation (cf. section 3.4.2). The output of the current stabilisation circuit is fed via a differential amplifier into a so-called SCHMITT trigger. This module sets the regulation voltage to zero in case of a drastic change of its input signal. As a matter of fact, sudden sudden drop of the sputter voltage, as in figure 3.15, can be detected, and the sputter process can be terminated accordingly. This automatic switch-off can be disabled. By means of a potentiometer ("current pot"), the regulation voltage can be tuned. In this way one can determine the current setpoint for which the high voltage is stabilised.

The vacuum gap between tip and counter electrode has a huge electrical resistance. For a typical field emission current of 1 nA at a tip voltage of 500 V, the equivalent ohmic resistance would be 500 G Ω . Hence, one cannot use conventional cable because the leak current through the isolation would quickly exceed the low field emission currents. We therefore used Teflon isolated cable. The cable should also be as short as possible in order to minimise the leak current. In this way, also charging effects due to the capacitance of the cable would be reduced. Another problem connected with the high resistance are leak currents on the circuit board inside the power supply. We noted that on days with high air humidity, the level of parasitic leak current was considerably enhanced. Protecting the sensitive regions with nitro varnish helped temporarily. Over time, however, the varnish absorbed moisture, again causing leak currents. Finally, the problem could be solved by coating the entire board with hot glue.

4 Selected STM Results

In this chapter, some of the STM data obtained during the work for this thesis are presented. For most of the tips which were tested in STM after conditioning, graphite was used. It is comparatively easy to obtain atomic resolution on graphite, which makes it a convenient standard sample to check on the tip quality. Furthermore, the regular and isotropic surface can be used to calibrate the STM in x and y direction. For calibration in z direction, we used the (111) surface of a gold single crystal. Gold was chosen because it does not show oxidation, and the preparation of clean and smooth surfaces costs moderate effort, compared with other metals. Finally, experiments were carried out on niobium diselenide (NbSe_2). Besides an easy surface preparation, this material features interesting effects as type-II superconductivity and the formation of charge density waves.

4.1 Graphite

The most frequently used sample for STM experiments within this work was *highly oriented pyrolytic graphite (HOPG)*. Graphite is thermodynamically the most stable of the two common allotropic forms of carbon (the other one is diamond). The crystal structure is sketched in figure 4.1. By sp^2 orbital hybridisation, each carbon atom is covalently bonded to three

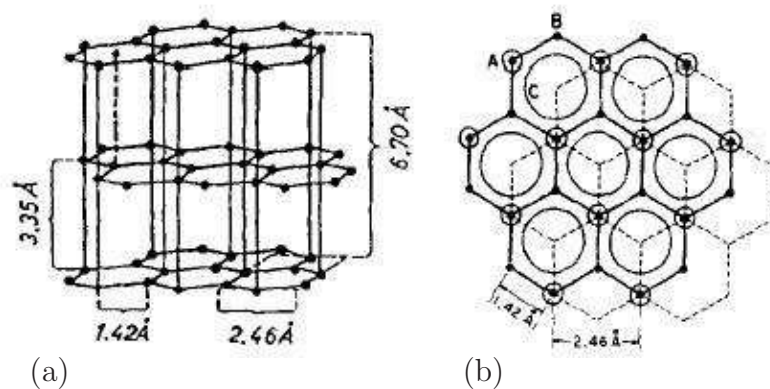


Figure 4.1: Crystal structure of graphite

other carbon atoms. These σ bonds form layers of hexagonally arranged C atoms. The nearest neighbour distance is 1.42Å. The overlap of the $2p_z$ orbitals perpendicular to the planes produces rings of delocalised π electrons, leading to a good electrical conductivity. The graphene layers are weakly bonded to each other by VAN DER WAALS forces, yielding an inter-layer spacing of 3.35Å. Neighbouring layers are shifted relative to each other, resulting in an ABAB stacking sequence. Thereby exist two different types of carbon atoms in each layer(cf. figure 4.1 b)): those which have a direct neighbour in the adjacent layer (denoted as A sites), and those which do not have a direct neighbour in the next layer (B sites)[44]. Figure 4.2 shows atomically resolved STM images of HOPG, recorded at low temperatures. In the inset in figure 4.2(a), the honeycomb structure of the C atoms of the two topmost layers is illustrated. A contrast between A and B sites is clearly visible. The site asymmetry does not result from real height inhomogeneities due to displacement of the atoms, rather the contrast reflects differences in the electronic properties of the respective atom sites. According to band theory, the amplitude of the BLOCH wave at an A site is smaller than at a B site[45]. At an A site, the LDOS is reduced around the FERMI level because of the bonding and antibonding interaction between the π orbitals of the topmost layer and the underlayer. Hence, the tunnelling current is higher at a B site than at an A site. The tunnelling probability is lowest in the centre of the C hexagons. Here, the BLOCH wave has a cross point of nodes, and the axial symmetric orbitals of the tip do not contribute to the tunnelling current. Note that images recorded with an asymmetric tip may differ from this situation ("abnormal imaging"[45]).

Naturally occurring graphite single crystals are relatively small and difficult to obtain. An alternative is HOPG, a polycrystalline material with large grain size and good orientation along the layer stacking axis. HOPG cleaves easily due to its layered structure. Just by peeling off the topmost layers by means of adhesive tape exposes large clean and atomically flat areas (cf. figure 4.2(b)) which are suitable for STM. In addition, a so-prepared surface is inert to oxidation. Because of the straightforward surface preparation, the high symmetry and the well-known lattice parameters, we used HOPG samples for calibrating our STM scanners in x and y direction. HOPG is not ideally suitable for calibration in z direction, though. Due to the weak coupling between the graphene layers, interactions between tip and sample may alter the interlayer spacing at the surface (i.e. slightly lift the topmost layer). In particular, it is not easily possible to measure the height of monoatomic steps.

On top of atomic corrugations, the STM image in figure 4.3 shows a pronounced superstructure which has the same hexagonal symmetry as the atomic lattice. It also reflects the site asymmetry of the atomic corrugations. Such patterns have repeatedly been reported for graphite with a wide range of superlattice periodicities (Ref. [46] and references therein). ALBRECHT et al. found the superstructure close to the boundaries of regions with differently oriented atomic lattices[47]. KUWABARA et al. suggested that the superstructures were rotational MOIRÉ patterns caused by a slight misorientation of the topmost graphene

layer by an angle θ with respect to the underlying substrate. To illustrate this phenomenon, figure 4.3 shows two identical triangular lattices of dots which are tilted by different angles θ with respect to each other. The resulting interference pattern again has threefold rotational symmetry. Its periodicity a_s and the tilting angle φ between the superstructure and original lattices changes with θ . a_s and φ can be expressed as[48, 46]

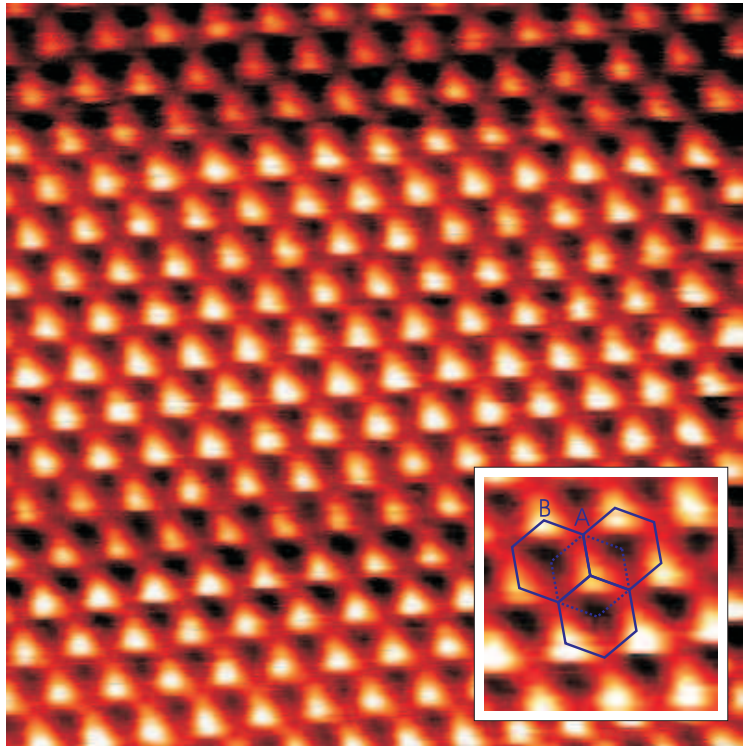
$$a_s = a/[2 \sin(\theta/2)] \quad (4.1)$$

$$\varphi = 30^\circ - \theta/2 \quad (4.2)$$

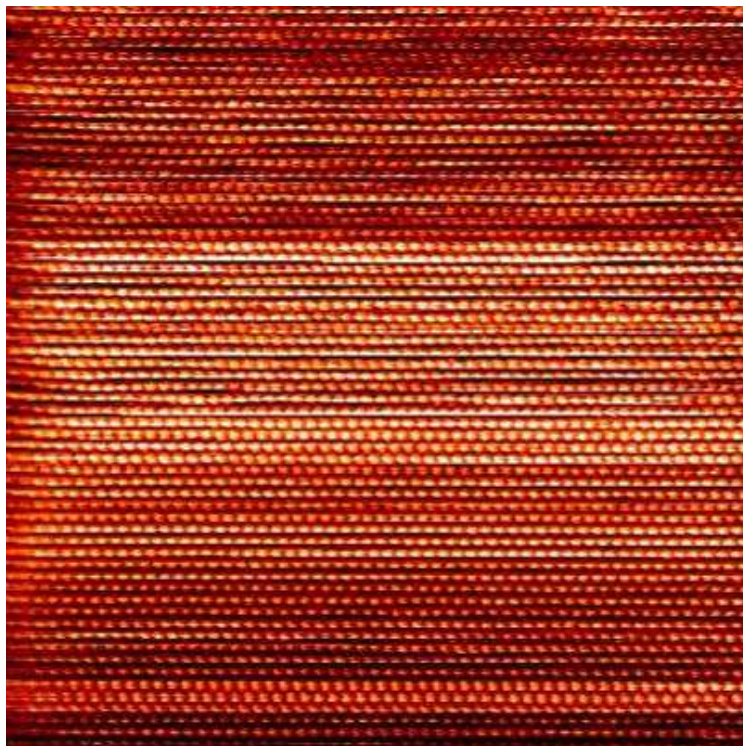
where a is the spacing of the atomic lattice. The superlattice in figure 4.3¹ has a periodicity of $a_s = (21 \pm 1)\text{\AA}$, and it is tilted by $\varphi = (27 \pm 1)^\circ$ against the atomic lattice. Inserting these values into equations (4.1) and (4.2) yields for θ $(6.7 \pm 0.1)^\circ$ and $(6 \pm 2)^\circ$, respectively. Here, the next-nearest neighbour distance for graphite $a = 2.46\text{\AA}$ was used. It should be pointed out that the modulation of the tunnelling current in the superlattice does not correspond to any topographic features. According to RONG and KUIPER[46], rotating the topmost layer with respect to the underlayers would alter the stacking sequence periodically along the surface, resulting in BAB, AAB, CAB and intermediate type sites. Even though the interlayer distances for those stacking sequences are all virtually the same, the contrast in tunnelling current can be explained by differences in the electronic structure between the different types of sites.

Electronically, graphite is a semi-metal or zero-gap semiconductor. For an isolated graphene layer, the occupied π band and the unoccupied π^* band meet at the corner points of the hexagonal BRILLOUIN zone, obeying a quasi-linear dispersion[50]. The layer interaction of graphite lifts the degeneracy of the π bands[51, 52]. Figure 4.4 shows a differential conductance curve of HOPG, recorded at room temperature. The data are in reasonable agreement with the calculated total DOS of graphite (from Ref. [49]). Note that the total DOS at E_F is non-zero[51], explaining the metallic character of graphite. Deviations from the calculated curve might result either from smearing due to the numerical evaluation of the derivative, or they may originate from thermal drift during measurement.

¹meant is the *triangular* lattice which is made up by the brightest spots

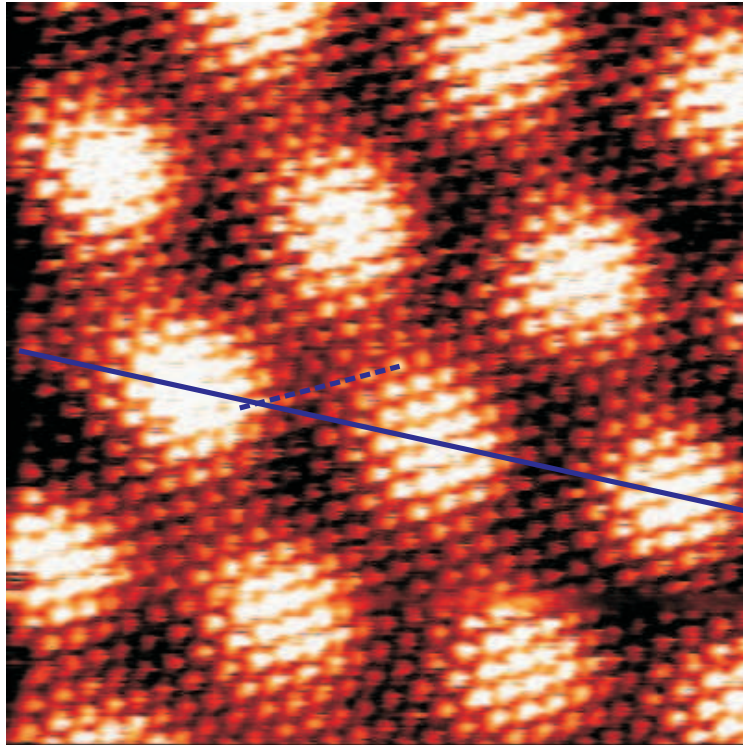


(a) HOPG, $3.2 \times 3.2 \text{ nm}^2$, $V_{\text{gap}} = -0.2 \text{ V}$, $I_{\text{set}} = 0.5 \text{ nA}$, $T = 380 \text{ mK}$. The zoom inset illustrates the hexagonal structures of C atoms.

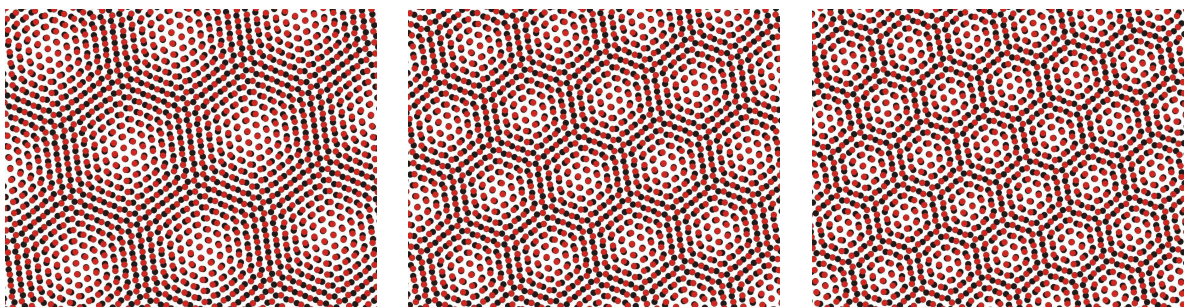


(b) HOPG, $13.5 \times 13.5 \text{ nm}^2$; $V_{\text{gap}} = -0.2 \text{ V}$, $I_{\text{set}} = 0.28 \text{ nA}$, $T = 1 \text{ K}$

Figure 4.2: Atomically resolved STM images of HOPG



(a) $6 \times 6 \text{ nm}^2$ STM image of HOPG ($V_{\text{gap}} = -0.32 \text{ V}$, $I_{\text{set}} = 0.3 \text{ nA}$, $T = 350 \text{ mK}$), showing a rotational MOIRÉ pattern. The lines depict the tilting angle φ between atomic lattice (*dashed*) and superlattice (*solid*)



(b) $\theta = 5.0^\circ$

(c) $\theta = 7.5^\circ$

(d) $\theta = 10.0^\circ$

Figure 4.3: MOIRÉ patterns on HOPG. (a) - STM image; (b) to (d) - simulation with two triangular lattices with the same spacing (red and black dots), which are rotated by an angle θ relative to each other

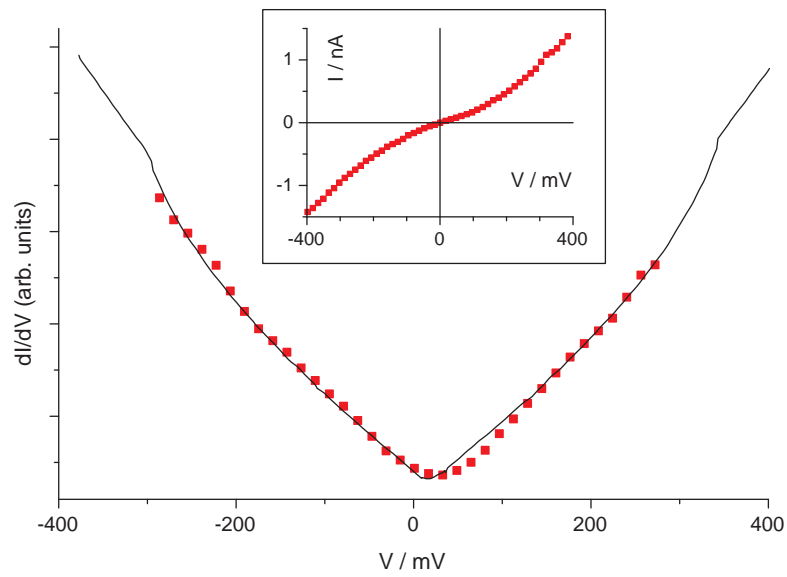


Figure 4.4: Differential conductance dI/dV vs. V of HOPG with a W tip at room temperature. The curve was obtained by numerical differentiation of the $I - V$ curve shown in the inset. The black line is the calculated total DOS of graphite (Ref. [49])

4.2 Au(111) surface

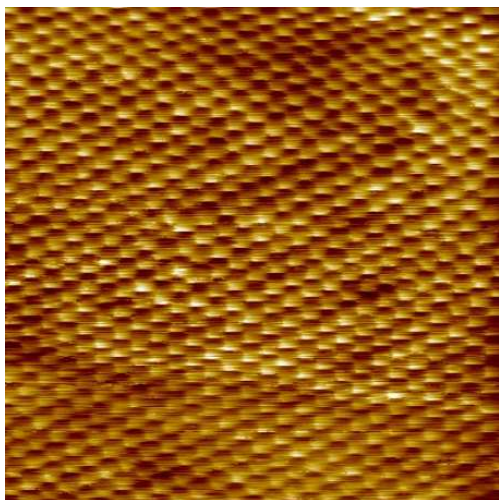
A number of measurements were performed on the (111) surface of a gold single crystal[53]. The initial surface preparation consisted of repeated cycles of Ar ion sputtering and annealing to $\sim 800^\circ\text{C}$. For subsequent experiments, only heating was required if the sample had been stored in UHV. As a result, atomically flat terraces could be found on the surface.

Figure 4.5(a) shows an atomically resolved STM image recorded with a W tip on Au(111) at 350 mK. The arrangement of the atomic sites reflects the threefold rotational symmetry of the (111) plane of the fcc crystal. Atoms at a crystal surface experience a binding environment which differs from that in the bulk. As a result, the bulk atomic positions might no longer correspond to the lowest energy state. In order to minimise the free energy, surface atoms are driven into new locations. In the simplest case the equilibrium is reached by small displacements such as relaxations. In many materials, however, the surface structure differs substantially from the bulk. This effect is called *reconstruction*[7, 36]. Au is the only metal which shows a reconstruction of the (111) surface[55]. This so-called $(22 \times \sqrt{3})$ reconstruction is visible as a pronounced superstructure in figures 4.5(b), (e), and (f))[55, 56, 57]. In order to compensate for the smaller number of nearest neighbours at the surface (nine instead of twelve in the bulk for an fcc lattice), the nearest neighbour distances in the topmost Au layer are *uniaxially* compressed. In the energetically most favourable state, 23 surface atoms are packed on 22 bulk lattice sites along the compression axis. Due to this mismatch, a number of Au atoms are forced from fcc sites to hcp type sites and to incommensurate bridge sites, as it is depicted in figure 4.6. The term $(22 \times \sqrt{3})$ reconstruction refers to the size of the reconstructed surface unit cell. Atoms occupying bridge sites between fcc and hcp stacking regions are slightly displaced in z direction, which causes the brighter stripes in STM images[56]. Such transition regions are called soliton walls. Figures 4.5(c) and (d) show z profile plots along the compression axis. In plot (c), the individual atomic positions are visible. Counting the atomic corrugations along the profile, one finds a periodicity of the reconstruction of 27 atoms. A reason for the deviation from the expected 23 atom-periodicity might be that the observed reconstruction was distorted due to surface defects. This is in agreement with the fact that we found different superlattice periodicities within different sample areas. The magnitude of the corrugations is 0.8-1.0 Å. The profile in figure 4.5(d) extends over three reconstruction stripes. Note that the regions of hcp and fcc stacking do not have the same width, suggesting that the energy of either sites is slightly different[54].

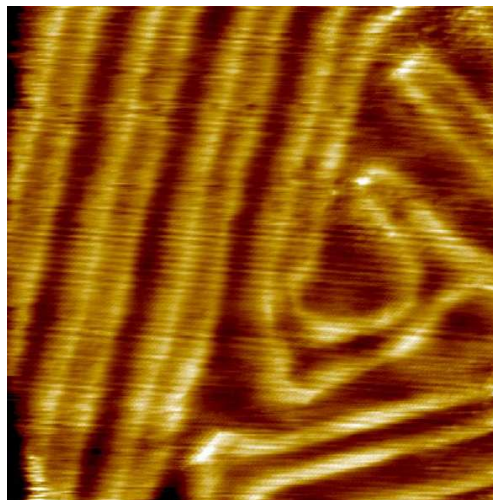
In order to reduce the uniaxial surface stress, the spontaneous formation of domains with differently oriented corrugations can be observed. A domain boundary region can be seen in figure 4.5(b). The threefold symmetry of the underlying fcc(111) face is visible. Note also that the solitons form closed structures. The observed deviation from the $(22 \times \sqrt{3})$ reconstruction might also be due to such domain boundaries. On larger scales, the formation of zigzag patterns is typical, cf. figure 4.7. This is called "herringbone" pattern. The brighter

structures in this image result from remainders of contaminants. The darker area indicates a monoatomic step dividing flat terraces. We used such steps for the z calibration of the STM piezo drives. The scan profile across the step shown in figure 4.7 indicates a step height of (2.55 ± 0.10) Å, which agrees well with the theoretical value of 2.50 Å.

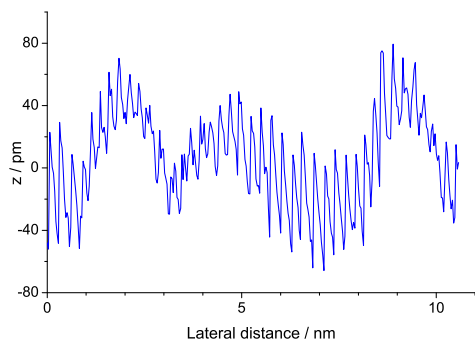
Figure 4.8 shows two images of a gold film which was deposited on a glass substrate by electron beam evaporation. The surface is much rougher than the single crystal surface. High resolution images could not be obtained.



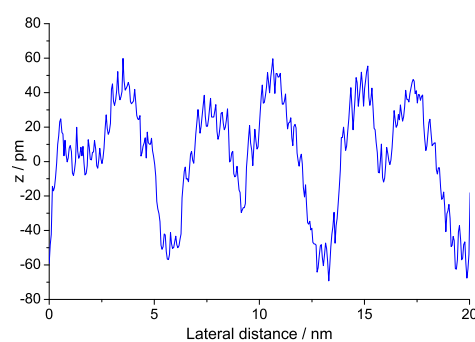
(a) $6.5 \times 6.5 \text{ nm}^2$; the triangular lattice refers to the (111) plane of an fcc crystal.



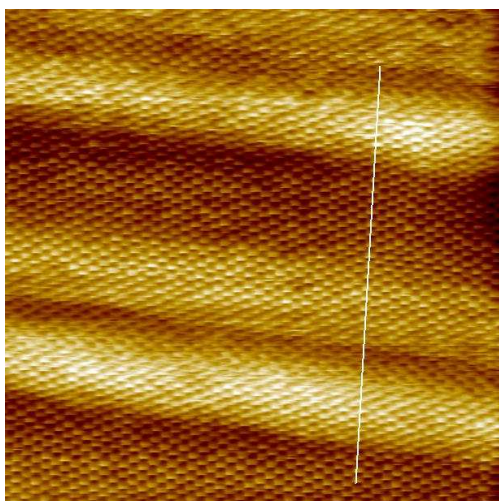
(b) $37 \times 37 \text{ nm}^2$ large scale image, showing patterns of the surface reconstruction.



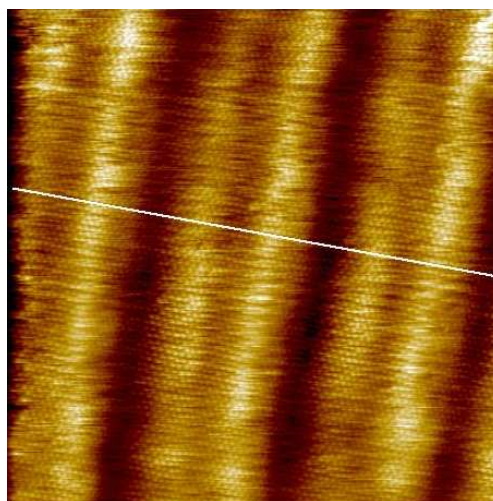
(c) Line profile along the compression axis of the reconstruction in figure (e). The atomic corrugations are clearly visible



(d) Line profile across several reconstruction stripes in figure (f), showing the magnitude of the displacement



(e) $12.5 \times 12.5 \text{ nm}^2$. The height profile along the line is shown in figure (c).



(f) $20 \times 20 \text{ nm}^2$. The height profile along the line is shown in figure (d).

Figure 4.5: STM images of the Au(111) surface, showing atomic resolution and surface reconstruction. $V_{\text{gap}} = -0.32 \text{ V}$, $I_{\text{set}} = 0.74 \text{ nA}$, $T = 350 \text{ mK}$.

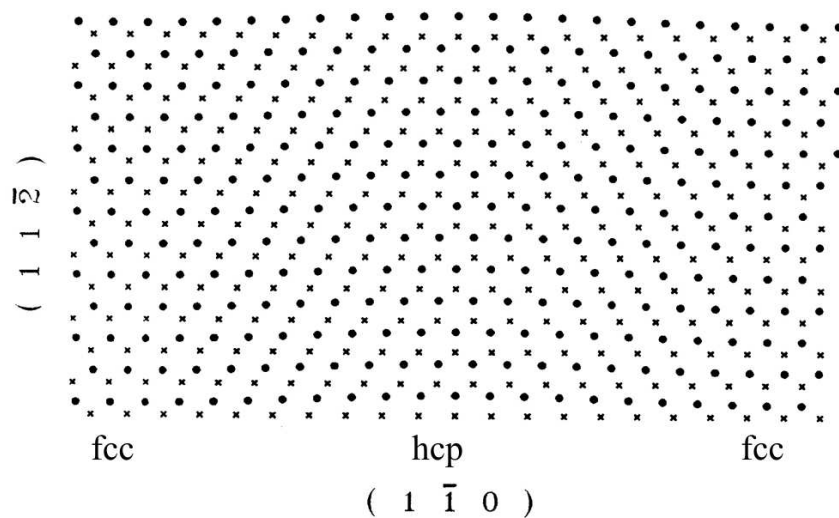


Figure 4.6: Model of the reconstructed Au(111) surface. The crosses denote the positions in the unreconstructed second-layer atoms, the filled circles denote the positions of atoms in the reconstructed top layer. Image faken from [54]

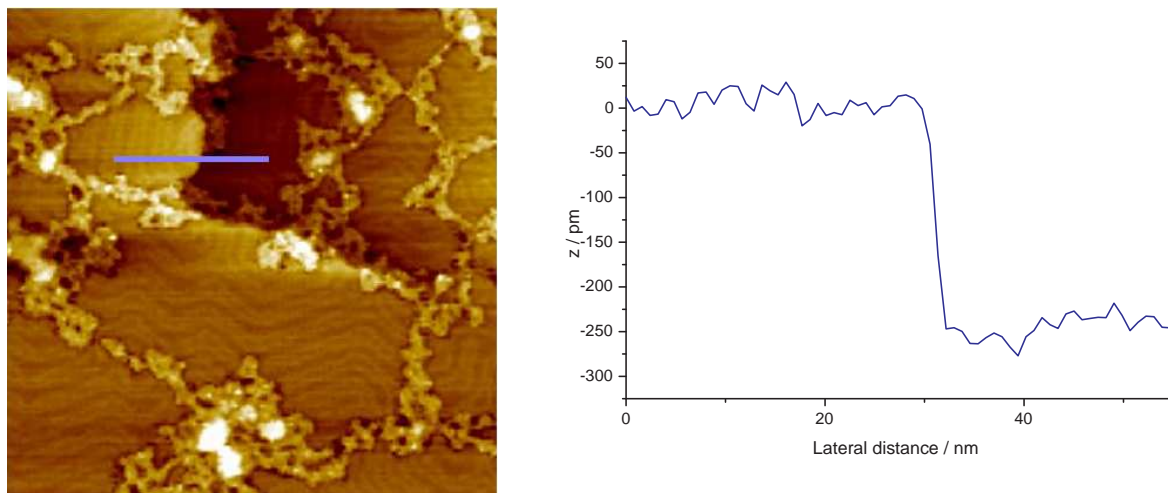


Figure 4.7: Left: $160 \times 160 \text{ nm}^2$ room temperature image of Au(111), showing the "heringbone" zigzag pattern as well as a monoatomic step. Remainders of contaminants are visible. Right: Line profile across the monoatomic step. The step height is 2.6 \AA

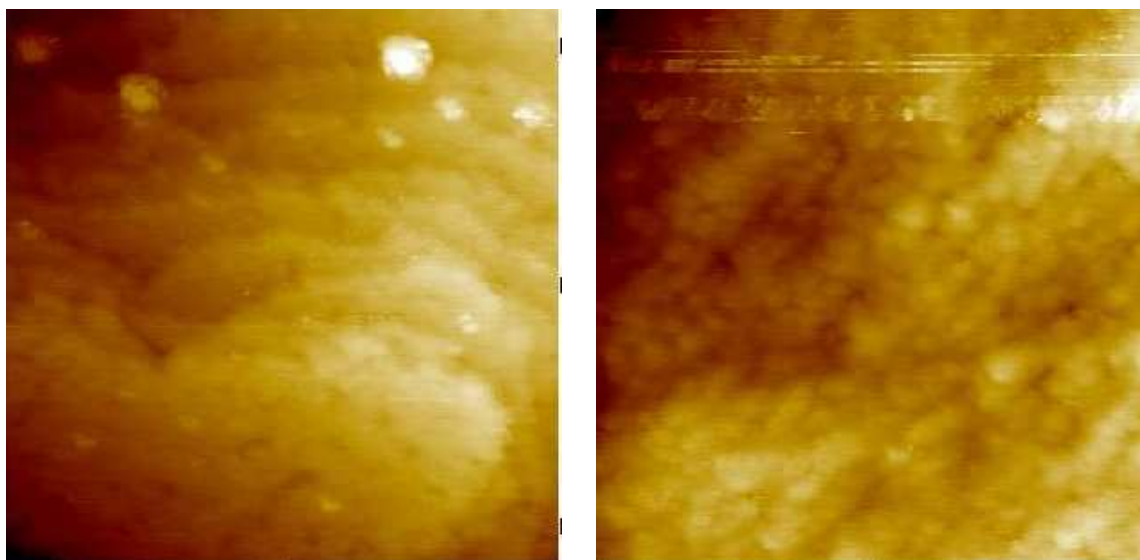


Figure 4.8: $100 \times 100 \text{ nm}^2$ images of a Au film on glass substrate; total z range $\approx 3 \text{ nm}$

4.3 NbSe₂

NbSe₂ is a layered material. Its single crystals can easily be cleaved to expose an atomically flat surface which does not show oxidation. Figure 4.9 shows an atomically resolved STM image recorded at 385 mK. The quasi two-dimensional system NbSe₂ undergoes a charge density wave (CDW) transition at $T_P = 33$ K. In certain materials, a periodic modulation of *both* the ionic lattice and the electron gas leads to a slight reduction of the electron kinetic energy. The effect becomes increasingly important at lower temperatures. Below a critical PEIERLS temperature T_P , the energy gain overcomes the cost of COULOMB energy for distorting the lattice, and a CDW is established. In figure 4.9, this CDW is visible as every third row of atoms appears brighter[16, 58].

NbSe₂ is a so-called *type-II superconductor* with a critical temperature of $T_c = 7.2$ K. Besides a zero electrical resistivity, the superconducting state is characterised by a particular behaviour in an external magnetic field. In a *type-I superconductor*, any magnetic field, which is below a temperature-dependant critical field $H_c(T)$, is completely pushed out of the superconductor. This so-called MEISSNER effect occurs below T_c . In contrast to that, type-II superconductors completely screen magnetic fields only up to a lower critical field H_{c1} . Above H_{c1} , magnetic flux partially enters the superconductor, such that there is a *mixed state* with a coexistence of superconducting and normal conducting regions. At increasing

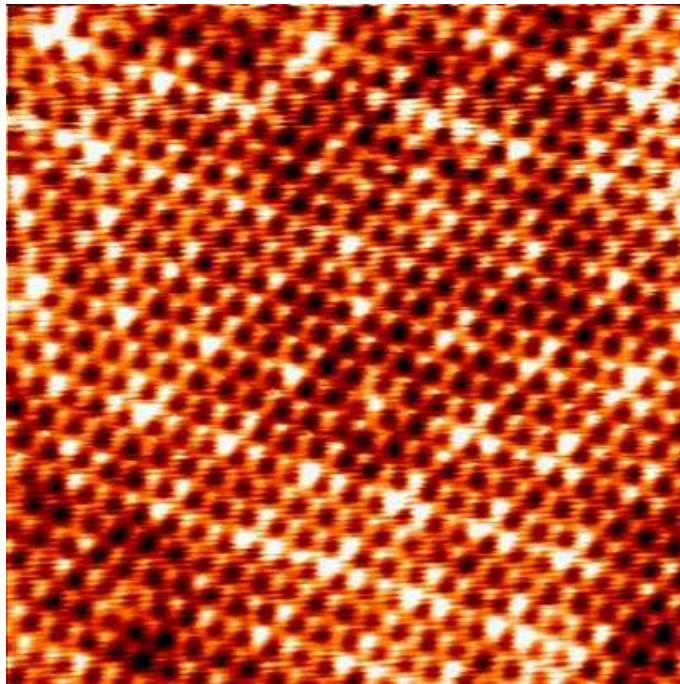


Figure 4.9: NbSe₂, 8×8 nm², $V_{\text{gap}} = 0.1$ V, $I_{\text{set}} = 1$ nA, $T = 385$ mK. The periodic modulation of the atomic lattice is a charge density wave (CDW)

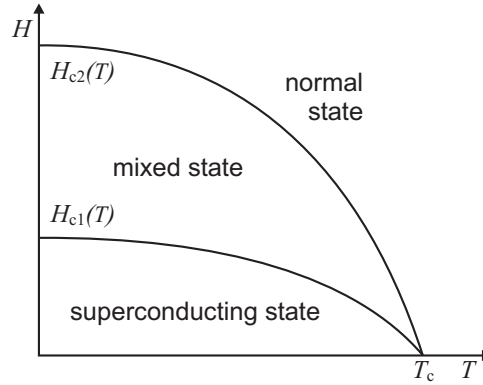


Figure 4.10: Temperature dependence of the critical fields for a type-II SC

field, the superconducting regions shrink until they vanish at the upper critical field H_{c2} . The temperature dependence of the critical fields is sketched in figure 4.10. At $T = T_c$, either critical field is zero.

Tunnelling spectroscopy curves of NbSe₂ in the mixed state are presented in Figure 4.11. The spectra were recorded at $T = 385$ mK in a field $\mu_0 H = 0.6$ T perpendicular to the surface. Figure 4.11(a) shows an I vs. V curve as well as the corresponding dI/dV vs. V curve for a superconducting region. The superconducting gap at the FERMI energy is visible. Within BCS theory (named after J. BARDEEN, L. N. COOPER and J. R. SCHRIEFFER, Ref. [59]), the electron excitation spectrum is given by

$$\rho(\varepsilon) = \text{Re} [|\varepsilon|/(\varepsilon^2 - \Delta^2)^{1/2}], \quad (4.3)$$

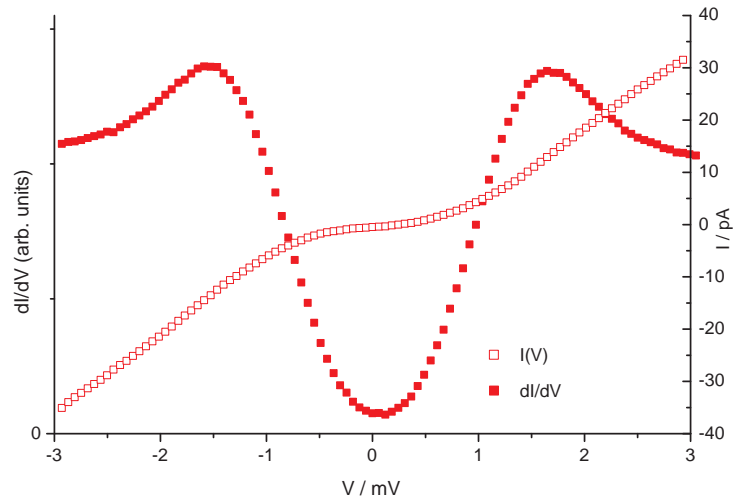
where Δ is the superconducting gap. The broadening of the tunnelling spectrum in figure 4.11(a) can be described by adding a *pair-breaking parameter* Γ [60, 61]:

$$\rho(\varepsilon, \Gamma) = \text{Re} \frac{|\varepsilon - i\Gamma|}{[(\varepsilon - i\Gamma)^2 - \Delta^2]^{1/2}}, \quad (4.4)$$

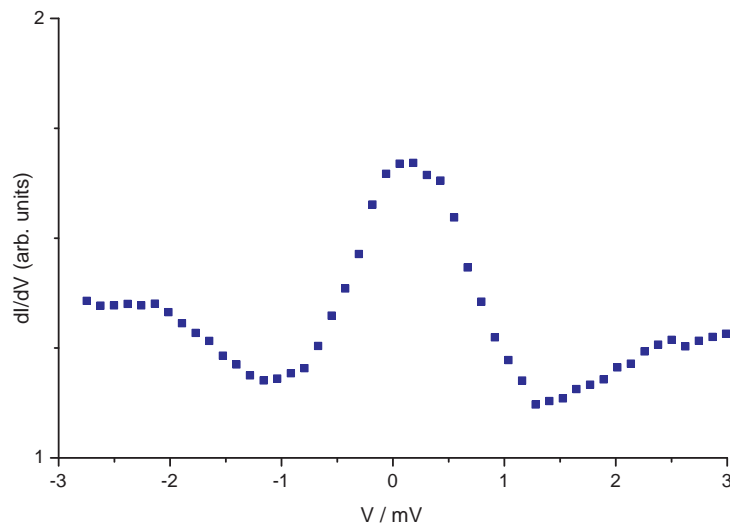
where Γ accounts for a finite life-time of the superconducting quasiparticles due to inelastic scattering.

In the mixed state of a type-II superconductor, the magnetic field can penetrate into normal conducting regions which are surrounded by superconducting currents. Each of these *vortices* carries a magnetic flux of $\Phi_0 = hc/2e$. The spectrum shown in figure 4.11(b) was measured at a surface region which was inside a vortex. No superconducting gap is present. The enhanced DOS at zero bias is related to low-energy quasiparticle states in the vortex [11, 61]. As predicted by A. A. ABRIKOSOV, the vortices arrange periodically in order to minimise the enthalpy of the system [62, 63]. As already mentioned in section 2.2, this vortex lattice can be observed by means of STS. One way to visualise the lattice is current imaging tunnelling spectroscopy (CITS). That is, spectroscopic data is displayed for one and the same bias on a grid of (x, y) coordinates. This is shown in figure 4.12 for NbSe₂.

The image shows dI/dV at $V = 61 \mu\text{V}$ at $T = 385 \text{ mK}$ and $\mu_0 H = 0.6 \text{ T}$. The brighter spots result from the enhanced DOS at E_F in the vortices as compared to the superconducting region. The triangular arrangement of the vortices corresponds to literature results[11]. In order to proof that the bright spots are indeed caused by the vortices, figure shows the dI/dV curves for different positions, as indicated by the arrow in figure. Going from the vortex centre towards the SC region, the peak at zero bias is gradually decreasing, and a gap is opening, whereas the DOS at the gap edge increases accordingly. The measured average spacing of two vortices a_v is $67 \pm 5 \text{ nm}$. This is in reasonable agreement with the theoretical value of $a_v = 48.9 \text{ nm} / \sqrt{B[\text{T}]} = 63.1 \text{ nm}$ [11, 64].



(a) SC region: $I(V)$ (open symbols) and dI/dV (filled symbols), showing the SC gap ($\Delta = (1.5 \pm 0.3) \text{ meV}$).



(b) Vortex: dI/dV , showing an enhanced DOS at E_F .

Figure 4.11: Tunnelling spectra of NbSe₂ at $T = 385 \text{ mK}$, $\mu_0 H = 0.6 \text{ T}$

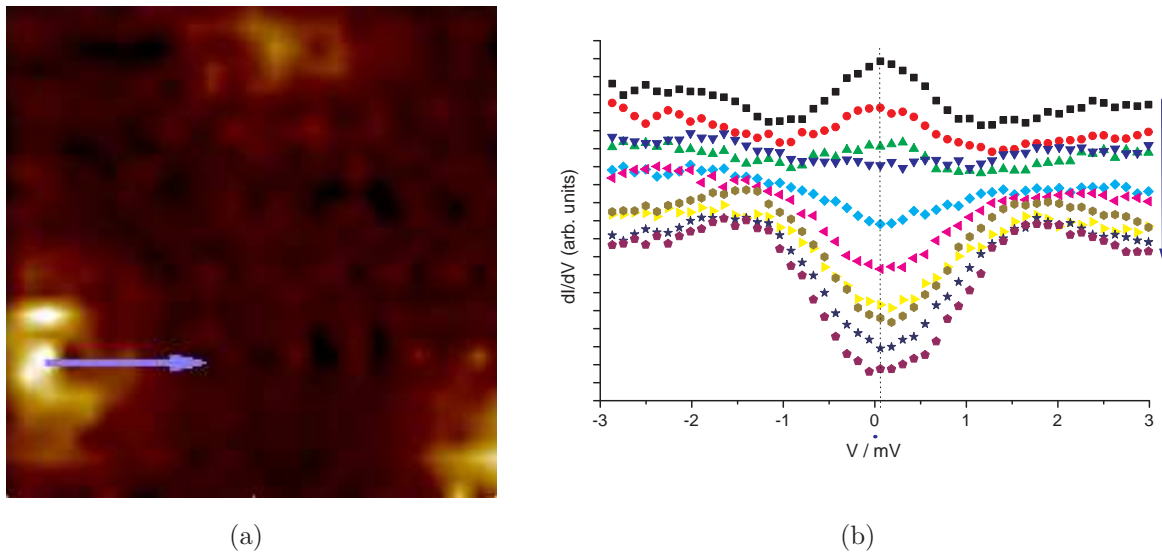


Figure 4.12: (a) $80 \times 80 \text{ nm}^2$ CITS image of NbSe_2 at $T = 385 \text{ mK}$, $\mu_0 H = 0.5 \text{ T}$, showing dI/dV at $V = 61 \mu\text{V}$. The brighter spots originate from the enhanced DOS at E_F in a vortex, and thereby visualise the ABRIKOSOV lattice of the vortices. The arrow indicates where the sequence of spectra in (b) were recorded. Starting in a vortex (top), the zero-bias peak disappears and the superconducting gap opens towards the superconducting region. For clarity, there is an offset of one unit between each two curves. The dashed line marks the bias $V = 61 \mu\text{V}$ used (a)

5 Summary

The present work deals with the preparation and characterisation of tungsten STM tips as well as their use in tunnelling experiments. The aim is the reliable manufacture of tips which perform strongly in STM. Here, the *in-situ* conditioning of the electrochemically etched tips takes the centre stage.

Facilities for the conditioning and characterisation of W tips have been implemented into existing UHV STM systems. This included the design and construction of the stages themselves as well as providing the technical requirements, such as gas supplies, electric and electronic equipment, and adequate vacuum conditions. With these technical prerequisites, it was possible to treat W tips in different ways: annealing by mechanical contact with a filament and by electron bombardement, and self-sputtering with noble gas ions. The efficiency of the available methods was investigated in experiments with more than 70 tips. This does not yet yield sufficiently high statistics to draw irrefutable conclusions about the ultimate way to prepare tips. However, the results give strong hints as which techniques are promising to yield good results, and which are appropriate parameters. The main factor which limits the available amount of data is that the experiments themselves are partially very time consuming. Only to reach appropriate vacuum conditions takes a lot of time, and for STM experiments, a lot of patience is inevitable.

In order to determine the quality of the tips and to judge the efficiency of the conditioning methods, the tips were characterised by means of SEM, field emission and STM experiments. In numerous cases, the results of the respective methods could be compared and related to each other. SEM measurements yielded information about the tip shape on a microscopic scale. In this way, strong contaminations and defects as well as changes to the tip shape caused by any treatment could be directly visualised. Features on an atomic scale could not be resolved, though. If more detailed information were needed in future, other experimental techniques such as TEM would be required. Field emission is a quick and effective means to check on the tip sharpness. The main advantage is that the experiments can be carried out *in situ*, without removing the tip from the conditioning stage. This makes it particularly useful to monitor changes to the tip due to some treatment (see, for instance, figure 3.13). It was proved that the emission indeed occurs from the tip apex, and that the emission current obeys the FOWLER-NORDHEIM equation. Tip apex radii were extracted from FOWLER-

NORDHEIM plots, and the results were in agreement with SEM measurements. Measuring the threshold voltage required to draw a fixed emission current from the tip was found to yield a reasonably good estimate of tip sharpness. As a rule of thumb, it was found that the tip radius in Å is roughly $\frac{2}{3}$ of the measured threshold in volts. More experiments would be necessary to obtain a more exact quantisation. It is doubtful, though, if this would be profitable for the process of preparing STM tips. It seems that tip sharpness is not the ultimate criterion for a good tip. In this work, the probability of obtaining good STM results was highest for tips which, according to field emission, had radii of apex curvature of about 10 to 15 nm. Apparently, more important than achieving the ultimate sharpness is it to have tips which are mechanically stable and free of contaminants.

Strong fluctuations of the emission current might be related to the presence of contaminants on the tip surface. This would be consistent with the fact that gentle annealing frequently stabilised the emission current. Furthermore, tips which had been decapitated during sputtering and can therefore be expected to be free of contaminants, in general showed very stable field emission after the sputter treatment

In this work, tips were annealed in two different ways: For direct annealing, the tip shank was brought into contact with a glowing filament wire. If carried out carefully for few minutes, this procedure was found to be profitable as a first step of conditioning, to remove water and other volatile contaminants. The major disadvantage is that this method is hardly controllable. Tips can easily be blunted due to overheating. Better to control is annealing by bombardment with thermionically emitted electrons. It was found that tips are already affected by fairly low annealing powers because the tips are heated up very locally at the apex. Increasing the power, the sharpness (as measured by field emission) decreases linearly due to a dissolution of W and WO_3 , until a minimum is reached. Heating even stronger, the tip starts to be gradually blunted. The position of the minimum of sharpness could so far not be related to properties of the tip. For effective annealing without risking to blunt the tips, powers of 20 to 100 μW seem to be promising. The success rate in STM of the tips which had been exclusively treated by electron annealing was rather low (about one third). The method might be more effective after further optimising the parameters. So far, most experiments were carried out at voltages of 250 to 500 V. It therefore might be worthwhile studying the effect of considerably higher voltages, especially since high electric fields influence the surface diffusion.

More than 30 tips which had been exposed to sputter treatment were tested in STM. Comparison with SEM data revealed that self sputtering leads to the formation of a head-and-neck structure (cf. figure 3.16), and eventually to a decapitation of the tip. The latter is connected to a sudden drop of the sputter voltage. Determining the sputter process automatically after such decapitation, the success rate in STM of the resulting tips was about 60%. Subsequent annealing of the tips further improved this rate. Throughout this work, self sputtering could only be combined with direct annealing, as described above. It

may be worth use electron beam annealing instead. Tips for which no decapitation was detected generally did not show satisfactory STM results. Crucial for successful sputtering is sufficiently high vacuum (10^{-8} mbar range for a neon pressure of 2 to $4 \cdot 10^{-5}$ mbar). Otherwise, the probability to harm the tip by electrical discharges is too high.

In conclusion, the technical prerequisites for tip conditioning have been established, and the available methods have been tested. Applying one, or a combination of the techniques, good tips could be prepared with a certain success rate. The quality of the tips was tested on HOPG, Au(111) and NbSe₂ samples, achieving high resolution in topography and spectroscopy. A "recipe" for tip preparation is given in this work. Even though it is specified for our setups, it may be applicable to other UHV-STM's, or even to other measurement techniques which require sharp and clean probes, such as AFM. It shall be noted that this is not yet the ultimate way to prepare tips. It is rather a basis on which the success rate can certainly be further improved. Especially, the combination of the above methods with tip sharpening under the influence of a high electric field, as described in section 3.4.3 seems to be very promising.

Appendix: A recipe for tip preparation

In the following, a guideline for tip preparation will be given. The procedures are adapted to the experimental equipment which was available for the present work. Note that this recipe is not yet claimed to be the ultimate way, further optimisation of certain parameters may be possible.

Etching (cf. section 3.2)

- Cut pieces of appropriate length from 0.375 mm diameter 5N tungsten wire (VT-STM 6.5-7 mm, Cryogenic STM 10-11 mm). The pliers should be used for this purpose only. It is profitable to have at least 20 pieces ready.
- Prepare 20 ml of 3M NaOH solution (7.5 ml 32%NaOH solution and 12.5 ml de-ionised (DI) water), and pour the required quantity into the tip etching stage. During the whole etching process one should wear gloves to protect the hands from the etchant and to keep the tips clean.
- Pre-etch the W pieces in order to create a clean and smooth end. For this end, insert the pieces by 2-3 mm into into the solution, and etch them for about one minute, such that the W surface becomes shiny and all fibres (originating from the grooves in the initial wire surface) have come off, but no considerable neck formation is visible yet. The right point to stop can be seen by observing the etching current: As long as W fibres stick to the wire, the current fluctuates by several mA. Stop the process when the current has stabilised and starts to drop gradually. This procedure should be done at once for all the cut pieces before starting to etch tips. (This is rather tedious work, but it is worth it...)
- Fill fresh NaOH solution into the beaker of the etching stage. The ring-shaped counter electrode should not be entirely inserted into the etchant but only touch the surface. In this way, disturbing H₂ gas bubbles are minimised at the tip.
- Immerse a W piece 1.5 mm into the etchant. At the etching power supply, set the etching voltage to 8.5 V, and the current threshold to =4 mA. If other NaOH concentrations are used, the voltage has to be adapted accordingly (~ 6 V for 4M, ~ 11V

for 2M). Focus the optical microscope and set the light source such that the meniscus around the wire is clearly visible. Put the Plexi-glass shielding around the stage and start the etching process.

- After two minutes, further immerse the wire by 0.05-0.1mm, to reduce the surface tension at the meniscus. Avoid any vibration at the etching stage.
- After the process was automatically stopped, take the readily etched tip out of the solution with a pair of tweezers. Rinse the tip carefully and thoroughly in DI water. If the tip is to be used immediately, dry it with clean N₂ gas and mount it into the tip holder. Otherwise store it in ethanol.
- Introduce the tip *as quick as possible* into the loadlock chamber (FEL, fast entry lock). While the chamber is opened, leave the N₂ gas valve slightly opened, and avoid any contamination of UHV parts. After closing, start pumping with the turbo pump.

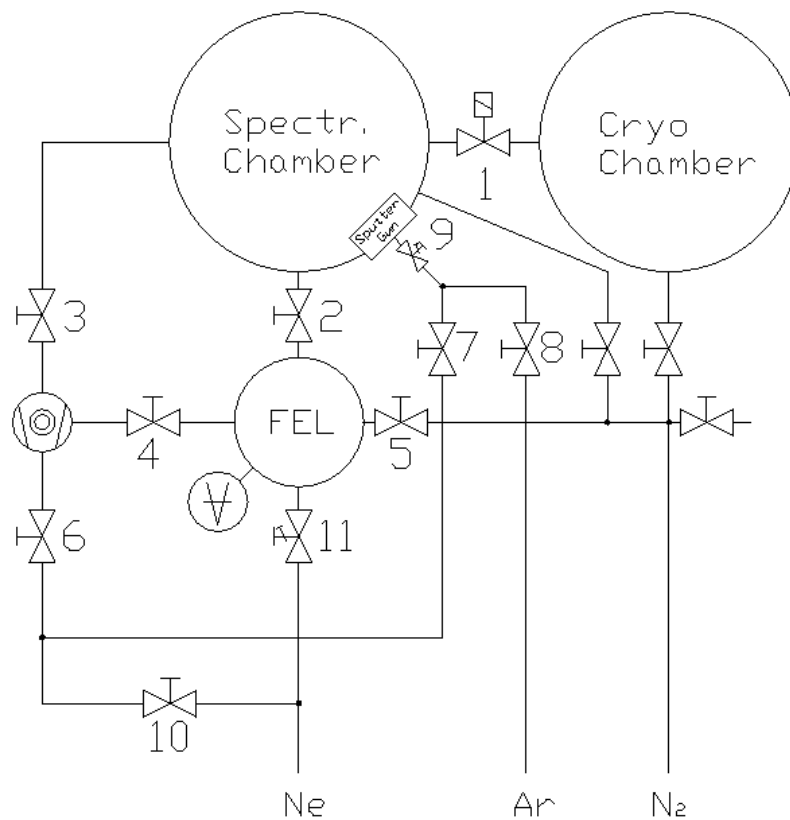


Figure A.1: Recipient and gas supplies of the Cryogenic STM

- For *self-sputtering* (see below), the gas supply line should be flushed few times: First open the main Ne valve to allow some gas into the line. Then, after closing the main

valve, pump the line by opening the valve which connects the Ne line directly to the turbo pump. Again close the pumping valve. This procedure ought to be repeated at least three times *right after starting to pump the loadlock* while the pump is at low revolutions. The gas supplies of the Cryogenic STM are illustrated in figure A.1. For pumping the Ne line, valves 6 and 10 have to be opened, accordingly. After flushing, allow for a slight Ne overpressure in the line.

Field emission (FE) test (cf. section 3.3)

- place the tip holder in the corresponding stage:
 - Into the left dovetail stage at the Cryogenic STM, cf. figure 3.20 at page 55; beware of touching the filament loop with the tip
 - At the VT-STM, sideways onto the steel angle, the contact spring touching the contact leg (cf. figure 3.21 on page 56); the appropriate position of the linear drive is around 10 mm
- Wait until the pressure in the loadlock has reached the 10^{-6} mbar region, in order to avoid vacuum discharges.
- Connect the HV output cable of the power supply for field emission and self-sputtering (FESS) to the current feedthrough of the respective tip conditioning stage (black=tip HV, blue=ground). *Before* swithing on the FESS power supply, set the mode switch to "voltage", and make sure that the voltage controle is set to zero. At the range selector, choose 1 nA.

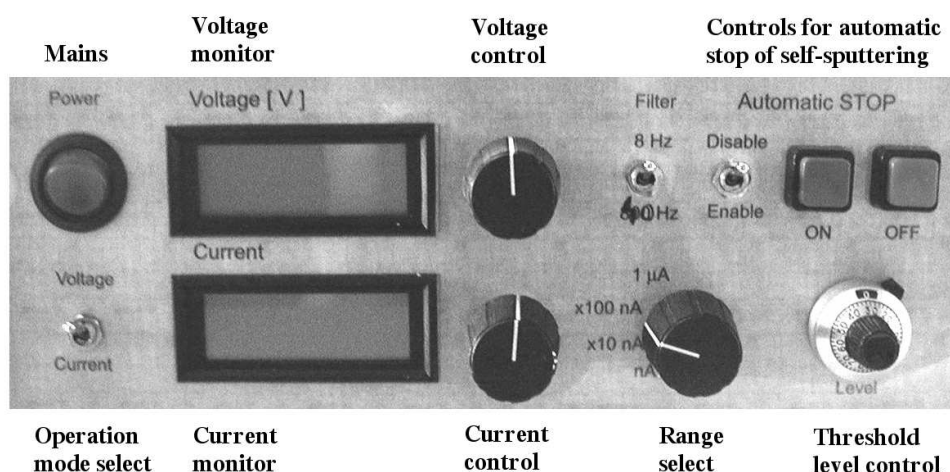


Figure A.2: Front panel of the power supply for field emission and self-sputtering (FESS), described in section 3.5.3

- *CAREFULLY* increase the voltage (upper knob), until the current meter shows a constant value of 1 nA. Note that any change in the applied voltage leads to a charging of the cable due to its finite capacitance. The displayed current value will therefore increase by few nA, and then quickly (within ~ 1 s) drop to the actual current reading.
- If the emission current fluctuates strongly, gently heat the tip (see below) for few minutes.
- The voltage V_{th} necessary to draw 1 nA gives an estimate for tip sharpness, cf. section 3.3
 - if $V_{\text{th}} > 600$ V - take a new tip.
 - if $V_{\text{th}} < 600$ V it is worth to continue with conditioning. For low values (up to 300 V), annealing by electron bombardment (if available) may be sufficient; otherwise go for Ne self sputtering.
- within the present work, best STM results were obtained with tips which had $V_{\text{th}} = 150$ to 300 V *after treatment*, independent of the initial value.

Direct resistive annealing (cf. section 3.4.1)

- This procedure may be applied as a first step of treatment, or subsequently to self-sputtering (see below).
- Place the tip holder such that the tip shank touches the W filament
 - Into the right dovetail stage at the Cryogenic STM. Using a handheld ohmmeter, one can check on the contact between tip (tip HV=black) and filament (fil. voltage=red, or ground=blue)
 - At the VT-STM, set the linear drive to 14 mm, and touch the filament, fine-tuning its position.
- Beware of applying force to the filament, since this might break the brittle W wire.
- Connect an adjustable DC power supply to 'fil. voltage'=red and ground=blue; suitable is the power supply for sample heating at the transfer rod (Delta electronics).
- Slowly increase the voltage until the filament begins to glow. The necessary power depends on the stage and the filament, usual values were $V \approx 1V$, $I \approx 2.8A$. A too strong annealing might blunt the tip.
- Note that the resistivity of the filament will further increase as its temperature raises, leading to an even stronger heating. One should therefore keep an eye on the brightness of the filament, and reduce the annealing power if necessary.

- After few minutes, *slowly* reduce the voltage to zero, and retract the tip.

Annealing by electron bombardment (not available at the VT-STM)

- At the Cryogenic STM, place the tip in the left dovetail, beneath the looped filament. Connect the TECTRA HV supply[42]: black=tip HV, yellow=filament, blue=ground. The pressure in the loadlock should be in the 10^{-7} mbar range or less.
- Measuring the emission current I_{emi} from the filament is performed as voltage measurement with a handheld voltmeter across a $10\text{ k}\Omega$ resistor in series with the output. That is, a reading of 1 mV corresponds to $I_{\text{emi}} = 0.01\ \mu\text{A}$.
- Tune the voltage V_{HV} to the desired value (e.g. 350 V), and increase the filament current I_{fil} until the filament starts to glow ($> 2\text{ A}$). Keep an eye on the pressure reading: Due to outgassing may rise drastically due to degassing from the filament. Further increase I_{fil} carefully, until I_{emi} reaches the desired value (usually 0.1 to 1.0 μA).
- Anneal the tip for 30s. Compensate strong fluctuations of I_{emi} by regulating I_{fil} .
- Check again on tip sharpness by field emission. If required, repeat annealing with gradually increased power.

Self sputtering (section 3.4.2)

- For this procedure, an initial tip sharpness is required (FE threshold $V_{\text{th}}(I = 1\text{ nA}) \lesssim 600\text{ V}$).
- The position of the tip is the same as for FE experiments in the respective STM's.
- The pressure in the loadlock should be in the (lower) 10^{-8} mbar range, to avoid discharges. Set the emission of the pressure gauge to 0.1 mA.
- Introduce the sputter gas, preferably Ne, into the chamber. The gate valve to the turbo pump should remain opened. In this way, the Ne pressure is better controllable. By means of the fine leak valve 11, set a pressure of $2.4 \cdot 10^{-5}$ mbar.
- Connect the FESS power supply as described above. In addition, make sure the device is connected to a computer via the USB interface.
- Before switching on the power supply, make sure that both voltage and current control are set to zero. Set the mode switch to "current", the range selector to 1 μA , and disable the automatic-stop mechanism.

- With the current control, increase the voltage until the desired emission current (10-20 μA) is displayed at the current monitor. If the tip is not sharp enough, it will not be possible to reach these values up to the limit of the power supply ($\lesssim 1 \text{ kV}$). In this case, an emission of a few μA still yields a appreciable sputter rate (it just takes somewhat longer). For less than 1 μA , one better goes for a new tip.
- When the current is stabilised, enable automatic stopping. If the voltage is fluctuating strongly, it might be necessary to increase the threshold with the threshold level control. Typical setting is 25 to 30.
- Start the "FESS" computer program, and press the "Start" button. Sputter voltage as well as emission current are monitored such that changes are visible. The displayed voltage U_c is corrected by the effect of the internal output resistance of the power supply (10.88 $\text{M}\Omega$).
- The sputter process can be interrupted by the "Stop" and "Start" buttons at the FESS power supply.
- Over time, the sputter voltage V_s should decrease gradually. However, it does not necessarily drop monotonously.
- After some time, the process is automatically terminated due to a jump in voltage. In order to check if the detected jump was indeed due to a decapitation of the tip (and not only due to some fluctuation of the signal), it is useful to perform a FE test. For this it is recommended to close the Ne gas inlet valve. The FE threshold for 1 nA should be lower than about 2/3 of V_s for an emission of 10 μA just before the voltage drop (this is just a rule of thumb based on experience). Another hint is the shape of the V_s vs t curve. Normally, one can observe a reduction of the noise, and a slight down-turn (both can be seen in figure 3.15 on page 47).
- After self-sputtering, it is strongly recommended to gently anneal the tip, in order to cure damages at the tip apex due to the sputter treatment.

Bibliography

- [1] R. Wiesendanger and H.-J. Güntherodt, editors. *Scanning Tunneling Microscopy III*, volume 29 of *Springer Series in Surface Sciences*. Springer, 2nd edition, 1996. [15](#), [18](#), [88](#)
- [2] G. Binnig and H. Rohrer. Scanning tunneling microscopy. *Helv. Phys. Acta*, 55:726–735, 1982. [16](#)
- [3] J. Bardeen. Tunneling from a many-particle point of view. *Physical Review Letters*, 6(2):57–59, 1961. [16](#)
- [4] J. Tersoff and D. R. Hamann. Theory of the scanning tunneling microscope. *Physical Review B*, 31(2):805–813, 1985. [16](#)
- [5] L. Pauling and E. B. Wilson, Jr. *Introduction to Quantum Mechanics*, chapter 27b, pages 198–201. Reprint by Dover Publications Inc., New York, 1985. [17](#)
- [6] R. J. Hamers. *Methods of Tunnelling Spectroscopy with the STM*, chapter 4, pages 51–103. In Bonnell [\[65\]](#), 1993. [17](#), [18](#)
- [7] W. Unertl. *The Surface Structure of Crystalline Solids*, chapter 5, pages 107–154. In Bonnell [\[65\]](#), 1993. [21](#), [65](#)
- [8] Omicron NanoTechnology GmbH, 65232 Taunusstein, Germany. [21](#), [33](#)
- [9] Oxford Instruments Ltd., Abingdon Oxfordshire, OX13 5QX, UK. [24](#)
- [10] F. Pobell. *Matter and Methods at Low Temperatures*. Springer Verlag, 2nd edition, 1996. [27](#)
- [11] H. F. Hess, R. B. Robinson, R. C. Dynes, J. M. Valles Jr., and J. V. Waszczak. Scanning-Tunneling-Microscope Observation of the Abrikosov Flux Lattice and the Density of States near and inside a Fluxoid. *Physical Review Letters*, 62(2):214–216, 1989. [27](#), [71](#), [72](#)

- [12] H. Rohrer. *The Preparation of Tips and Sample Surfaces for STM Experiments*, chapter 6, pages 155–187. In Bonnell [65], 1993. [29](#), [30](#), [31](#)
- [13] I. Ekvall, E. Wahlström, D. Claesson, H. Olin, and E. Olsson. Preparation and characterization of electrochemically etched W tips for STM. *Meas. Sci. Technol.*, 10:11–18, 1999. [29](#), [31](#), [42](#), [43](#), [44](#), [46](#), [48](#)
- [14] H. Neddermeyer and M. Drechsler. Electric field-induced changes of W(110) and W(111) tips. *Journal of Microscopy*, 152:459–466, August 1988. [30](#), [53](#)
- [15] J. G. Rodrigo, H. Suderow, and S. Vieira. On the use of STM superconducting tips at very low temperatures. *European Physics Journal B*, 40:483–488, 2004. [30](#)
- [16] S. H. Pan and E. W. Hudson and J. C. Davis. Vacuum tunneling of superconducting quasiparticles from atomically sharp scanning tunneling microscope tips. *Applied Physics Letters*, 73(20):2992–2994, 1998. [30](#), [70](#)
- [17] Santos F. Alvarado and Philippe Renaud. Observation of spin-polarized-electron tunneling from a ferromagnet into GaAs. *Physical Review Letters*, 68:1387–1390, 1992. [30](#)
- [18] R. Wiesendanger, D. Bürgler, G. Tarrach, A. Wadas, D. Brodbeck, H.-J. Güntherod, G. Güntherodt, R. J. Gambino, and R. Ruf. Vacuum tunneling of spin-polarized electrons detected by scanning tunneling microscopy. *Journal of Vacuum Science and Technology*, 9:519–524, 1991. [30](#)
- [19] A. Kubetzka, M. Bode, O. Pietzsch, R. Wiesendanger. Spin-polarized scanning tunneling microscopy with antiferromagnetic probe tips. *Physical Review Letters*, 88:057201, 2002. [30](#)
- [20] H. Ness and F. Gautier. The electronic structure and stability of transition metal nanotips - part I. *Journal of Physics: Condensed Matter*, 7:6625–6640, 1995. [31](#)
- [21] H.-W. Fink. Mono-atomic tips for scanning tunneling microscopy. *IBM Journal of Research and Development*, 30(5):460–465, 1986. [31](#), [53](#)
- [22] Vu Thien Binh. *In situ* fabrication and regeneration of microtips for scanning tunneling microscopy. *Journal of Microscopy*, 152:355–361, August 1988. [31](#), [42](#), [44](#)
- [23] O. Albrektsen, H. W. M. Salemink, K. A. Mørch, and A. R. Thölen. Reliable tip preparation for high-resolution scanning tunneling microscopy. *Journal of Vacuum Sciences and Technology*, 12(6):3187–3190, 1994. [31](#), [46](#), [48](#)
- [24] Goodfellow Cambridge Ltd., Huntingdon, PE29 6WR, UK. [31](#)

- [25] A.-S. Lucier, Henrik Mortensen, Yan Sun, and Peter Grüttner. Determination of the atomic structure of scanning probe microscopy tungsten tips by field ion microscopy. *Physical Review B*, 72:235420, 2005. [31](#)
- [26] R. Zhang and D. G. Ivey. Preparation of sharp polycrystalline tungsten tips for scanning tunneling microscopy imaging. *Journal of Vacuum Science and Technology B*, 14(1):1–10, 1996. [32](#), [33](#)
- [27] J. P. Ibe, P. P. Bey Jr., S. L. Brandow, R. A. Brizzolara, N. A. Burnham, D. P. DiLella, K. P. Lee, C. R. K. Marrian, and R. J. Colton. On the electrochemical etching of tips for scanning tunneling microscopy. *Journal of Vacuum Science and Technology A*, 8(4):3570, 1990. [32](#), [34](#), [42](#)
- [28] C. Bai. *Scanning Tunneling Microscopy and its Application*, volume 32 of *Springer Series in Surface Sciences*. Springer, 1995. [32](#)
- [29] A.-S.-Lucier. Preparation and Characterization of Tungsten Tips Suitable for Molecular Electronics Studies. Master’s thesis, Center for the Physics of Materials Department of Physics McGill University Montreal, Quebec Canada, 2004. [32](#), [36](#), [37](#), [42](#)
- [30] R. H. Fowler and L. Nordheim. Field Emission in Intense Electric Fields. *Proceedings of the Royal Society of London, Series A*, 119:173, 1928. [36](#)
- [31] L. Nordheim. The Effect of the Image Force on the Emission and Reflection of Electrons by Metals. *Proceedings of the Royal Society of London, Series A*, 121:626, 1928. [36](#), [39](#)
- [32] A. Modinos. *Field, thermionic, and secondary electron emission spectroscopy*. Plenum Press, 1984. [36](#)
- [33] A. P. Jansen and J. P. Jones. The sharpening of field emitter tips by ion sputtering. *Journal of Physics D: Applied Physics*, 4:118–123, 1970. [36](#), [37](#), [46](#), [49](#)
- [34] G. J. de Raad, P. M. Koenraad, and J. H. Wolter. Use of the Schiller decapitation process for the manufacture of high quality tungsten scanning tunneling microscopy tips. *Journal of Vacuum Sciences and Technology*, 17(5):1946–1952, 1999. [40](#), [42](#), [47](#), [49](#)
- [35] L. Ottaviano, L. Lozzi, and S. Santucci. Scanning Auger microscopy study of W tips for scanning tunneling microscopy. *Review of Scientific Instruments*, 74(7):3368–3378, 2003. [42](#)
- [36] Ch. Kittel. *Einführung in die Festkörperphysik*. Oldenbourg, 7th edition, 1988. [44](#), [65](#)

- [37] C. Schiller, A. A. Koomans, T. L. van Rooy, C. Schönenberger, and H. L. van Elswijk. Decapitation of tungsten field emitter tips during sputter sharpening. *Surface Science*, 339:L925–L930, 1995. [46](#), [48](#), [49](#)
- [38] J. Y. Cavaille and M. Drechsler. Ion impact on fieldemitter crystals. *Revue de Physique Appliquée*, 12:1631–1639, October 1977. [47](#), [49](#)
- [39] H. Vogel. *Gerthsen Physik*. Springer, 19th edition, 1997. [53](#)
- [40] W. Nolting. *Grundkurs Theoretische Physik 3: Elektrodynamik*. Springer, 6th edition, 2002. [53](#)
- [41] Ch. Renner. private conversation. [53](#)
- [42] tectra GmbH, 60323 Frankfurt/M, Germany. [55](#), [83](#)
- [43] Conrad Electronics GmbH, 92240 Hirschau, Germany. [57](#)
- [44] R. Wiesendanger and D. Anselmetti. *STM on Layered Materials*, chapter 6, pages 131–179. Volume 20 of R. Wiesendanger and H.-J. Güntherodt [[66](#)], 2nd edition, 1994. [60](#)
- [45] M. Tsukada, K. Kobayashi, N. Isshiki, S. Watanabe, H. Kageshima, and T. Schimizu. *The Role of Tip Atomic and Electronic Structure in Scanning Tunneling Microscopy and Spectroscopy*, chapter 5, pages 77–103. Volume 29 of Wiesendanger and Güntherodt [[1](#)], 2nd edition, 1996. [60](#)
- [46] Z. Y. Rong and P. Kuiper. Electronic effects in scanning tunneling microscopy: Moiré pattern on a graphite surface. *Physical Review B*, 48(23):17427–17431, 1993. [60](#), [61](#)
- [47] T. R. Albrecht, H. A. Mizes, J. Nogami, Sang il Park, and C. F. Quate. Observation of tilt boundaries in graphite by scanning tunneling microscopy and associated multiple tip effects. *Applied Physics Letters*, 52(5):362–364, 1987. [60](#)
- [48] M. Kuwabara, D. R. Clarke, and D. A. Smith. Anomalous superperiodicity in scanning tunneling microscope images on graphite. *Applied Physics Letters*, 56(24):2396–2398, 1990. [61](#)
- [49] J. W. McClure. Band Structure of Graphite and de Haas-van Alphen Effect. *Physical Review*, 108(3):612–618, 1957. [61](#), [64](#)
- [50] S. Reich, J. Maultzsch, and C. Thomsen. Tight-binding description of graphene. *Physical Review B*, 66:035412, 2002. [61](#)

- [51] H. Bross and W. Alsheimer. Electronic Structure of Graphite. *Reports on the Research Projects on the High Performance Computers of the Leibniz Computing Centre of the Bavarian Academy of Sciences and Humanities 1997-1999*, pages 374–376. [61](#)
- [52] S. Y. Zhou, G.-H. Gweon, C. D. Spataru, J. Graf, D.-H. Lee, Steven G. Louie, and A. Lanzara. Coexistence of Sharp Quasiparticle Dispersions and Disorder Features in Graphite. *Physical Review B*, 71:161403, 2005. [61](#)
- [53] MaTecK Material-Technologie & Kristalle GmbH, D-52428 Jülich, Germany. [65](#)
- [54] N. Takeuchi, C. T. Chan, and K. M. Ho. Au(111): A theoretical study of the surface reconstruction and the surface electronic state. *Physical Review B*, 43(17):13899–13905, 1991. [65](#), [68](#)
- [55] W. Haiss, D. Lackley, J. K. Sass, and K. H. Besocke. Atomic resolution scanning tunneling microscopy images of Au(111) surfaces in air and polar organic solvents. *Journal of Chemical Physics*, 95(3):2193–2196, 1991. [65](#)
- [56] Ch. Wöll, S. Chiang, R. J. Wilson, and P. H. Lippel. Determination of atom positions at stacking-fault dislocations on Au(111) by scanning tunneling microscopy. *Physical Review B*, 39:7988–7991, 1989. [65](#)
- [57] J. V. Barth, H. Brune, G. Ertl, and R. J. Brehm. Scanning tunneling microscopy observations on the reconstructed Au(111) surface: Atomic structure, long-range superstructure, rotational domains, and surface defects. *Physical Review B*, 42:9307–9318, 1990. [65](#)
- [58] B. Giambattista, A. Johnson, R. V. Coleman, B. Drake, and P. K. Hansma. Charge-density waves observed at 4.2 K by scanning-tunneling microscopy. *Physical Review B*, 37(5):2741–2744, Feb 1988. [70](#)
- [59] J. Bardeen, L. N. Cooper, and J. R. Schrieffer. Theory of Superconductivity. *Physical Review*, 108(5):1175–1204, 1957. [71](#)
- [60] R. C. Dynes, V. Narayanamurti, and J. P. Garno. Direct Measurement of Quasiparticle-Lifetime Broadening in a Strong-Coupled Superconductor. *Physical Review Letters*, 41(21):1509–1512, 1978. [71](#)
- [61] Ch. Renner, A. D. Kent, Ph. Niedermann, Ø. Fischer, and F. Lévy. Scanning Tunneling Spectroscopy of a Vortex Core from the Clean to the Dirty Limit. *Physical Review Letters*, 67(12):1650–1652, 1991. [71](#)
- [62] A. A. Abrikosov. On the Magnetic Properties of Superconductors of the Second Group. *Soviet Physics JETP*, 5(6):1174–1182, 1957. [71](#)

-
- [63] U. Essmann and H. Träuble. The direct observation of individual flux lines in type II superconductors. *Physics Letters*, 24A(10):526–527, 1967. [71](#)
- [64] S. Behler, S. H. Pan, P. Jess, A. Baratoff, H.-J. Güntherodt, F. Lévy, G. Wirth, and J. Wiesner. Vortex Pinning in Ion-Irradiated NbSe₂ Studied by Scanning Tunneling Microscopy. *Physical Review Letters*, 72(11):1750–1752, 1993. [72](#)
- [65] D. A. Bonnell, editor. *Scanning Tunneling Microscopy and Spectroscopy: Theory, Techniques and Applications*. VCH Publishers, Inc., 1993. [85](#), [86](#)
- [66] R. Wiesendanger and H.-J. Güntherodt, editors. *Scanning Tunneling Microscopy I*, volume 20 of *Springer Series in Surface Sciences*. Springer, 2nd edition, 1994. [88](#)

Acknowledgements

I would like to express my gratitude to all those persons from which I received support throughout the work for this thesis.

First and foremost, I thank Prof. Frank Steglich for his support in many respects, particularly for the opportunity to complete my Diploma in such a unique working environment. Specifically grateful I am to Steffen Wirth, who succeeded to give me excellent supervision during my work, even in turbulent times. I felt to have a lot of freedom to work individually, while never being alone "out on a limb". Particularly important were our numerous discussions and his helpful comments to this thesis.

Throughout the first part of my work I had the pleasure to cooperate with Michal Rams. I gratefully acknowledge his numerous contributions to this work, specifically concerning the electronics and software programming, and I enjoyed our fruitful and friendly discussions, whether they were about physics or not.

Furthermore, I would like to thank Sahana Rößler and Voicu Dolocan for the numerous discussions and the many helpful comments and proposals for corrections to this work.

The scanning electron microscopy data provided by Mrs. Petra Scheppan (in the groups of Rainer Ramlau and Ulrich Burkhard) make up an important part of this thesis. I appreciated the friendly and uncomplicated cooperation.

A number of technical problems which occurred during this work could be solved with support of the mechanical workshop and the electronics workshop of our institute.

Peter Kes I thank for providing the NbSe₂ sample which was used during my work.

Finally, I feel this is the right occasion to also express my heartfelt gratitude to my family, my parents in particular, who supported me in many ways throughout my physics studies. I also thank Ina for her patience and support during the time of writing-up.

Erklärung

Hiermit bestätige ich, dass ich diese Diplomarbeit ohne unzulässige Hilfe Dritter und ohne die Benutzung anderer als der angegebenen Hilfsmittel angefertigt habe. Die aus fremden Quellen direkt oder indirekt übernommenen Gedanken sind als solche kenntlich gemacht. Die Arbeit wurde bisher weder im Inland noch im Ausland in gleicher oder ähnlicher Form einer anderen Prüfungsbehörde vorgelegt.

Stefan Ernst

Dresden, 26. Juni 2006